



Ludwig-Maximilians-Universität München
Technische Universität München

Dynamic Rupture Modeling of the 2017 Mw 6.5 Botswana Intraplate Earthquake using SeisSol

Thesis submitted to Munich GeoCenter within the
Joint International Masters' Programme in Geophysics

Author: **Hongyi (Mike) Su**
Matriculation Number: **12335218**

Supervisors: **Prof. Dr. Alice-Agnes Gabriel**
and Dr. Max Moorkamp

Chair of Geophysics
Department of Earth and Environmental Sciences

Submitted date: September 12, 2022

©2022 – HONGYI SU
All rights reserved.

Preface

In the eighteenth century, philosophers considered the whole of human knowledge, including science, to be their field and discussed questions such as: did the universe have a beginning? However, in the nineteenth and twentieth centuries, science became too technical and mathematical for the philosophers, or anyone else except a few specialists. Philosophers reduced the scope of their inquiries so much that Wittgenstein, the most famous philosopher of this century, said, “The sole remaining task for philosophy is the analysis of language.” What a comedown from the great tradition of philosophy from Aristotle to Kant!

Stephen Hawking

Contents

Preface	i
Abstract	1
1 Introduction	2
1.1 Overview	2
1.2 Earthquake	2
1.3 Intraplate earthquakes	3
1.4 Botswana Intraplate earthquake	5
1.4.1 State of Knowledge	5
1.4.2 Tectonic setting	5
1.4.3 Trigger Hypothesizes	7
1.4.4 Motivation of this study	8
2 Method	10
2.1 Overview	10
2.2 Discontinuous Galerkin Method	10
2.3 Mesh	12
2.3.1 Model Design	12
2.3.2 Fault Geometry	12
2.4 Friction Law	15
2.5 Initial Stress Conditions	17
2.6 Nucleation Stress Conditions - Make the Rupture Start	19
2.7 Material Properties	20
2.8 Run <i>SeisSol</i>	21
3 Results	22
3.1 Overview	22
3.2 Parameter Study	22
3.3 Mesh	31
3.4 Dynamic Rupture Process - Slip	32
3.5 Dynamic Rupture Process - Slip Rate	33
3.6 Free Surface Output	35
3.7 Synthetic Seismograms	37
3.7.1 Seismological Data	37
3.7.2 Comparison of the Synthetic and the Observed Seismograms	39
3.7.3 Analysis Code	41
3.7.4 Observed Seismogram	42

4 Discussion	45
4.1 Overview	45
4.2 Nucleation - Lithstatic or Hydrostatic	45
4.3 Error Analysis - How can we improve the synthetic seismogram?	57
4.3.1 3D Velocity Model	57
4.4 Application	58
5 Conclusion	59
5.1 Overview	59
5.2 Key Findings from our Preferred DR Model	59
5.3 Holy Grail of Seismology	60
5.4 Future Work and Outlook	60
A.1 Source Parameters from CMT and USGS	63
A.2 3D Resistivity Model	65
A.3 Fault Traces at 5 km Depth	66
B.1 Configuration and Parameter Files (SeisSol)	67
B.1.1 Define a Fault Model - botswana_fault_700km_r6.yaml	67
B.1.2 Setup Initial Stress - initial_0.95.yaml	67
B.1.3 Nucleate the Rupture - nucleation_0.37_1.06km.yaml	68
B.1.4 Include Material Properties - botswana_material.yaml	69
B.1.5 Parameter File in SeisSol - parameter_700km_r6.par	70
B.1.6 Run SeisSol with a Shell Script - seis sol.sh	72
C.1 SeisSol Input Parameters for the Preferred Model	73
C.2 SeisSol Full Fault Output	74
C.3 Raw Synthetic Seismograms for All 16 Stations	74
D.1 Kinematic Model from Materna et al. (2019)	79
Nomenclature	80
Bibliography	80
List of Figures	87
List of Tables	90
Declaration of Competing Interest	92
Data and Resources	93
Acknowledgements	94
Statement	95
Selbständigkeitserklärung	96

Abstract

The 2017 Botswana intraplate earthquake is a deep, large, rare intraplate earthquake. In 2019, Max Moorkamp estimated two possible fault planes from a local 3D resistivity model (Moorkamp et al., 2019 [1]). In 2020 and 2021, two bachelor students, Thomas Obermaier and Sophia Gahr, performed static analysis on the first and second fault plane respectively (Obermaier, 2020 [2], Gahr, 2021 [3]). They have found optimal oriented fault parameters to maximize R value across the fault. In this thesis, we made a suite of dynamic rupture models with *SeisSol* to simulate the 2017 Botswana earthquake. Our dynamic rupture models adopt fault geometries and parameters from the previous static analysis. In chapter 1, we introduced the current understanding and models for the 2017 Botswana intraplate earthquake, in particular the deep fluid triggering hypothesis from Gardonio et al. (2018) [4]. In chapter 2, we introduced *SeisSol* code and explained in detail how we set up our dynamic rupture simulations with *SeisSol* in order to validate the fluid triggering hypothesis. In chapter 3, we showed the results from different rupture scenarios. We only vary two parameters, the nucleation radius and pore fluid pressure at nucleation. We found the predefined nucleation patch under lithostatic conditions is about 4 times larger than under hydrostatic conditions in order to have an earthquake at the target magnitude (Mw 6.46). We chose our preferred model to nucleate under hydrostatic conditions because it is more plausible to have a runaway rupture when the predefined nucleation patch is smaller. However, nucleation under the lithostatic conditions can also produce an earthquake at the target magnitude with a suitable nucleation patch. Our preferred model showed the earthquake has a moment magnitude of Mw 6.45, the rupture stopped around 5 s, and the slip on the fault plane is less than 1 m on average. The synthetics are comparable with the observations. Specifically, (1) the free surface output showed subsidence in the vicinity of the epicenter, the magnitude and area of the subsidence agree with geodetic measurements; (2) the synthetic seismogram matched only the polarity of the first arrival of the observed seismogram. In chapter 4, We compared two similar models, one nucleates under hydrostatic conditions and the other nucleates under lithostatic conditions. We found some similarities and differences from the fault output of the two dynamic rupture models. We also discussed how we could improve the synthetic seismogram to match the observational, the most important one is to convert a new material model that is big enough to include all seismic stations. The current material model was converted from a relatively small velocity model, and as a result, 5 out of the 7 seismic stations used in our dynamic rupture models are outside the material model domain. In chapter 5, we concluded that our approach of studying the 2017 Botswana intraplate earthquake with *SeisSol* can also apply to other intraplate earthquakes triggered by a transient stress increase, for instance, induced earthquakes from anthropogenic activities.

Chapter 1

Introduction

*Modern Science is based on the Latin injunction **ignoramus** - ‘we do not know’. It assumes that we don’t know everything. Even more critically, it accepts that the things we think we know could be proven wrong as we gain more knowledge. No concept, idea or theory is sacred and beyond challenge.*

Yuval Noah Harari, The Hebrew University of Jerusalem

1.1 Overview

In this chapter, we first introduce a brief history of how humankind understands earthquakes from different cultures and through times. Our ancestors made countless efforts to advance earthquake studies before 1900, we highlight some of the major scientific breakthroughs in seismology. Next, we introduce existing theories on intraplate earthquake genesis and the state of knowledge of the 2017 M 6.5 Botswana earthquake. Finally, we explain why we want to perform a dynamic rupture simulation on this event and what can we benefit from that.

1.2 Earthquake

The word *earthquake* is defined by the Oxford Dictionary as a sudden and violent shaking of the ground. Geophysicists, however, typically associate the term *earthquake* with a sudden shear slip on a fault within the earth.

The nature of earthquakes makes them intrinsically difficult to study. Throughout the 3500 years of recorded history by humans, people have been eager to find an explanation of the cause of earthquakes. In Japanese mythology, earthquakes are caused by a gigantic underground catfish, Namazu. The creature lives under the Japanese island and is guarded by the god Takemikazuchi, who restrains Namazu with a stone. When Takemikazuchi releases Namazu, an earthquake occurs (Smits, 2012) [5]. Meanwhile in Europe, devastating earthquakes were widely interpreted as the wrath of god. The ancient Greek philosopher Aristotle was one of the first to attempt an explanation based on natural phenomena. In about 400 BC, he proposed that earthquakes were caused

by winds trapped in subterranean caves (Missiakoulis, 2008) [6]. Nearly 260 years later, the Chinese astronomer and mathematician, Zhang Heng invented the first seismoscope in 132 BC. The device records disturbances along Earth's surface and is able to roughly indicate the direction of an earthquake over 600 km away (Yan and Hsiao, 2007) [7]. The 1755 Great Lisbon earthquake (M 8.7 on the Richter scale) marks the beginning of the modern era of seismology. The catastrophic earthquake shattered Portugal's proud capital, the city of Lisbon (Europe's fourth-largest city), took away 60,000 souls and destroyed 85% of Lisbon's buildings (Paith, 2008) [8]. Theologians saw the powerful earthquake and the scale of the tragedy as the awesome manifestation of the anger of God. On the other side, the event had a searing impact on European people, prompting numerous studies into the effects, location and timing of earthquakes. The 1755 Lisbon earthquake was the first event ever that conducted an objective damage survey using questionnaires. In 1851, Irish civil engineer and geophysicist, Robert Mallet, determined the velocity of seismic waves using explosions of gunpowder in different locations. He was also one of the first to estimate the depth of an earthquake underground. In 1879, Scottish physicist and engineer, Sir. James Alfred Ewing, recorded the first scientifically significant seismograph in Japan. German astronomer and geophysicist, Von Rebeur-Paschwitz obtained the first recording of a teleseism in Potsdam in 1889 (Dewey and Byerly, 1969) [9].

After 1900, more breakthroughs have been made in the field of seismology. Perhaps the most important one is the plate tectonic theory in the 1960s, it explains the stress accumulation due to tectonic plate marginal forces and earthquake mechanics at the plate boundaries. However, the intraplate earthquakes that are far away from the plate boundaries are still bewildering to seismologists even today.

1.3 Intraplate earthquakes

Intraplate earthquakes (IPEs) are a class of earthquakes that usually causes catastrophic damage. Johnson and Kanter (1990) found that the cumulative seismic moment of IPEs only accounted for 0.5% of the Earth's total (Johnson and Kanter, 1990 [10]). Despite this small percentage, large IPEs pose a significant threat to human lives and infrastructure due to the low attenuation of seismic energy within rigid continental plate interiors and the tendency of occurring on previously unknown faults (Talwani, 2014, 2016 [11][12]; Moorkamp et al., 2019 [1]). Large IPEs are rare, but the occurrence of this type of earthquake shows that the continental lithosphere can build up significant stresses (Materna et al., 2019) [13]. To date, large IPEs have been reported worldwide. For example, the 1886 Charleston earthquake (Mw 7.6) and New Madrid earthquake sequence ($M \geq 7.0$) of 1811-1812 in the United States (Hough and Armbruster, 2000) [14], the 1969 Ceres earthquake in South Africa (Krüger and Scherbaum, 2014) [15], and the 1988 Tennant Creek earthquake sequence ($M \geq 6.3$) in central Australia (Bowman, 1992) [16]. The 2017 Botswana earthquake (W-Pahse moment magnitude of 6.5, USGS;

Mw 6.4, Materna et al., 2018 [13]) is the most recent large intraplate earthquake, which occurred in the central district of Botswana and is the largest earthquake recorded in Botswana in 50 years since the 1952 Maun (M 6.7 on Richter scale) earthquake.

So why do IPEs occur? The triggering mechanism of IPEs has long been debated in the literature (Liu and Zoback, 1997 [17]; Pollitz et al., 2001 [18]; Calais et al., 2016 [19]). The first attempt to explain the stress accumulation of IPEs was made by Sykes and Sbar in 1973. They proposed that sufficient stresses build up at the plate boundaries and, given that the stable continental lithosphere is rigid and strong, these stresses are able to transmit over long distances, eventually reactivating a preexisting zone of weakness (Sykes and Sbar, 1973 [20]; Sykes, 1978 [21]). Moreover, about 50% of IPEs are observed to occur in failed continental rifts (Johnson and Kanter, 1990 [10]). According to Talwani, the most seismic energy release is associated with rifts and the preferential location of IPEs within rifts has a solid mechanical basis (Talwani, 2016 [12]). Talwani proposed a unified model for studying IPEs. The theoretical model can explain how stress builds up on various geological features, producing many of their observed characteristics (Talwani, 2016 [12]; Talwani, 2014 [11]). Based on the unified model, stress needs to build up at suitable geological features, called ‘local stress concentrators’ (LSCs). Examples of some LSCs are buried plutons, old rifts pillows, fault bends and intersections, and restraining stepovers. Then, based on the unified model, IPEs occur when the magnitude of this local stress buildup is comparable with the regional stress due to far-field regional tectonic forces. However, the other school of thought argues that IPEs occur far from plate boundaries and thus are not explained by the theory of plate tectonics (Beroza and Kanamori, 2015 [22]). Calais et al. (2016) challenged the view that an IPEs’ stress buildup is due to far field plate marginal forces. Observations show IPEs tend to not repeat at the same location, and that the location of IPEs is more random than deterministic. The observed strain accumulation in stable continental regions (SCR) is not fast enough to trigger a large earthquake, thus IPEs are predominantly triggered by a transient force instead of a steady tectonic loading (Calais et al., 2016 [19]).

In conclusion, there are two schools of thought on the genesis of an intraplate earthquake. One adopts the theories developed for earthquakes at plate boundaries to the intraplate earthquakes, connecting strain accumulation to the static tectonic loading. The other argues that the intraplate earthquake is due to a transient stress perturbation, thus the strain accumulation is due to a transient event, for instance, deep fluid migration.

1.4 Botswana Intraplate earthquake

1.4.1 State of Knowledge

On 3rd April 2017, a large rare intraplate earthquake hit the Central District of Botswana, USGS (United States Geological Survey) reported the moment magnitude of Mww 6.46 based on W-phase inversion, and a group of researchers from UC Berkeley later determined a moment magnitude of approximately Mw 6.4 based on their best-fitting teleseismic and geodetic joint inversion model, which corresponding to a 27% reduction of the moment (Materna et al., 2019 [13]). The epicentre of this event is located at -22.6784 in latitude and 25.1558 in longitude, and the depth of this earthquake is 29 km, as reported by GCMT (Global Centroid-Moment-Tensor) project, USGS place the depth of the event at 23.5 km. (See Appendix A.1)

Large uncertainties exist for the magnitude, location and fault planes which are associated with this event. In **Table 1.1**, we compare the fault geometry parameters from various studies. The GCMT moment tensor solution suggests two possible fault planes, one dipping to the northeast, while the other dips to the southwest, and this is confirmed by these studies.

Table 1.1: proposed fault geometry by various research group

Geophysicists	Strke [°]	Dip [°]	Rake [°]	Slip [m]	Depth [km]
Kolawole et al., (2017) [23]	126 NW-SE	72-74 NE	-114	1.8	21-24
Albano et al., (2017) [24]	304 NW-SE	65 NE	-131	2.7	20
Gardonio et al., (2018) [4]	differ by 180	73 ± 4 or 17 ± 4	NA	NA	29 ± 4
Materna et al., (2019) [13]	126 NW-SE	51 ± 30 SW	-107	0.66	23
Mulabisana et al., (2021) [25]	315 NW-SE	45 NE	-80	0.50	22 ± 3

The focal mechanism of the 2017 Botswana earthquake indicates normal faulting, which is consistent with the extensional stress pattern in Southern Africa on the World Stress Map (Heidbach et al., 2016 [26]). The epicentre of this event is far away from tectonic plate boundaries and characterized by a low risk of seismicity based on a Global Earthquake Model (GEM) by Pagani et al., (2018) [27].

1.4.2 Tectonic setting

The large-scale active tectonic regime of Southern Africa is the East Africa rift system (EARS) and the continent is slowly pulling apart in an approximately east-west orientation, thus resulting in normal faulting earthquakes in this region (Materna et al., 2019 [13]). In **Figure 1.1** taken from Materna et al., (2017), we can see that the rift system accommodates extension between the Nubian Plate in the northwest and the Somalian plate in the northeast. The extension is faster (46 mm/yr) in the north and slower (12

mm/yr) in the south, where the rift also splits into eastern and western branches (Kinabo et al., 2007 [28]; Stamps et al., 2008 [29]). Red bars indicate the SH_{max} (Maximum horizontal compressive stress) from the World Stress Map 2008 (Heidbach et al., 2010 [30]). The colored dots represent historical earthquakes from 1910 to 2017, based on the USGS COMCAT catalog (Materna et al., 2019 [13]).

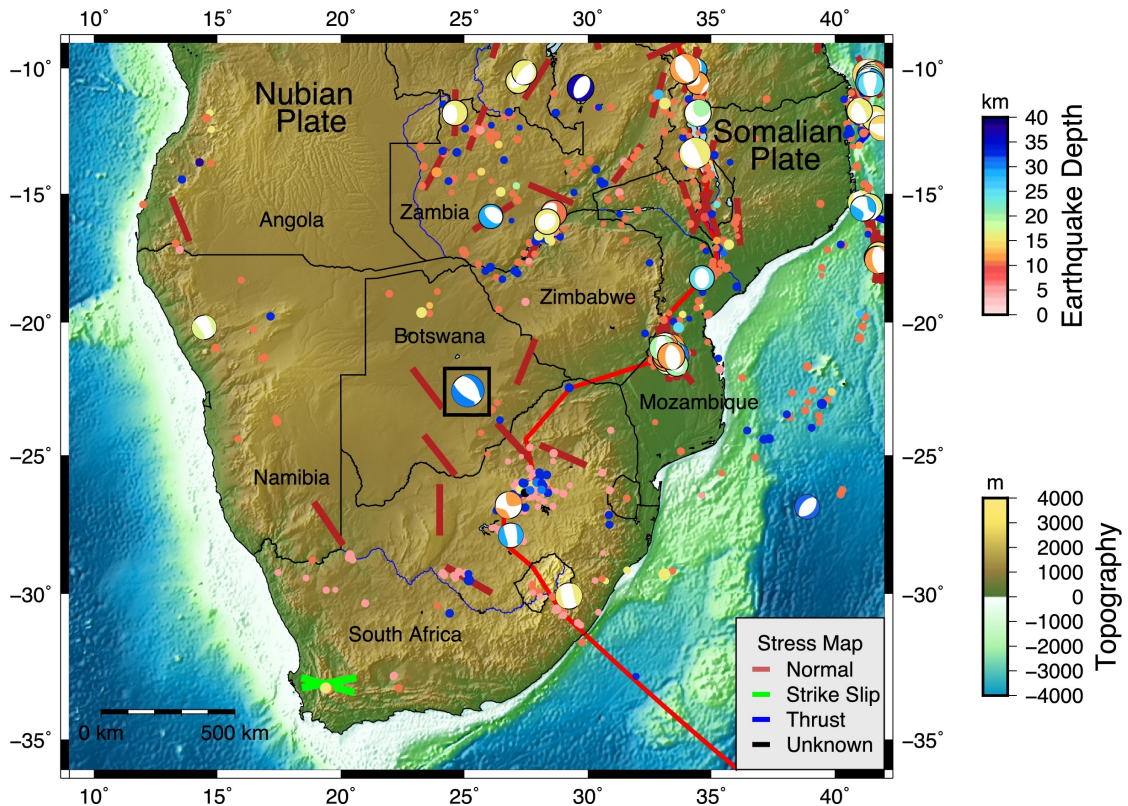


Figure 1.1: Tectonic setting of southern Africa, taken from Materna et al. (2019) [13].

In Botswana, past-recorded earthquakes clustered in the northwest part of the country, close to the Okavango Rift Zone (ORZ), which is part of the southwest branch of the EARS (Yu et al., 2017 [31]). In this area, a major seismic swarm was observed between 1951 and 1953, including two sequences of two M 5.8-5.9 earthquakes in 1952 (Reeves, 1972 [32]). To the south, the epicentral area had no large earthquakes in recorded history. This area belongs to Cratons, which are acknowledged as seismically inactive and tectonically stable. In **Figure 1.2**, taken from Materna et al. (2019), we can see that the epicentre of the earthquake was located in the middle of two major Cratons blocks, the Kaapvaal Craton and Zimbabwe Craton. They are composed of Proterozoic and Archean age rocks and have been deformed little since their formation (Beeler et al., 2008 [33]; De Wit et al., 1992 [34]). The Limpopo belt is Archean age continental material that was subjected to multiple episodes of intense deformation and high-grade

metamorphism throughout the Proterozoic (Mapeo et al., 2001 [35]). An aeromagnetic dataset clearly showing the Karoo dyke intrusions is in **Figure 1.2b** (Kolawole et al., 2017 [23]).

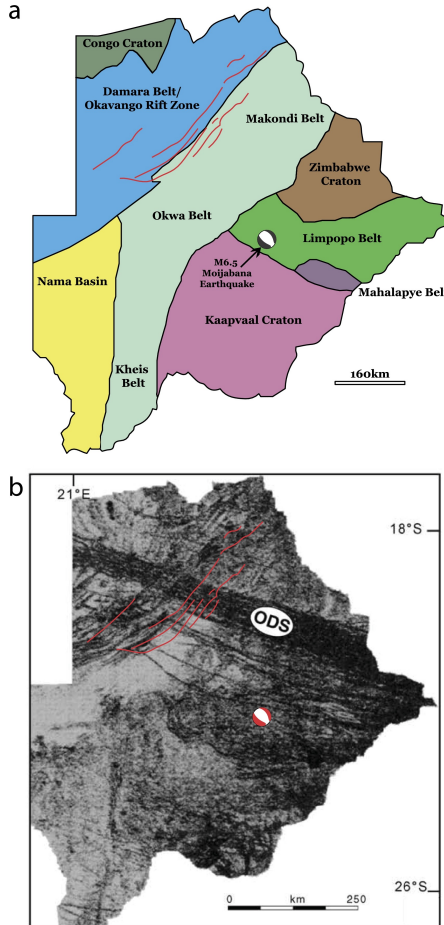


Figure 1.2: (a) Schematic geologic map of Archean terranes in Botswana, (b) Aeromagnetic data over Botswana showing the placement of Karoo dykes, taken from Materna et al., (2019) [13].

1.4.3 Trigger Hypothesizes

The 2017 Botswana earthquake is a natural earthquake. The Botswana earthquake occurred in an area with a low level of seismicity, thus it was suspected to be a human-made earthquake induced by nearby gas extraction. However, Albano et al. (2017) [24] disproved the anthropogenic hypothesis because the retrieved fault geometry and mechanism were incompatible with the hypothetical stress perturbation caused by the gas extraction. They concluded that the Botswana earthquake is a natural intraplate event.

Several pieces of evidence indicate the 2017 Botswana earthquake was reactivated on a preexisting zone of weakness. Kolawole et al. (2017) [23] associated the Botswana earthquake with reactivation of Neoproterozoic thrust sheets within the Limpopo Belt based on analysis of geodetic, aeromagnetic and gravity datasets. Materna et al. (2019) [13] also suggested that the earthquake took place within a preexisting zone of weakness from a Proterozoic collisional episode between two strong cratonic blocks. Moorkamp et al. (2019) [1] proposed that the earthquake was reactivated on preexisting thrust faults within the crust based on their inverted resistivity model (See Appendix A.2)

The deep fluid pulse from the EARS is suspected to be responsible for triggering the 2017 Botswana earthquake. Gardonio et al. (2018) [4] argued that a transient stress increase due to a local pulse of elevated fluid triggered the earthquake. The rocks at hypocentral depth should flow rather than break. It is the fluid that caused the ductile to the brittle transition of the viscous rock and triggered the earthquake. Fadel et al. (2020) [36] adopted the fluid triggering mechanism and connected the event to the EARS. They then inverted a shear velocity model using ambient noise and telesismic data and found a low shear velocity zone beneath the EARS. They interpreted this zone as potential conduits for fluid movement. Chisenga et al. (2020) [37] further suggested the fluid movement from the upper mantle beneath the EARS erodes the lower crust and could lead to future earthquakes in the Limpopo Belt.

1.4.4 Motivation of this study

Dynamic rupture models can help us reconcile different hypotheses, the rupture process is not generated from a simple point source but rather change dynamically. In dynamic rupture models, the outcome of the earthquake is not predetermined, we can validate mechanic viability of an earthquake scenario based on the outcomes. Dynamic rupture model is an excellent tool to investigate potential source characteristics, such as fault friction, fault geometry, and initial or nucleation stress field.

Moorkamp et al. (2019 [1]) could neither confirm nor refute the deep fluid triggering hypothesis put forward by Gardonio et al. (2018) [4]. On the one hand, they did not observe a mantle fluid reservoir of elevated fluid content in the upper mantle based on their MT data. On the other hand, the resolution of their resistivity model is not fine enough to detect small fluid pathways, resulting in the kernel of small water reservoirs to be zero in data space. The goal of our Dynamic Rupture (DR) simulations focus on validating the fluid triggering hypothesis. We simulate a transient increase of stress by changing the pore fluid ratio from lithostatic to hydrostatic at nucleation and increase the R value at the predefined nucleation patch. Moreover, we can determine the size of the nucleation patch that is potentially associated with the deep fluid reservoir that Moorkamp et al. (2019) [1] were not able to observe in their resistivity model.

In the absence of observations, which is the case for the 2017 Botswana earthquake,

dynamic rupture models can be used to generate a suite of scenarios to test source parameters that govern key rupture features (Ramos et al. (2022) [38]). The observational data for the 2017 Botswana earthquake is very limited. For example, there are no near-field strong motion data for this event (Materna et al. (2019) [13]), and the few available seismic recordings has low data quality (See Chapter 3). Moreover, dynamic rupture models can resolve the ambiguity of fault planes that moment tensor solutions and geodetic inversions cannot.

Chapter 2

Method

The question arises of which numerical scheme is capable of efficiently solving the elastic wave equation on tetrahedron (or generally unstructured) grids. This is the key motivation that led to the transference of the discontinuous Galerkin method to seismology.

Heiner Igel, Ludwig Maximilian University of Munich

2.1 Overview

In this chapter, we start with introducing the advantages of the discontinuous Galerkin method for solving dynamic rupture problems. Next, we present a cooking recipe for dynamic rupture simulations using the *SeisSol* solver, and the following ingredients a tetrahedron Mesh, a friction law, initial stress conditions, nucleation stress conditions, and a 3D elastic material model.

2.2 Discontinuous Galerkin Method

We use open-source code, *SeisSol*, to perform DR simulations. *SeisSol* is based on the Arbitrary high-order DERivative-Discontinuous Galerkin (ADER-DG) approach, which efficiently solves seismic wave propagation with high-order accuracy in space and time (Käser and Dumbser, 2006 [39]). The mathematical formula of the 3D elastic wave equation solved by *SeisSol* is

$$\begin{cases} \frac{\xi}{\xi_t} \sigma_{xx} - (\lambda + 2\mu) \frac{\xi}{\xi_x} u - \lambda \frac{\xi}{\xi_y} v - \lambda \frac{\xi}{\xi_z} w = 0, \\ \frac{\xi}{\xi_t} \sigma_{yy} - \lambda \frac{\xi}{\xi_x} u - (\lambda + 2\mu) \frac{\xi}{\xi_y} v - \lambda \frac{\xi}{\xi_z} w = 0, \\ \frac{\xi}{\xi_t} \sigma_{zz} - \lambda \frac{\xi}{\xi_y} u - \lambda \frac{\xi}{\xi_z} v - (\lambda + 2\mu) \frac{\xi}{\xi_z} w = 0, \\ \frac{\xi}{\xi_t} \sigma_{xy} - \mu \left(\frac{\xi}{\xi_x} v + \frac{\xi}{\xi_y} u \right) = 0, \\ \frac{\xi}{\xi_t} \sigma_{yz} - \mu \left(\frac{\xi}{\xi_z} v + \frac{\xi}{\xi_y} w \right) = 0, \\ \frac{\xi}{\xi_t} \sigma_{xz} - \mu \left(\frac{\xi}{\xi_z} u + \frac{\xi}{\xi_x} w \right) = 0, \\ \rho \frac{\xi}{\xi_t} u - \frac{\xi}{\xi_x} \sigma_{xx} - \frac{\xi}{\xi_y} \sigma_{xy} - \frac{\xi}{\xi_z} \sigma_{xz} = 0, \\ \rho \frac{\xi}{\xi_t} v - \frac{\xi}{\xi_x} \sigma_{xy} - \frac{\xi}{\xi_y} \sigma_{yy} - \frac{\xi}{\xi_z} \sigma_{yz} = 0, \\ \rho \frac{\xi}{\xi_t} w - \frac{\xi}{\xi_x} \sigma_{xz} - \frac{\xi}{\xi_y} \sigma_{yz} - \frac{\xi}{\xi_z} \sigma_{zz} = 0, \end{cases} \quad (2.1)$$

Where ρ is the density, μ is Lamé’s second parameter and λ is Lamé’s first parameter. (Their respective values are defined in the 3D elastic material file; see **Section 2.7**)

The geometrical flexibility of the discontinuous Galerkin method is an attractive feature for dynamic rupture problems (Igel, 2017 [40]). The very first attempt to solve wave-propagation problems on unstructured grids appears after Igel and Weber developed the first solvers for global wave propagation in spherical coordinates in 1995 (Igel and Weber, 1995 [41]; Igel and Weber 1996 [42]). Solving 3D wave-propagation on an unstructured tetrahedral mesh allows for complex fault geometry and high-resolution topography. *SeisSol* not only uses a computational mesh with different element size (also called h -adaptivity), but also has the option to vary the polynomial order arbitrarily in each cell (also called p -adaptivity) (Igel, 2017) [40]. This flexibility is crucial as DR simulations are sensitive to the complexity of fault geometry (Dunham et al., 2011 [43]; Shi and Day, 2013 [44]; Uphoff et al., 2017 [45]; Wollherr et al., 2018 [46], 2019 [47]; Ulrich et al., 2019 [48], 2019 [49]). Another advantage of the discontinuous Galerkin methods is that it uses the “weak-form” of the partial differential equations, because it implicitly satisfies the Neumann boundary conditions; thus, only Dirichlet boundary conditions need to be implemented for solving the wave equation (Marcus Mohr, Computational Geophysics Lecture; Heiner Igel, Computational Seismology Lecture).

For dynamic-rupture problems, the discontinuous Galerkin method is currently the most accurate solver for complicated fault models (Igel, 2017 [40]). The local time-stepping approach introduced by Dumbser et al. (2017) [50] made a substantial improvement to the discontinuous Galerkin method, enabling an arbitrary change in the tetrahedron mesh density to avoid oversampling. Thanks to the computer science community in Munich, the *SeisSol* code became a finalist of the prestigious Gordon Bell Prize in 2014. Its remarkable scaling behaviour as well as the obtained peak performance (Exceeding 1 PFlops) was the result of several years of performance optimization (Breuer et al., 2014 [51]). For a comprehensive list of alternative DR codes using various methods, we refer the interested reader to *Table 1* in Harris et al. (2018) [52] and *Table 2* in Erickson et al. (2020) [53].

However, for elastic wave-propagation problems without sophisticated geometries or strong material heterogeneities, the discontinuous Galerkin method is often not the preferred choice. Instead, finite-difference or spectral-element methods provide more efficient solutions (Igel, 2017 [40]). For an in-depth introduction to various numerical methods for wave-propagation problems, see Igel (2017) [40].

2.3 Mesh

2.3.1 Model Design

We use unstructured tetrahedron grids to describe a large rectangular volume with two fault planes. We implement DR boundary conditions on the two fault planes, absorbing boundary conditions on the bottom and side faces of the box and a free surface boundary condition on the remaining top face. We did not include topography for our mesh because (1) our fault planes do not intersect with the free surface and (2) the earthquake occurred in an area with little topographic relief (Moorkamp et al. 2019 [1], Materna et al. 2019 [13]).

We use a Cartesian coordinate system for our model, which is usually sufficient for all but the mega-earthquakes (M9) (Igel, 2017 [40]). The mesh domain is determined by the fastest P-wave velocity and the total simulation time. Although we have implemented absorbing boundary conditions, propagating seismic wave reflections from the sides can still distort our simulation results. For this reason, we need to define the dimension of our box domain to be large enough to avoid the unwanted reflections. The fastest P-wave velocity is estimated to be roughly 8.75 km/s by using an S-wave velocity model from Fadel et al. (2020) [36] (Obermaier, 2020 [2]). For example, if we want to simulate a total length of 40 seconds, then we would need our box domain to be at least 350 km away from the fault. Because we placed the epicentre of the Botswana earthquake at the origin (0,0) in Cartesian coordinates, the smallest box dimension in the XY plane is $700 \text{ km} \times 700 \text{ km}$.

It is important for our simulation to achieve resolved frequencies well above 1 Hz , because 1 Hz are the wavefields relevant for structure damage (Igel, 2017 [40]). We need two elements to resolve the smallest wavelength and, according to Obermaier (2020) [2], the minimal S-wave velocity is 2.5 km/s . As a result, we set the absolute element size on the fault planes to be 200 m , theoretically, we can resolve $\sim 6.25 \text{ Hz}$ along faults.

2.3.2 Fault Geometry

In **Table 2.1**, we show the fault geometry parameters for two possible fault planes, F129 and F126. F129 is the northeast dipping fault plane and F126 is the southwest dipping fault plane.

Table 2.1: Parameters of fault geometry

Fault	Strike [$^{\circ}$]	Dip [$^{\circ}$]	Element size [m]	Maximum depth [m]	Minimum depth [m]
F129	129	74	200	-37000	-5000
F126	126	-28	200	-37000	-5000

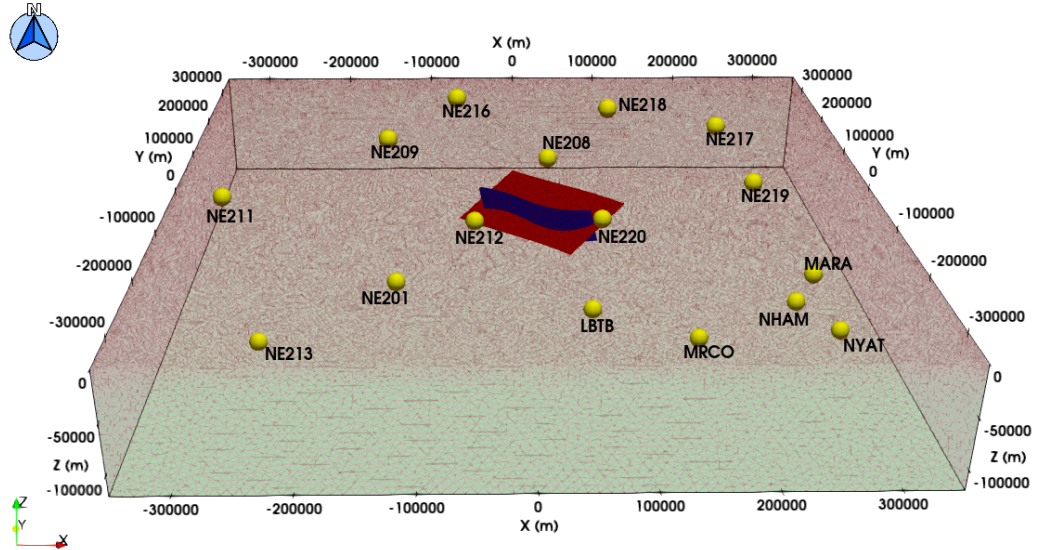


Figure 2.1: A 3D mesh of our proposed model plotted together with the locations of 16 seismic stations (yellow sphere) from the NR (FDSN code) network and two proposed faults, F129 dips to northeast (blue plane) and F126 dips to southwest (red plane)

The strike and dip angles of F129 and F126 are adopted from static analysis, see Obermaier (2020) [2] and Gahr (2021) [3]. These values are also comparable with Kolawole et al. (2017) [23] and Gardonio et al. (2018) [4], as well as the moment tensor solution from CMT. The two fault planes are buried at 5 km depth and extend down as far as 37 km. The shallower depth was chosen to because: (1) the fault has no surface expression and (2) the fault trace was estimated to be 5 km deep in a 3D resistivity model (Moorkamp et al., 2019 [1], See Appendix A.2 and A.3). The edge of the deeper extension is constrained by the end of the seismogenic zone at around 37 km (Stein and Wysession, 2009 [54]). The location of two fault planes in our mesh are determined by selecting points on fault traces that were estimated from the 3D resistivity model. Given the latitude and longitude pairs for each point, we used a python script from Thomas Ulrich to create the two non-planar fault planes. A smoothing parameter of 10^7 is applied for both fault planes to avoid kinks in the initial stress configuration.

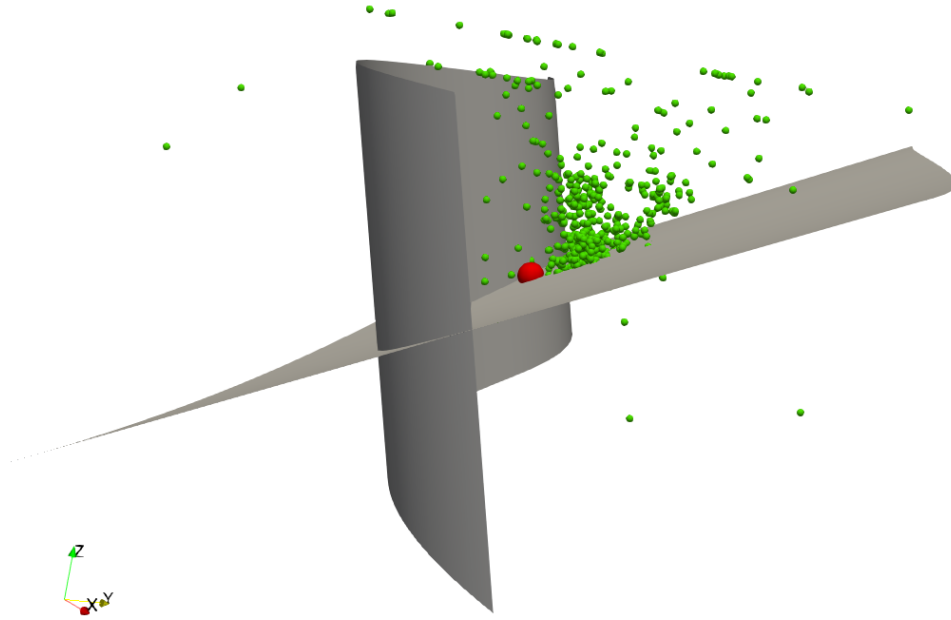


Figure 2.2: A 3D reconstruction of our proposed fault planes plotted together with the locations of the measured aftershocks (green dots) and the hypocenter (red sphere).

We can validate our proposed fault geometry with available aftershock distributions. In theory, aftershock locations should lie in the vicinity of reconstructed fault planes. Most aftershocks occur on or near the main shock's fault plane (Stein and Wysession, 2009 [54]). In **Figure 2.2**, we can see that our proposed fault planes fit reasonably well with the aftershock locations, most of which are located close to the intersection of the two planes. The red sphere represents the hypocenter, which is projected onto our local coordinate system (UTM 35K).

In summary, our proposed fault geometry is supported by static analysis (Obermaier (2020) [2], Gahr (2021) [3]), the moment tensor solution, 3D resistivity model (Moorkamp et al. (2019) [1], and aftershock distributions.

2.4 Friction Law

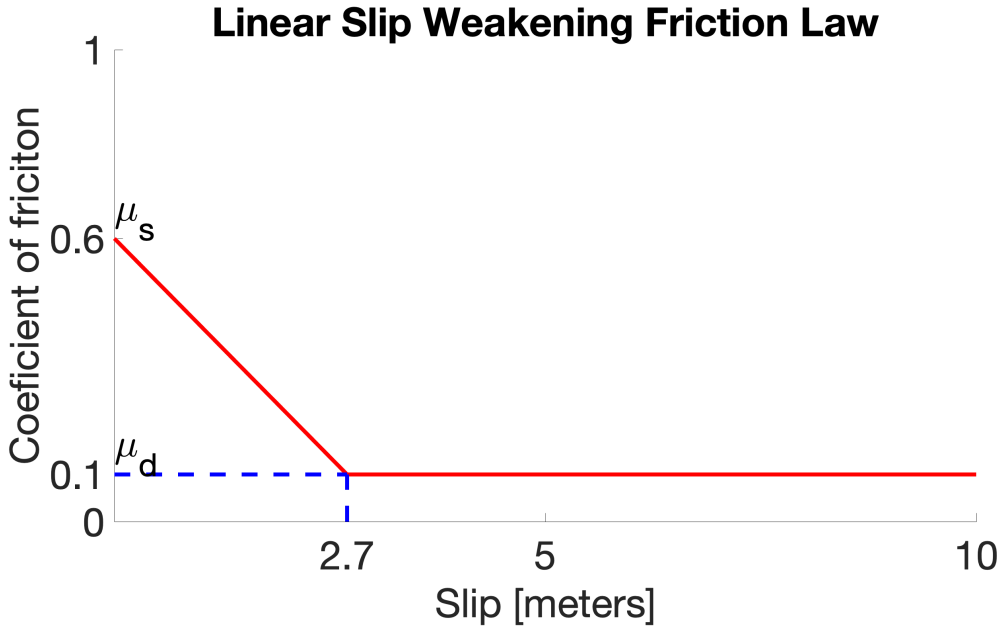


Figure 2.3: Slip-weakening friction law with $D_c = 2.7 \text{ m}$, $\mu_s = 0.6$ and $\mu_d = 0.1$

Two common friction laws used in dynamic rupture models are slip-weakening and velocity-weakening (Ramos et al., 2022 [55]). Friction has to drop from a static level to a lower sliding level for earthquake rupture to propagate (Beroza and Kanamori, 2015 [22]). In the slip-weakening friction framework, the earthquake propagation depends on the relative difference between static friction coefficient (μ_s) and dynamic friction coefficient (μ_d). When $\mu_s > \mu_d$, there is a finite drop in fault strength and this behaviour is called slip-weakening; otherwise, the fault exhibits neutral ($\mu_s = \mu_d$) or slip-strengthening ($\mu_s < \mu_d$) behaviour (Ramos et al., 2022) [55]. The dynamic friction coefficient only depends on slip and is parametrized by the slip-weakening critical distance (D_c) under a slip-weakening friction law. If, for some reasons, we are highly confident about the slip-weakening critical distance, let us assume 2.7 m for the Botswana earthquake, then we can set $D_c = 2.7$. **Figure 2.3** shows a plot of linear slip-weakening friction law with $D_c = 2.7$.

$$\mu = \begin{cases} \mu_s - (\mu_s - \mu_d) \cdot \frac{D}{D_c}, & D \leq D_c \\ \mu_d, & D > D_c \end{cases} \quad (2.2)$$

where μ is friction coefficient, D is the local fault slip.

However, the exact slip of the 2017 Botswana earthquake is hard to estimate as the

hypercenter is very deep, large uncertainty remains as evidenced by the different values used in different studies: 1.8 m (Kolawole et al. 2017) [23]; 2.7 m (Albano et al. 2017) [24]; 0.66 m (Materna et al. 2019) [13]; 0.5 m (Mulabisana et al. 2021) [25]; 0.7 m (Obermaier 2020) [2]). In addition to the uncertainty of the slip value, a slip-weakening friction law also does not allow faults to heal (i.e. recover their frictional strength). Once slip has occurred, crack-like rupture characteristics develop along the interface. (Gabriel et al., 2012 [56]). Therefore, realistic faults require a more complex frictional behaviour.

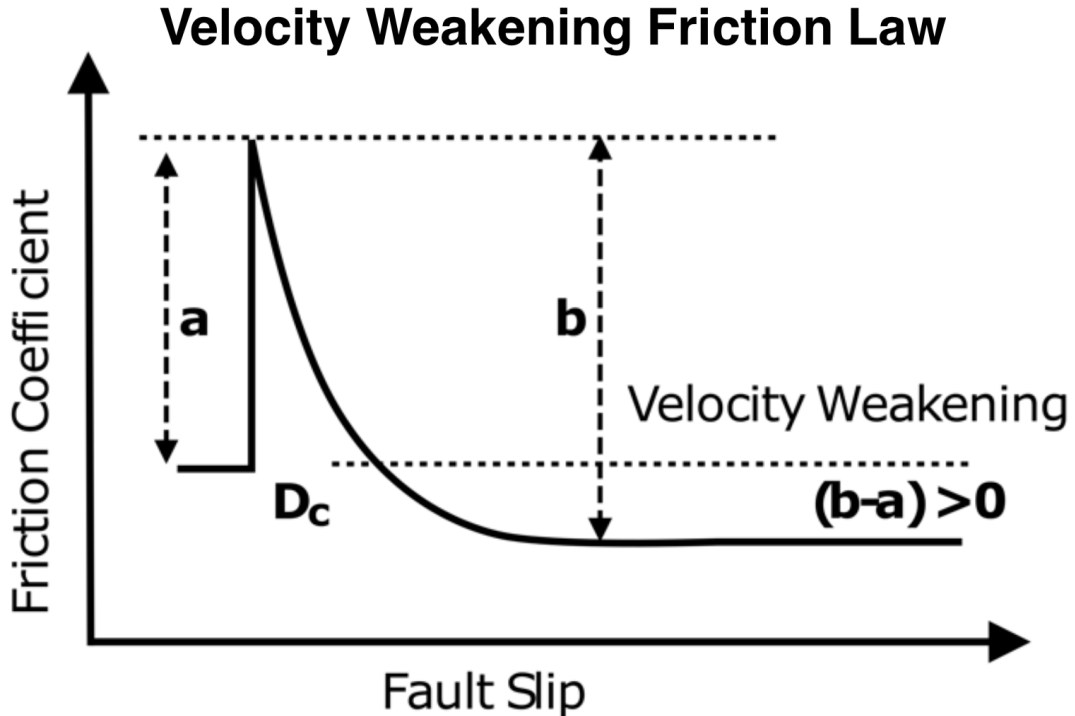


Figure 2.4: Velocity-weakening friction law, taken from Ramos et al., 2022 [55], Velocity weakening friction law

In this thesis, we use the state-of-the-art, Rate-and-State friction law, which uses a slip law with strong rate weakening (RS-SL-SRW) (SeisSol Document, SCEC TPV104). The velocity-weakening friction laws allow faults to heal, thereby promoting a pulse-like propagation (Heaton, 1990 [57]). **Figure 2.4** demonstrates how the friction coefficient is inversely proportional to the slip-rate during the coseismic phase under a velocity weakening friction law, which captures the general observation that fault friction is inversely proportional to slip-rate during an earthquake (Cochard and Madariaga, 1994 [58]; Ampuero and Ben-Zion, 2018 [59]).

In **Table 2.2**, we show a list of Rate-and-State friction law parameters adopted from

Palgunadi et al. (2020) [60]. Most of the friction parameters are fault independent. They are related to some microscopic processes and represent internal properties of a minerals (personal conversion with Casper Pranger). Note that we made a simplification to the spatial-dependent variables, a and V_W . According to Palgunadi et al. (2020) [60], $a = 0.01$ and $V_W = 0.1$ when the depth is deeper than 3.3 km . Since the fault planes in our model are buried at 5 km depth and the earthquake nucleates at 29 km , we consider this simplification is reasonable. Typical ranges for $a, b \in [0.001 -- 0.1]$ (Ampuero and Ben-Zion, 2008 [59]; Kozdon and Dunham, 2013 [61]).

 Table 2.2: *SeisSol* Friction Parameters for Rate-and-Sate Friction Law (FL=103)

SeisSol name	Physical meaning	Symbol	Used value
rs_a	Direct effect parameter	$a(x)$	0.01
RS_b	Evolution effect parameter	b	0.014
RS_sr0	Reference slip velocity	V_0	10^{-6} m/s
RS_sl0	Characteristic slip scale	L	0.1 m
RS_srW	Weakening slip velocity	$V_W(x)$	0.1
RS_f0	Steady-state friction coefficient	f_0	0.6
Mu_W	Weakening friction coefficient	f_W	0.1
RS_iniSlipRate1	Initial sliding velocity	V_{ini}	10^{-16} m/s
t_0	Forced rupture decay time	t_0	0.4 s

Similar to the slip-weakening framework, the relative difference between a and b controls when the fault exhibits velocity-weakening ($a < b$), neutral ($a = b$) or velocity-strengthening ($a > b$) behaviour (Romas et al., 2022 [55]). In our case, velocity-weakening ($a - b = 0.01 - 0.014 = -0.04$) across the entire fault. $V_0 = 10^{-6}$ and $V_{ini} = 10^{-16}$ are adopted from Palgunadi et al. (2020) [60]. For characteristic slip, we use $L = 0.1\text{ m}$. Similar to the slip-weakening friction law, $f_0 = \mu_s = 0.6$ and $f_W = \mu_d = 0.1$, where $\mu_s = 0.6$ is from laboratory measurements, most rocks at seismogenic depth has coefficient of friction around 0.6 (Byerlee, 1978 [62]). The choice of $\mu_d = 0.1$, $V_{ini} = 10^{-16}$, $t_0 = 0.4$ is based on experiment of SeisSol Earthquake computing group (LMU Munich).

Rate-and-State friction law parameters setup in *SeisSol* (see Appendix B.1.1 and B.1.5).

2.5 Initial Stress Conditions

We describe the initial stress field via a stress tensor, which describes the forces acting on a deformable continuous medium. Because stress tensor is symmetric, we only need 6 parameters (i.e. s_{xx} , s_{yy} , s_{zz} , s_{xy} , s_{yz} , s_{xz}) to fully describe the state of stress at a given point in the medium. The three diagonal components of the stress tensor (i.e.

s_{xx} , s_{yy} , s_{zz}) are known as normal stress, while the six off-diagonal components (i.e. s_{xy} , s_{yx} , s_{xz} , s_{zx} , s_{yz} , s_{zy}) are termed shear stress (Stein and Wysession, 2009 [54]).

We use the following equations to set up the initial stress conditions in *SeisSol* (see Appendix B.1.2),

$$s_{ij} = \begin{cases} s_{xx} = \text{Omega} \cdot b_{xx} + (1 - \text{Omega}) \cdot eCS, \\ s_{yy} = \text{Omega} \cdot b_{yy} + (1 - \text{Omega}) \cdot eCS, \\ s_{zz} = \text{Omega} \cdot b_{zz} + (1 - \text{Omega}) \cdot eCS, \\ s_{xy} = \text{Omega} \cdot b_{xy}, \\ s_{yz} = \text{Omega} \cdot b_{yz}, \\ s_{xz} = \text{Omega} \cdot b_{xz}, \end{cases} \quad (2.3)$$

$$\text{Omega} = \begin{cases} 1, & z \geq -33000 \\ 1 - 3 \cdot (1 - \frac{z+37000}{4000})^2 - 2 \cdot (1 - \frac{z+37000}{4000})^3, & -37000 \leq z \leq -33000 \\ 0.001, & \text{otherwise} \end{cases} \quad (2.4)$$

$$eCS = 2670 \cdot (1 - \gamma) \cdot 9.8 \cdot \min(-5000, z), \quad (2.5)$$

Where *Omega* is a scalar, it gradually reduces the magnitude of the shear stresses in areas deeper than seismogenic zone (33 km) in order to prevent the rupture propagates downwards, because it would make no physical sense to have a rupture beyond this depth. We set *Omega* to a very small number (i.e. 0.001) for stress field deeper than the maximum fault depth (37 km). The width of stress decrease zone is 4000 m, it is the difference between the maximum fault depth and the depth of seismogenic zone. *eCS* means the effective compressive stress (also termed effective normal stress), which is caused by the weight of the overlying rock. The purpose of *eCS* is to counterbalance the smoothing effect by *Omega* on normal stress components. In which 2670 m/s^2 in **Equation 2.5** is the average overlying rock density (Obermaier, 2020 [2]) and 9.8 m/s^2 is the gravitational constant. The function $\min(-5000, z)$ filters the depth to be at least 5 km because we embedded our faults at this depth. γ is the fluid pressure ratio, we set $\gamma_{ini} = 0.95$ because (1) it is very close to the lithostatic condition (Madden et al., 2022 [63]) and (2) we adopted the parameter value from a static analysis (Obermaier, 2020 [2]) to constrain the initial fault strength.

The six stress tensor components (i.e. $b_{xx}, b_{yy}, b_{zz}, b_{xy}, b_{yz}, b_{xz}$) in **Equation 2.3** are calculated by a function called *AndersonianStress* in *easi* (Easy Initialization of models)

library. The *easi* is a library written in C++14, developed by Carsten Uphoff (Intel) who was a former member of the *SeisSol* Earthquake computing group. **Table 2.3** shows the input parameters of the *easi* function.

 Table 2.3: *AndersonianStress* Input Parameters

SeisSol name	Symbol	Value	Physical meaning
mu_d	μ_d	0.1	dynamic friction coefficient
mu_s	μ_s	0.6	static friction coefficient
SH_max	SH_{max}	132.0	the azimuth of maximum compressive horizontal stress
S_v	S_v	1	define which one is the vertical principal stress
cohesion	-	0.0	rock internal property
s2ratio	ν	0.5	stress shape ratio
S	S	1 / (R-1)	relative fault strength
sig_zz	σ_{zz}	$\rho_{eff} \cdot g \cdot h$	the effective normal stress

We set dynamic and static friction coefficient parameter $\mu_d = 0.1$ and $\mu_s = 0.6$ (see 2.4). We set $S_v = 1$ because the 2017 Botswana earthquake has a normal-faulting focal mechanism. $cohesion = 0$ because our faults do not intersect with the surface. $\nu = 0.5$ means pure extension (Ulrich et al., 2019 [49]). σ_{zz} is equivalent to the aforementioned variable, *eCS*. $SH_{max} = 132$ and $R = 0.7$ are from the static analysis (Obermaier, 2020 [2]), S is determined by R . We adopted the static analysis result from Obermaier et al. (2020) [2], the four parameters, $R_{ini} = 0.7$, $\nu = 0.5$, $\gamma_{ini} = 0.95$, $SH_{max} = 132$, can fully describe the stress state and relative strength of the fault (Ulrich et al., 2019 [48]).

2.6 Nucleation Stress Conditions - Make the Rupture Start

We apply overstressed patch method (Kanamori, 1981 [64]) to nucleate the rupture. Nucleation is done by imposing additional shear stress in a predefined nucleation patch. To validate the deep fluid triggering hypothesis that put forward by Gardonio et al. (2018) [4], we increase the shear stress at nucleation patch by changing two parameters in the *AndersonianStress* function. First, we decrease the pore fluid pressure (γ) from 0.95 (γ_{ini}) to 0.37 (γ_{nuc}), which represents change from the lithostatic conditions to the hydrostatic conditions (Madden et al. 2022 [63]); Second, we increase the relative prestress ratio (R) from 0.7 (R_{ini}) to 4 (R_{nuc}), which means we force the predefined nucleation patch to rupture. The rupture spontaneously nucleates in the predefined nucleation patch. We define the nucleation patch as a circle centred at a nucleation point.

We define a spacial filter called $ShapeNucleation(r)$ for nucleation stress field set up,

$$nuc_{ij} = \begin{cases} nuc_{xx} = ShapeNucleation(r) \cdot b_{xx}, \\ nuc_{yy} = ShapeNucleation(r) \cdot b_{yy}, \\ nuc_{zz} = ShapeNucleation(r) \cdot b_{zz}, \\ nuc_{xy} = ShapeNucleation(r) \cdot b_{xy}, \\ nuc_{yz} = ShapeNucleation(r) \cdot b_{yz}, \\ nuc_{xz} = ShapeNucleation(r) \cdot b_{xz}, \end{cases} \quad (2.6)$$

$$ShapeNucleation(r) = \begin{cases} \exp\left(\frac{r^2}{r^2 - r_c^2}\right), & r < r_c \\ 0, & \text{otherwise} \end{cases} \quad (2.7)$$

$$r = \sqrt{(x - x_c)^2 + (y - y_c)^2 + (z - z_c)^2}, \quad (2.8)$$

The $ShapeNucleation(r)$ is a bell-shaped function, where r_c is the radius of the pre-defined nucleation circle. r is the euclidean distance of an arbitrary point (i.e. x , y , z) to the nucleation point (i.e. x_c , y_c , z_c). The epicenter of the earthquake has been recentered at origin (0,0) in our local coordinate system, therefore, the hypocenter is (0,0,-29000). However, the point (0,0,-29000) is not located on our proposed fault plane, we need to manually pick a nucleation point (x_c , y_c , z_c) that is on the fault plane and to be as close to the hypocenter as possible. For instance, we found the point (-3446.35, 5.21, -29000.00) on fault F129. Due to the uncertainty of the hypocenter, the estimated nucleation point can be seen as the actual earthquake hypocenter. Nucleation stress set up in *SeisSol* (see Appendix B.1.3).

2.7 Material Properties

Elastic material properties (ρ , μ and λ) were translated from a local 3D shear velocity model by my supervisor, Max Moorkamp. The velocity model is a subset of the 3D velocity model from Fadel et al. 2020 [36]. The following equation demonstrates the empirical relationship between shear velocity and density (Miller and Stewart, 1991 [65]),

$$\rho = -0.0000045 \cdot V_s^2 + 0.432 \cdot V_s + 1711, \quad (2.9)$$

And the ratio of V_p and V_s are suggested to be around 1.75 (Fadel et al., 2018 [66]),

$$\frac{V_p}{V_s} = 1.75, \quad (2.10)$$

Shear and compressional wave velocity can be expressed by elastic parameters. The following equations demonstrate the relationship between two elastic parameters and P- and S-wave velocities,

$$V_p = \sqrt{\frac{\lambda + 2 \cdot \mu}{\rho}}, \quad (2.11)$$

$$V_s = \sqrt{\frac{\mu}{\rho}}, \quad (2.12)$$

Where ρ is the density, μ is the Lamé's second parameter and λ is the Lamé's first parameter, they are the same parameters used in **Equation 2.1** for solving the wave propagation PDEs. We use default value $\rho = 3330 \text{ kgm}^3$, $\mu = 65,942,325,000 \text{ Pa}$ and $\lambda = 81,235,350,000 \text{ Pa}$ for grids outside the local velocity model. Material properties' set up in *SeisSol* (see Appendix B.1.4).

2.8 Run *SeisSol*

Carefully annotated parameter and YAML configuration files are attached in Appendix B.2. Note that the exclamation mark (!) in YAML file means to call a function, for instance, *!Switch*, *!ConstantMap* and *!Include* in *botswana_fault_700km_r6.yaml*. But the exclamation mark (!) in parameter file (*.par) means comment. See *easi* Documentation (Uphoff, 2022) for definitions of the used functions in our model setup (*.yaml)

We run *SeisSol* in a parallel computing environment with OpenMP. A shell script is attached in Appendix B.1.6. *SeisSol* supports parallel computing with MPI (Message-Passing Interface standard). MPI consists of libraries that can be called from Fortan, C, C++ and Python (pyMPI). In the attached shell command, n indicates the number of allocated CPU processors. How large should n be in order to achieve optimal performance? To answer this question, we need to consider scaling because adding more processors does not necessarily mean more speed-up for even high percentages of parallelizability. *SeisSol* is a remarkable example of strong scaling and obtained peak performance at 1.09 PFlops on SuperMUC at Leibniz Supercomputing centre, Munich (Igel, 2017 [40]).

Chapter 3

Results

If geophysics requires mathematics for its treatment, it is the Earth that is responsible, not the geophysicist.

Sir Harold Jeffreys, Cambridge University

3.1 Overview

In this chapter, we find a combination of parameters that can produce an earthquake scenario close to the target magnitude, Mw 6.5, by trial-and-error approach. We find the model with 1060 meters of nucleation radius under hydrostatic conditions is most likely to represent a realistic scenario of the 2017 Botswana earthquake. We then focus on the dynamic rupture results of our preferred model. First, we discuss the quality of observational seismic data in the region and showed the filtered synthetic seismograms. We compare the synthetic seismograms and observed seismograms of 7 seismic stations. Second, we show the initial stress conditions on two possible fault planes. We observe the rupture only propagates on the northeast dipping fault and stops naturally around 5 seconds. Finally, we compare the free surface output with the InSAR measurements and found that they are comparable.

3.2 Parameter Study

To save CPU hours, we first run DR simulations on a smaller mesh with only 10 s of the total simulation time (20 timesteps). After we obtained a good result by trial-and-error approach, we apply the same parameters for a bigger mesh and run the simulation longer. As explained in Chapter 2, we adopted the static analysis results from Obermaier (2020) [2] and Gahr (2021) [3] to reduce our model space and avoid running unlikely scenarios. In order to accomplish our deep fluid validation goal, we only vary two parameters in our study, which are the pore fluid pressure (γ_{nuc}) at nucleation and the radius of the nucleation sphere (r_c). **Table 3.1** shows the selected DR model setups and the results.

Table 3.1: SeisSol Simulation Results

Model	Mesh	γ_{nuc}	$r_c [km]$	Magnitude	Fault	Time [s]
5_ref_litho	Mesh4	0.95	1.00	Mw 4.5475	F129	10.0
5_ref_hydro	Mesh4	0.37	1.00	Mw 6.3479	F129	10.0
5_ref_hydro2	Mesh4	0.37	1.00	Mw 6.3488	F129	20.0
3_ref	Mesh3	0.37	1.00	Mw 2.9159	F126	10.0
5_l1	Mesh4	0.95	10.00	Mw 7.1310	F129	10.0
5_l2	Mesh4	0.95	2.00	Mw 5.4790	F129	10.0
5_l3	Mesh4	0.95	3.00	Mw 5.9844	F129	10.0
5_l4	Mesh4	0.95	4.00	Mw 6.3455	F129	10.0
5_r1	Mesh4	0.37	2.00	Mw 7.0863	F129	10.0
5_r2	Mesh4	0.37	1.20	Mw 6.6767	F129	10.0
5_r3	Mesh4	0.37	1.50	Mw 6.9504	F129	10.0
5_r4	Mesh4	0.37	1.10	Mw 6.5075	F129	10.0
5_r5	Mesh4	0.37	1.08	Mw 6.4751	F129	10.0
5_r6	Mesh4	0.37	1.06	Mw 6.4431	F129	10.0
5_r7	Mesh4	0.37	1.04	Mw 6.4112	F129	10.0
5_r8	Mesh4	0.37	1.02	Mw 6.3795	F129	10.0
700km_r4	Mesh700km	0.37	1.10	Mw 6.5159	F129	40.0
700km_r6	Mesh700km	0.37	1.06	Mw 6.4503	F129	40.0

First, we ran two simulations, `5_ref_litho` and `5_ref_hydro`, the former sets $\gamma_{nuc} = 0.95$ (close to lithostatic condition), while the latter sets $\gamma_{nuc} = 0.37$ (close to hydrostatic condition), and both of them use the same nucleation radius, $r_c = 1 \text{ km}$. The lithostatic reference model, `5_ref_litho`, produced a too small earthquake (Mw 4.5475). On the other hand, the hydrostatic reference model (i.e. `5_ref_hydro`) produced an earthquake of magnitude Mw 6.3479. To make sure the rupture in the scenario, `5_ref_hydro`, has a natural stop (i.e. not forced to stop by the simulation time), we increased the total simulation time to 20 s, and got a magnitude of Mw 6.3488 in the model, `5_ref_hydro2`. This result proves that the rupture process stopped naturally on the fault.

Chapter 3 Results

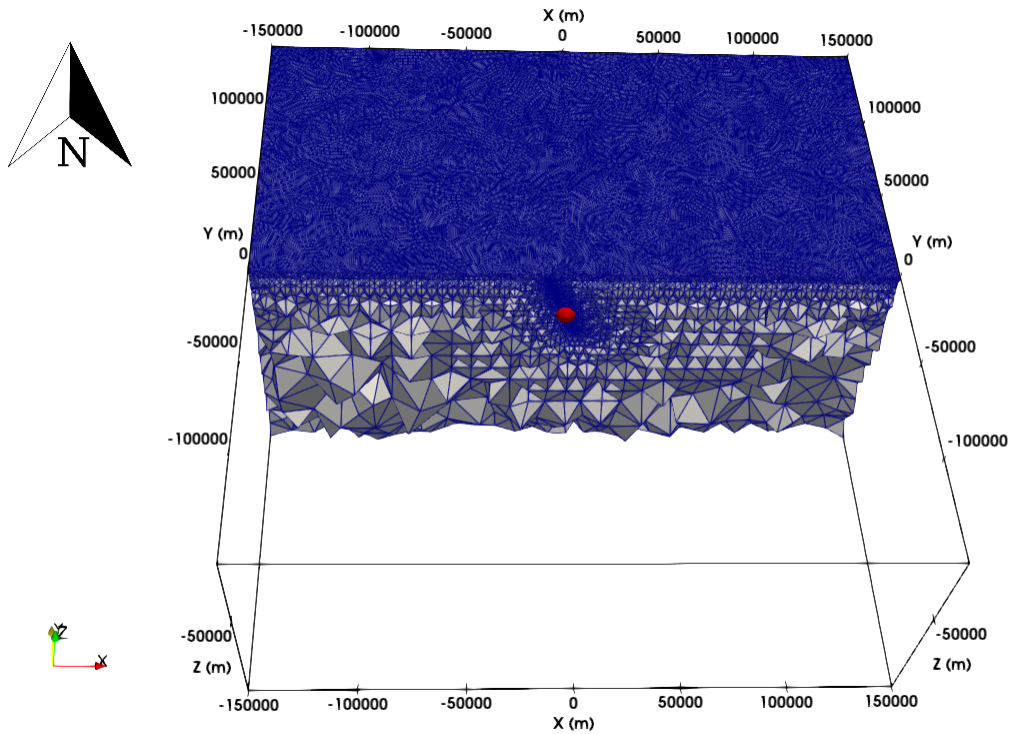


Figure 3.1: Mesh4 visualization in Paraview, only contain fault F129, consists of 1,291,885 tetrahedron elements, red sphere represents hypocenter

Chapter 3 Results

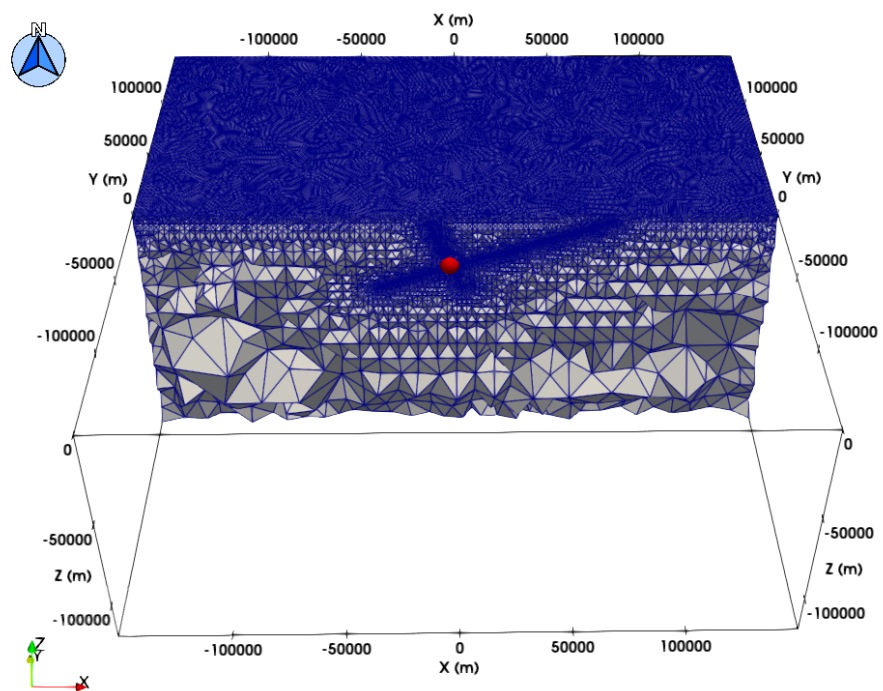


Figure 3.2: Mesh3 visualization in Paraview, contain both fault F126 and F129, consists of 676,984 tetrahedron elements, red sphere represents hypocenter

Chapter 3 Results

Model-3_ref (Mw 2.9159)

Nucleation under hydrostatic (0.37) pore fluid pressure with 1km predefined nucleation radius

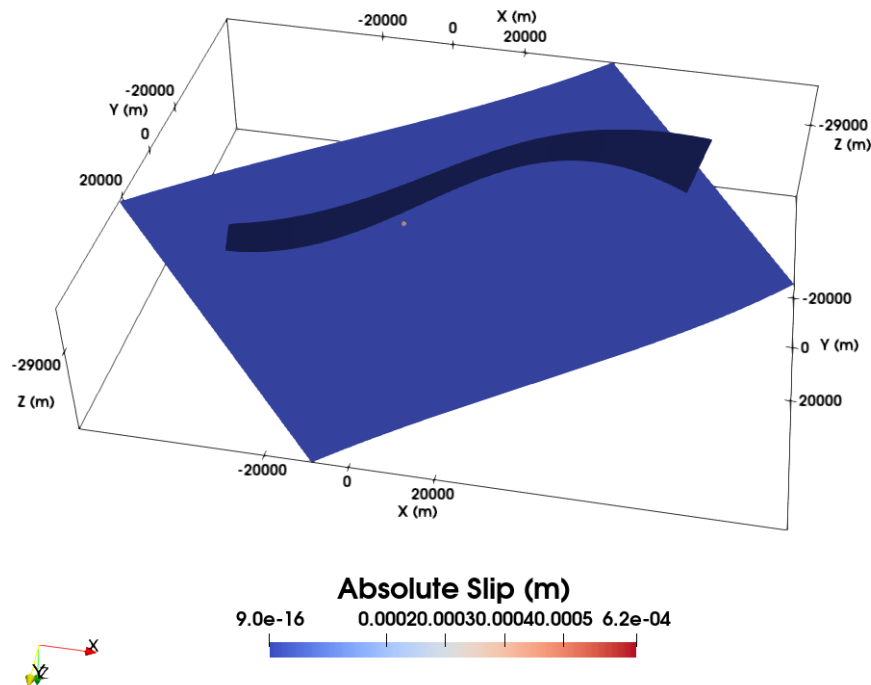


Figure 3.3: Dynamic rupture fault output of Model-3_ref, we show the absolute slip on the reconstructed second fault plane, F126

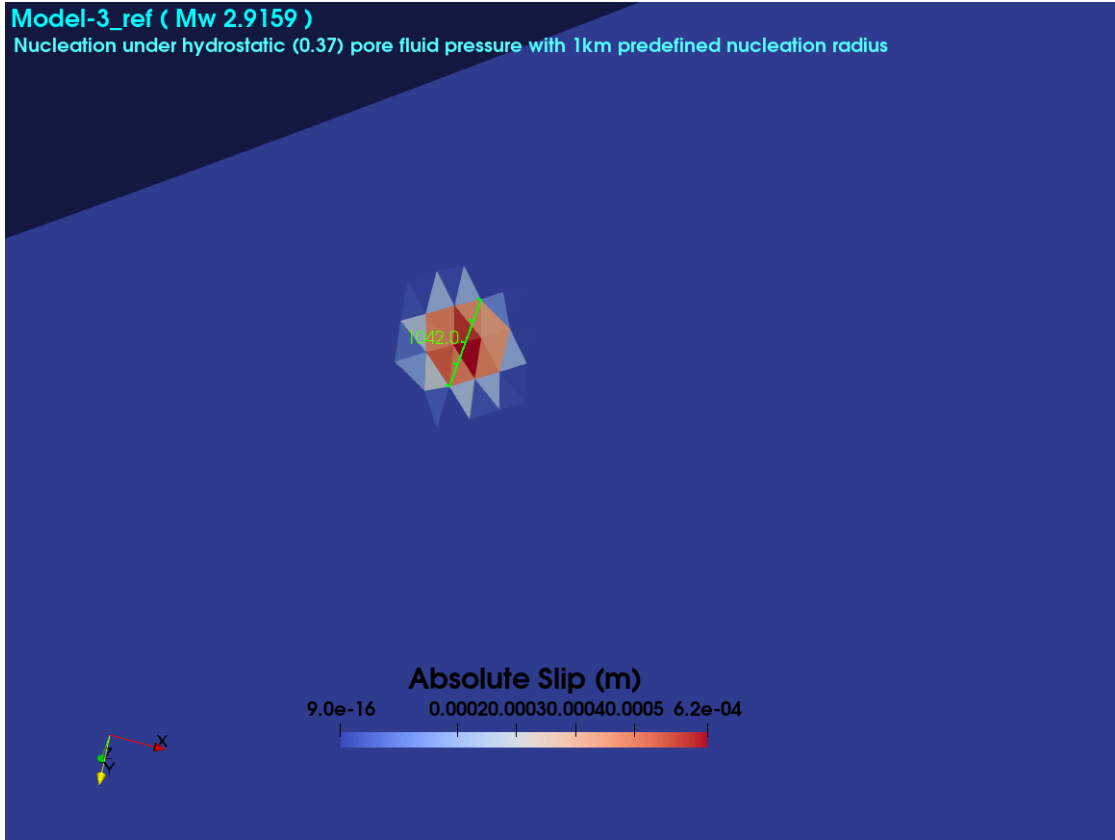


Figure 3.4: A zoomed view of Figure 3.3 in the nucleation area, a green ruler measures the indicated line distance of the ruptured zone is about 1042 m

Second, we want to know whether it is also possible to have a rupture on the second fault plane, F126. The first two discussed models ran on *Mesh4*, which only contains the first fault plane, F129 (**Figure 3.1** shows a visualization of *Mesh4* in *Paraview*). We ran another model on *Mesh3*, which contains both faults, F129 and F126 (**Figure 3.2** shows a visualization of *Mesh3* in *Paraview*). We chose a nucleation point on the second fault, F126, and found that the magnitude is too small (Mw 2.9159) despite using the same parameters (i.e. γ_{nuc} and r_c) as the model *5_ref_hydro*. **Figure 3.3 and 3.4** shows the absolute slip on the fault, F126, is very small, the ruptured zone is inside the predefined nucleation patch. This is expected, as Sophia Gahr concluded in her Bachelor's thesis that the second fault plane is not optimally oriented (Gahr, 2020 [3]), which means the second fault plane, F126, is not able to sustain a larger earthquake rupture. Therefore, we conclude that the rupture most likely nucleates on the first fault plane, F129.

Model-5_l4 (Mw 6.3455)
Nucleation under lithostatic (0.95) pore fluid pressure

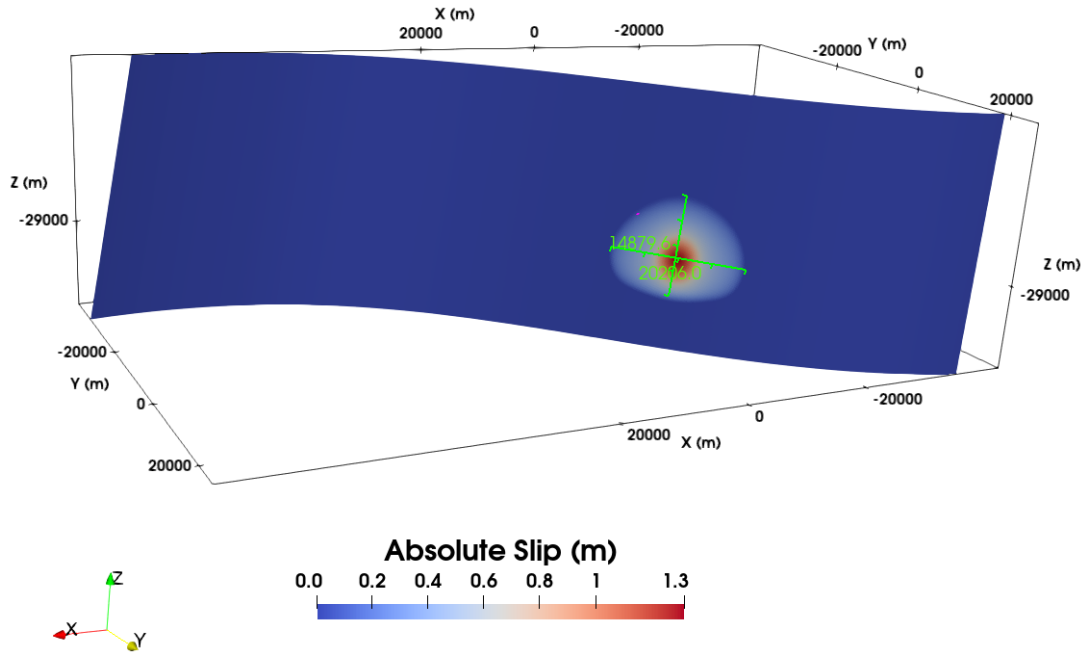


Figure 3.5: Dynamic rupture fault output of the Model-5_l4, we show the absolute slip on the reconstructed first fault plane, F129

The reference model of nucleation under the lithostatic conditions (5_ref_litho) has a nucleation radius of 1 km. When we increased the nucleation radius to 10 km in model 5_l1, we found that this model produce an earthquake scenario with magnitude greater than Mw 7. This means the rupture is able to nucleates under lithostatic conditions and produce an earthquake with magnitude of the target value. We vary r_c to 2 km, 3 km, and 4 km respectively in model 5_l2, 5_l3, and 5_l4. The larger r_c , the larger magnitude. We found the model 5_l4 produce an earthquake with magnitude close to the target value. **Figure 3.5** shows the absolute slip of the Model-5_l4. The rupture has a natural stop and extend outside the predefined nucleation patch. The geometry of nucleation area has an irregular shape, the indicated horizontal line is about 20206 m and the indicated vertical line is about 14879.6 m. If we simply take the average value, then the width of the ruptured zone is about 17542.8 m. The predefined nucleation patch roughly account for 45.6 % of the total ruptured area.

Chapter 3 Results

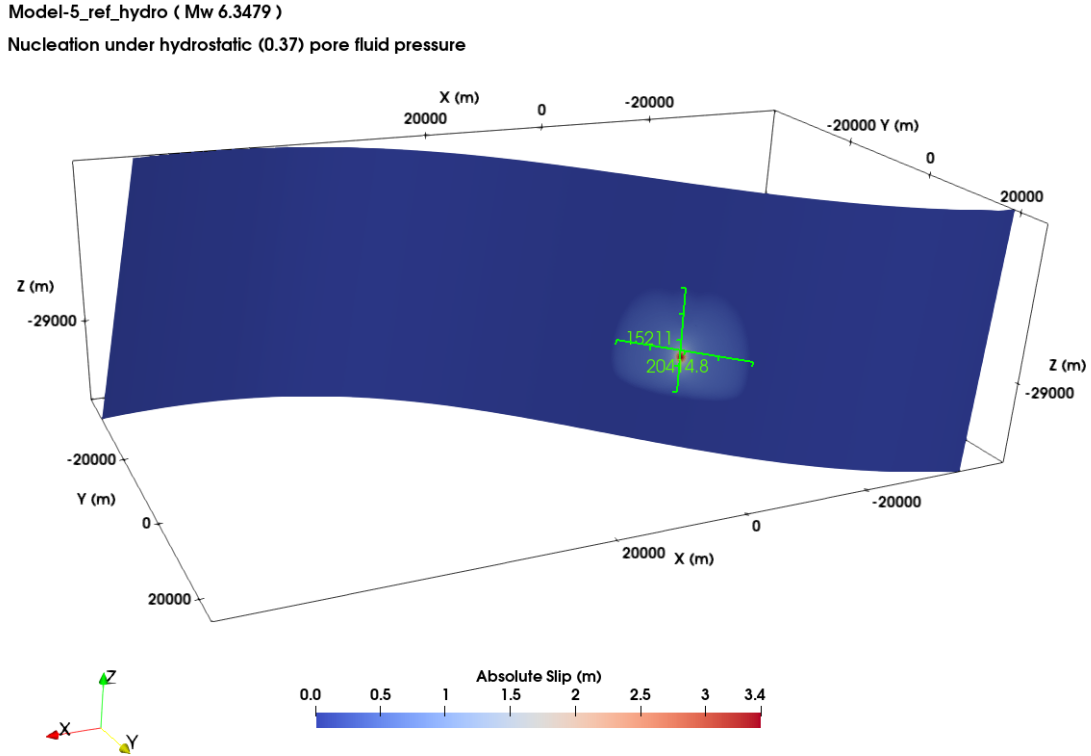


Figure 3.6: Dynamic rupture fault output of the Model-5_ref_hydro, we show the absolute slip on the reconstructed first fault plane, F129

The geometry of nucleation area of the Model-5_ref_hydro and Model-5_l4 are very similar. **Figure 3.6** shows the absolute slip of the Model-5_ref_hydro. The indicated horizontal line is about 20414 m and the indicated vertical line is about 15211 m. The area of ruptured zone and resulting earthquake magnitude is comparable for two models, one nucleates under hydrostatic conditions and the other nucleates under lithostatic conditions. However, we noticed that the maximum absolute slip of the Model-5_ref_hydro is larger, this maybe due to larger initial stress under the hydrostatic conditions. Moreover, the predefined nucleation patch roughly account for only 11.2 % of the total ruptured area for the Model-5_ref_hydro. Because we artificially increase the R value within the nucleation patch, the smaller percentage means a more realistic rupture scenario. Therefore, we chose our preferred model to nucleate under the hydrostatic conditions (i.e. $\gamma_{nuc} = 0.37$). We tune the nucleation radius in the Model-5_r1 to Model-5_r8. We found that the Model-5_r4 with $r_c = 1.10 \text{ km}$ and the Model-5_r6 with $r_c = 1.06 \text{ km}$ produce Mw 6.5075 and Mw 6.4431 respectively. They are the two best candidates for our preferred model.

In the next step, we ran these two model setups on a bigger mesh, *Mesh700km*, for

Chapter 3 Results

40 s and found the resulting magnitude for the Model-700km_r4 and Model-700km_r6 are Mw 6.5159 and Mw 6.4503 respectively. *Mesh700km* is much bigger than *Mesh4*, it has a dimension of $700\text{km} \times 700\text{km} \times 120\text{km}$. **Figure 3.7** shows a visualization of *Mesh700km* in *Paraview*. The moment magnitude from USGS is Mw 6.46 (see Appendix A.1), thus we chose our preferred model to be Model-700km_r6. The seismic moment for *Model – 700km_r6* is $6.033\text{e+018 N}\cdot\text{m}$, which corresponds to 2.5% reduction of moment from the USGS W-phase inversion ($6.188\text{e+18 N}\cdot\text{m}$). The full *SeisSol* input parameters for the preferred model, see Appendix C.1.

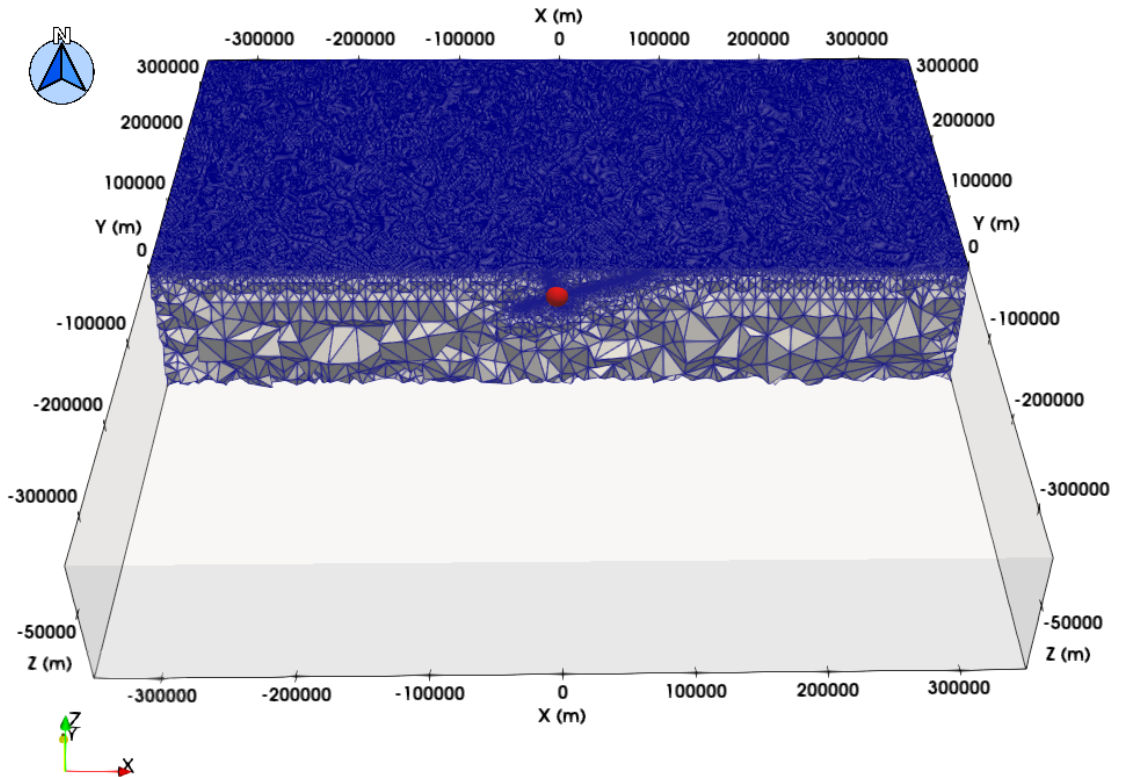


Figure 3.7: *Mesh700km* visualization in *Paraview*, consists of 2,124,064 unstructured tetrahedron grids, red sphere represents hypocenter

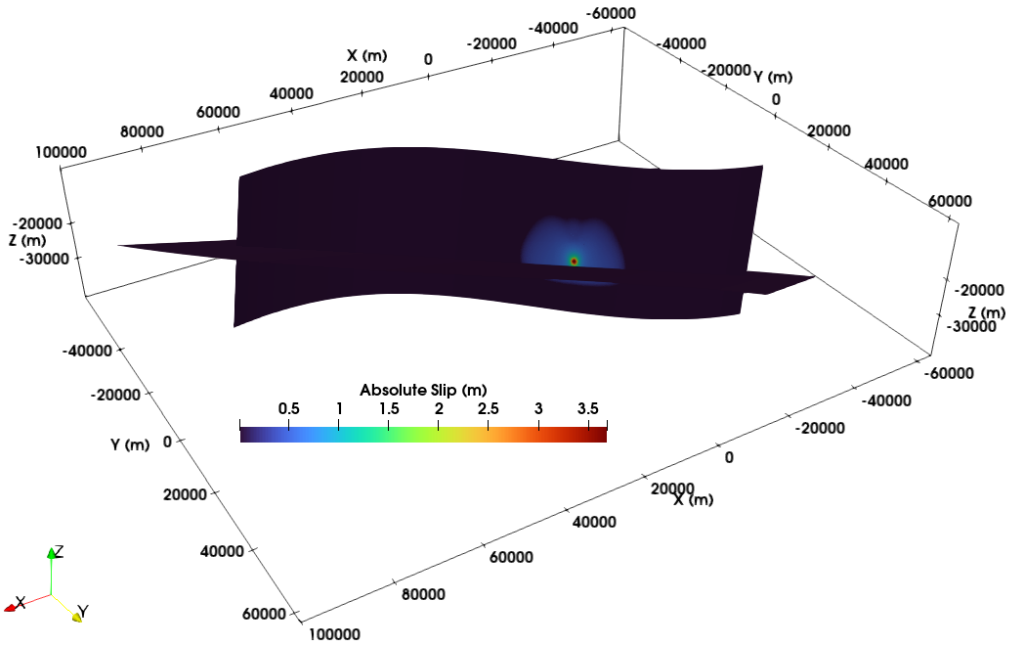


Figure 3.8: Dynamic rupture fault output of the Model-700km_r6, we show the absolute slip on the reconstructed fault plane

Figure 3.8 shows the absolute slip of Model-700km_r6 on *Mesh700km*, we can roughly estimate that the average absolute slip outside the nucleation patch is around 0.5 to 1 m. The maximum absolute slip is higher than 3.5 m within the nucleation patch.

3.3 Mesh

To generate a realistic mesh, which contains non-planar complex fault geometries from a fault trace dataset using finite elements, requires knowledge in and access to advanced meshing software. We use open-source 3D finite element mesh generator, *Gmsh* (Geuzaine and Remacle, 2009 [67]) and commercially available *SimModler* (SIMmetrix ref manual) to create and discretize our mesh. Building a high quality mesh is a laborious process and take more time than running a parameter study.

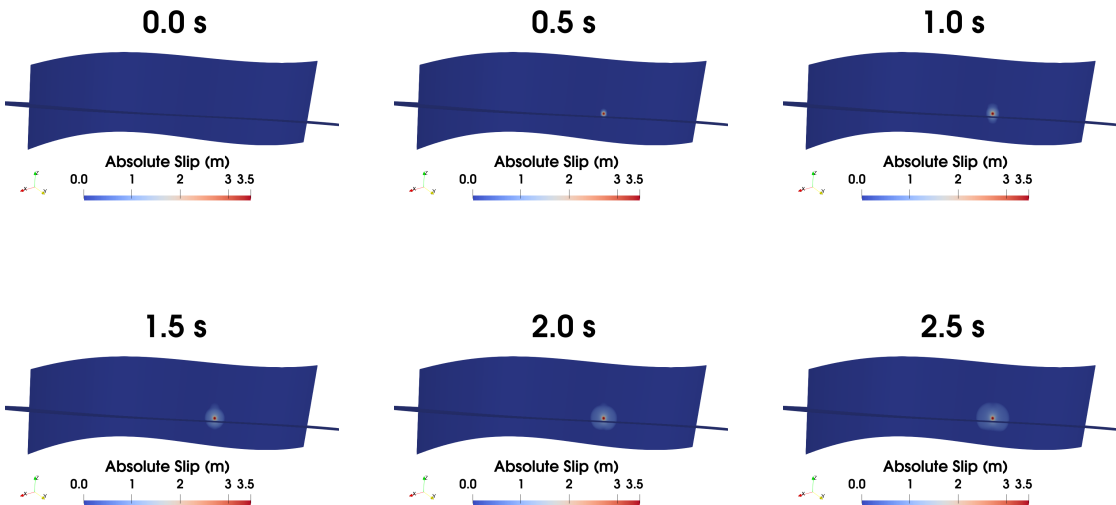
The aforementioned *Mesh700km* is based on unstructured tetrahedron girds. It consists of 2,124,064 vertices with 24,333,722 faces. The mesh resolution is coarsened away from the faults towards the boundary by applying a graduation rate of 0.5 in order to attenuate higher wave frequencies as they pass through the larger elements (Ramos et al. 2022, [55]). The absolute resolution on two fault planes is 200 m, free surface is

2000 m, and the five side faces are 10,000 m.

We select dynamic rupture solver to be *SeisSol* in *SimModeler* when implementing DR boundary conditions on the fault. And boundary conditions outside the fault include absorbing and reflecting conditions, we implement reflecting conditions on the top face of our box domain to include Earth's free surface. And absorbing conditions on the 5 side faces of the box domain to avoid artificial reflections, they could be implemented as perfectly matched layers (Komatitsch and Tromp, 2003 [68]) or as a vanishing flux condition (Kser and Dumbser, 2006 [39]), however, the absorbing condition implemented with *SimModeler* does not work well (personal conversion with Alice Gabriel), to make sure our synthetic seismogram is unaffected by the unwanted reflections from the sides, we need to make our box domain to be big enough so that the fastest P-wave can only travel from the hypocenter to the sides for the total simulation time.

Aspect ratio describes the quality of the mesh, the smaller aspect ratio, the higher mesh quality. We use aspect ratios of 6.0 for surface geometrics meshing and 12.0 for volume geometrics meshing. In the end, our resulting mesh, 700km, achieved aspect ratios smaller than 10 for 99% and smaller than 6 for 98% of its 2,124,064 tetrahedron elements. The highest aspect ratio is 11.99. Therefore, we consider our mesh has a good quality throughout.

3.4 Dynamic Rupture Process - Slip



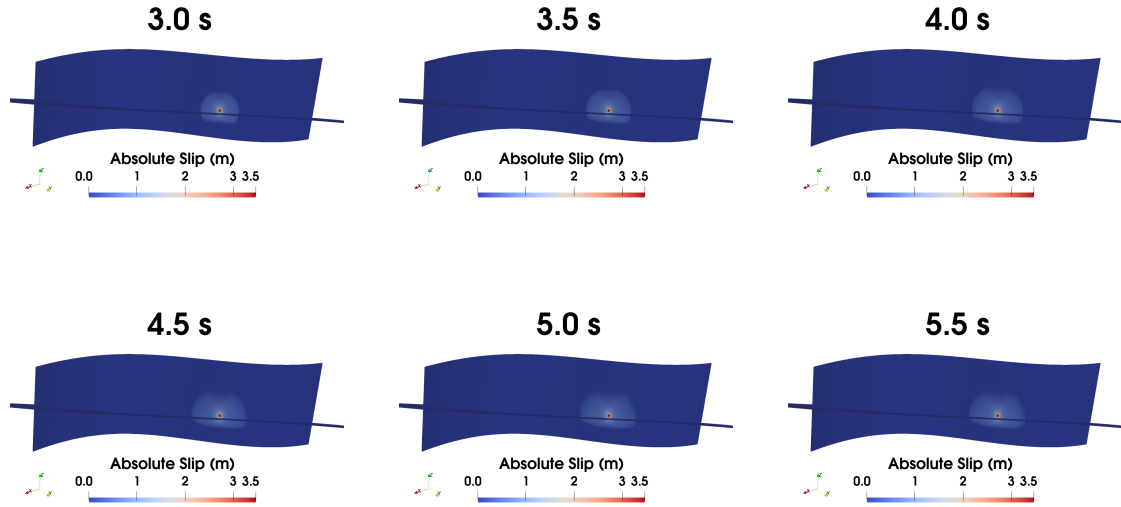
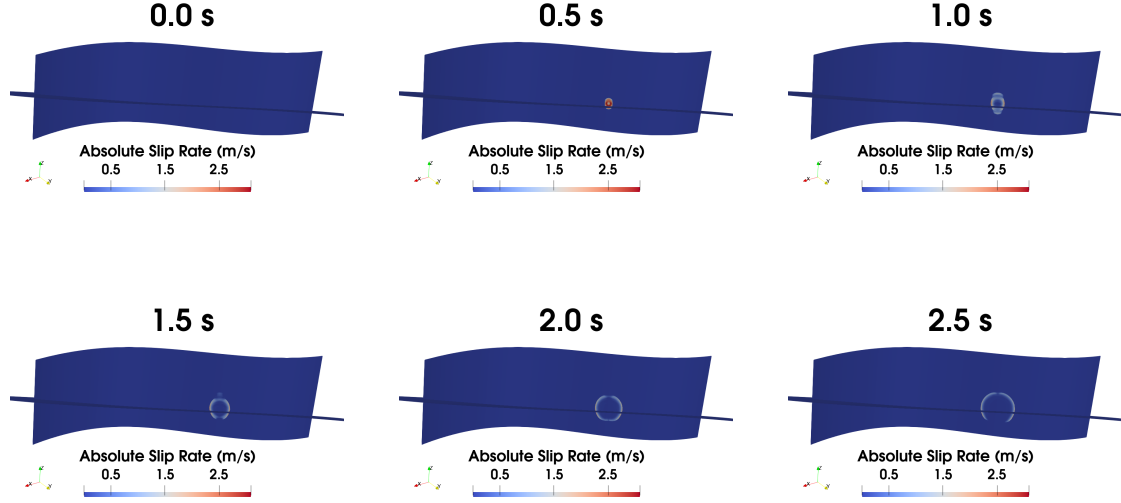


Figure 3.12: Absolute slip of Model-700km_r6 from 0 to 5.5 seconds on reconstructed fault planes

Figure 3.12 shows the temporal and spatial distribution of the absolute slip on the northeast dipping fault plane, F129. We observe the slip stopped around 5 s and the average slip outside the predefined nucleation circle is less than 1 m, this result agrees with Materna et al. (2019) [13], they conclude that the maximum slip is around 0.8 m.

3.5 Dynamic Rupture Process - Slip Rate



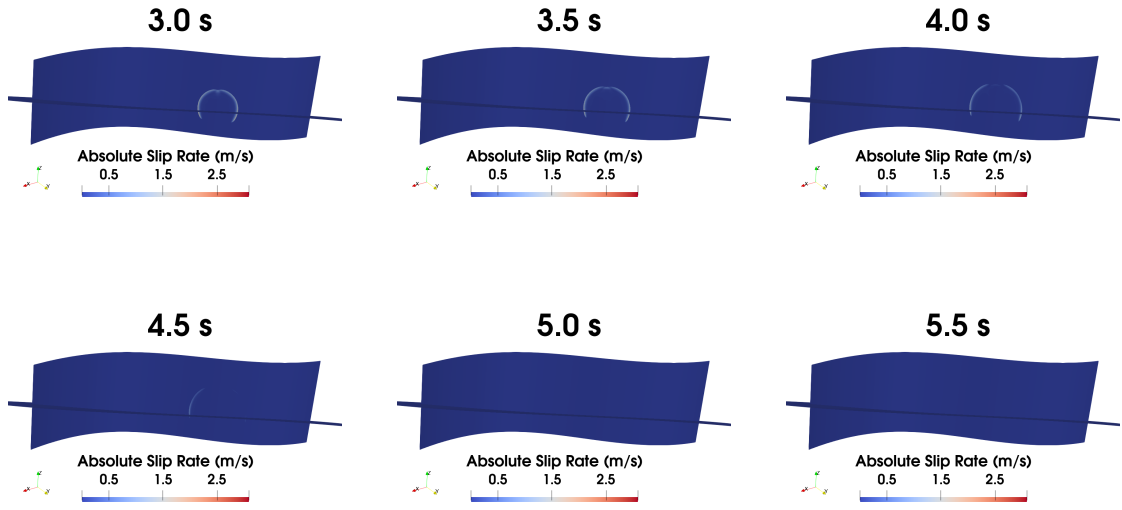


Figure 3.16: Absolute slip rate of Model-700km_r6 from 0 to 5.5 seconds on reconstructed fault planes

Figure 3.16 shows the temporal and spatial distribution of the rupture propagation. Slip rate describes how fast a particle on the fault moves during the rupture. *SeisSol* provide two fault output variables, *Sls* and *Sld*, means slip in strike and dip direction. (See Appendix C.2 for full fault output list from *SeisSol*) We calculate the L2 norm of these two variable to get the absolute slip rate as shown in **Figure 3.12**. We can see the slip rate immediately go back to zero at 5 s after the rupture, we conclude that our modelled rupture is a pulse-like event (Gabriel et al, 2013) [69].

3.6 Free Surface Output

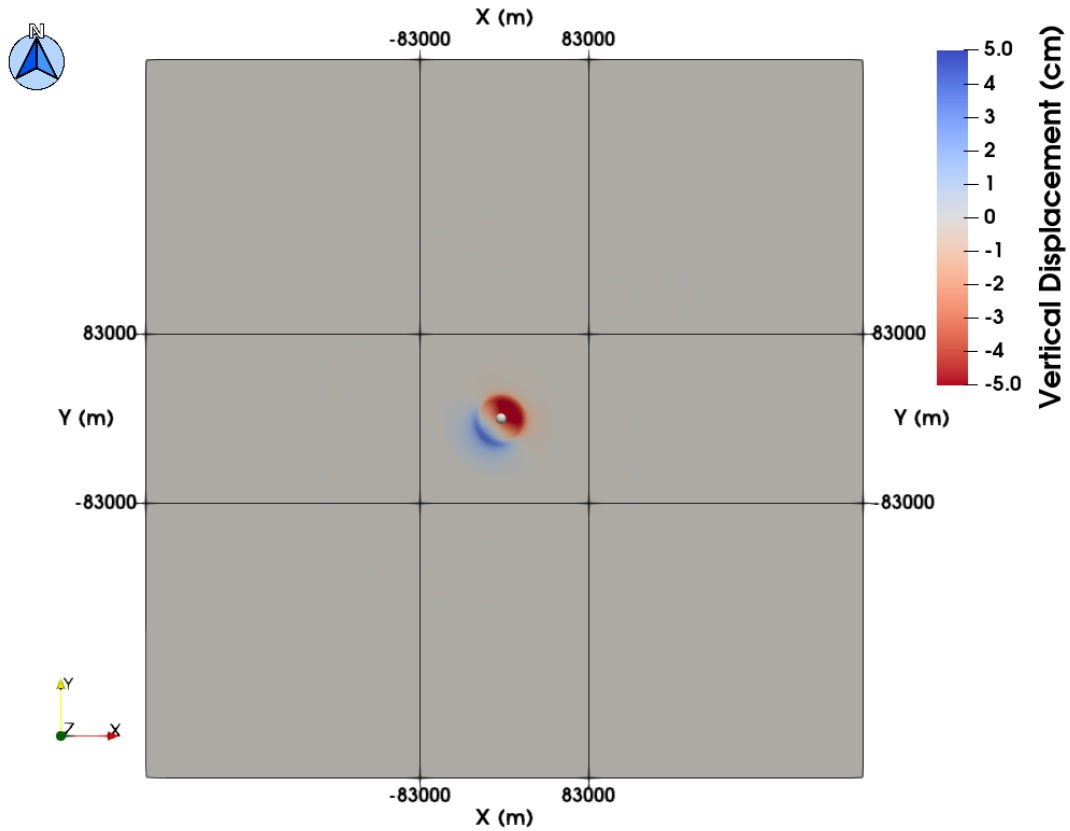
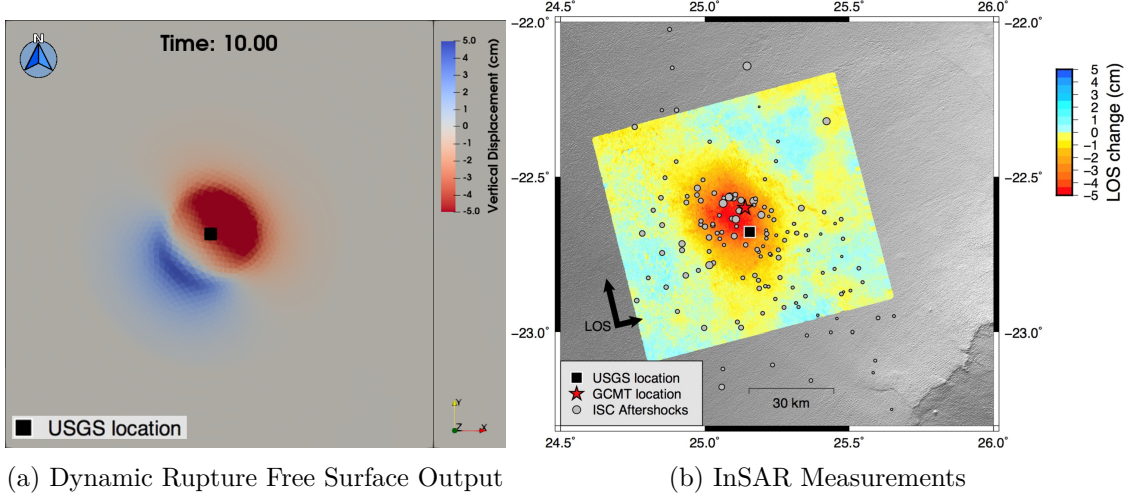


Figure 3.17: Vertical displacement plotted from free surface output of our preferred model, Model-700km_r6

Figure 3.17 shows the vertical displacement on the free surface. Vertical deformation suggests the stress buildup at these locations. We see subsidence of more than 5 cm in the epicentral area, and Materna et al. (2019) [13] have also observed subsidence in the same area with comparable value.



(a) Dynamic Rupture Free Surface Output

(b) InSAR Measurements

Figure 3.18: Vertical displacement comparison of the InSAR measurements and the free surface output (at 10 s) plotted from our preferred dynamic rupture model, *Model – 700km_r6*. Figure 3.18 (b) taken from Materna et al. (2019) [13]

Figure 3.18 shows a comparison of the InSAR measurements from Materna et al. (2019) [13] and the free surface output from our preferred DR model. The zoomed area has the same dimension as the InSAR measurements. Because 1° is approximately 111 km and 1.5° is 166 km. We plotted the free surface output at 10 seconds. These observations agree with the 2017 Botswana earthquake has a normal faulting mechanism.

3.7 Synthetic Seismograms

3.7.1 Seismological Data

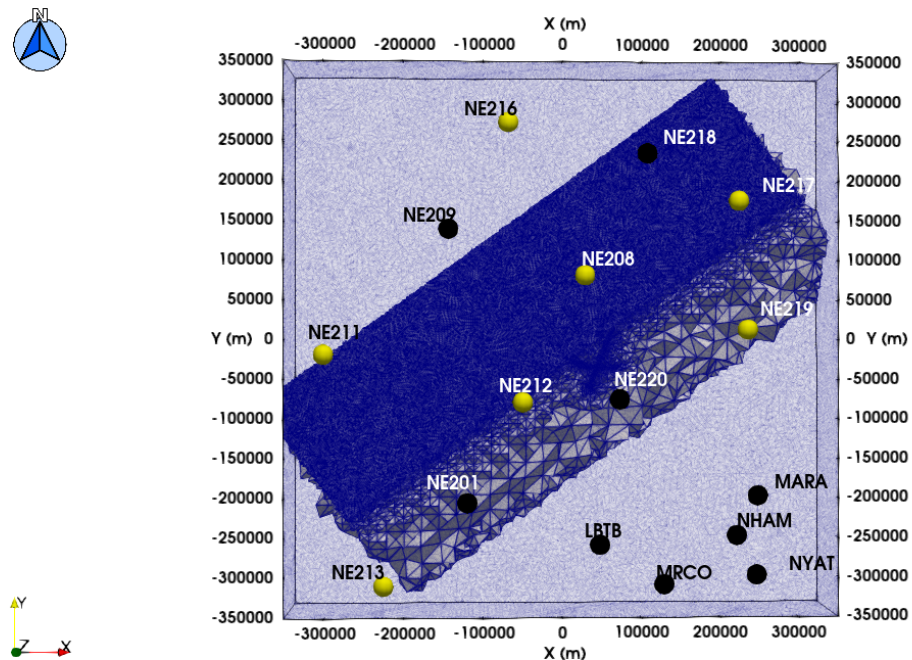


Figure 3.19: Location of the corresponding seismic stations projected on *Mesh700km*, yellow sphere represents the seismic station used in this study

Table 3.2: Seismic stations

Station	Distance [km]
NE208	91.16
NE211	302.42
NE212	97.27
NE213	384.03
NE216	283.82
NE217	286.41
NE219	237.54

Figure 3.19 shows the location of synthetic receivers projected on *Mesh700km*. We used 7 broadband seismometers from the NARS-Botswana network (see **Data & Resources**). We selected these stations because they have recorded data at the time that the 2017 Botswana earthquake took place (UTC 17:40:18, 3 April 2017). The NR network consists of 21 seismic stations and deployed from November 2013 to March 2018. **Table 3.2** shows the selected 7 stations and their euclidean distance to the hypocenter of the 2017 Botswana earthquake.

3.7.2 Comparison of the Synthetic and the Observed Seismograms

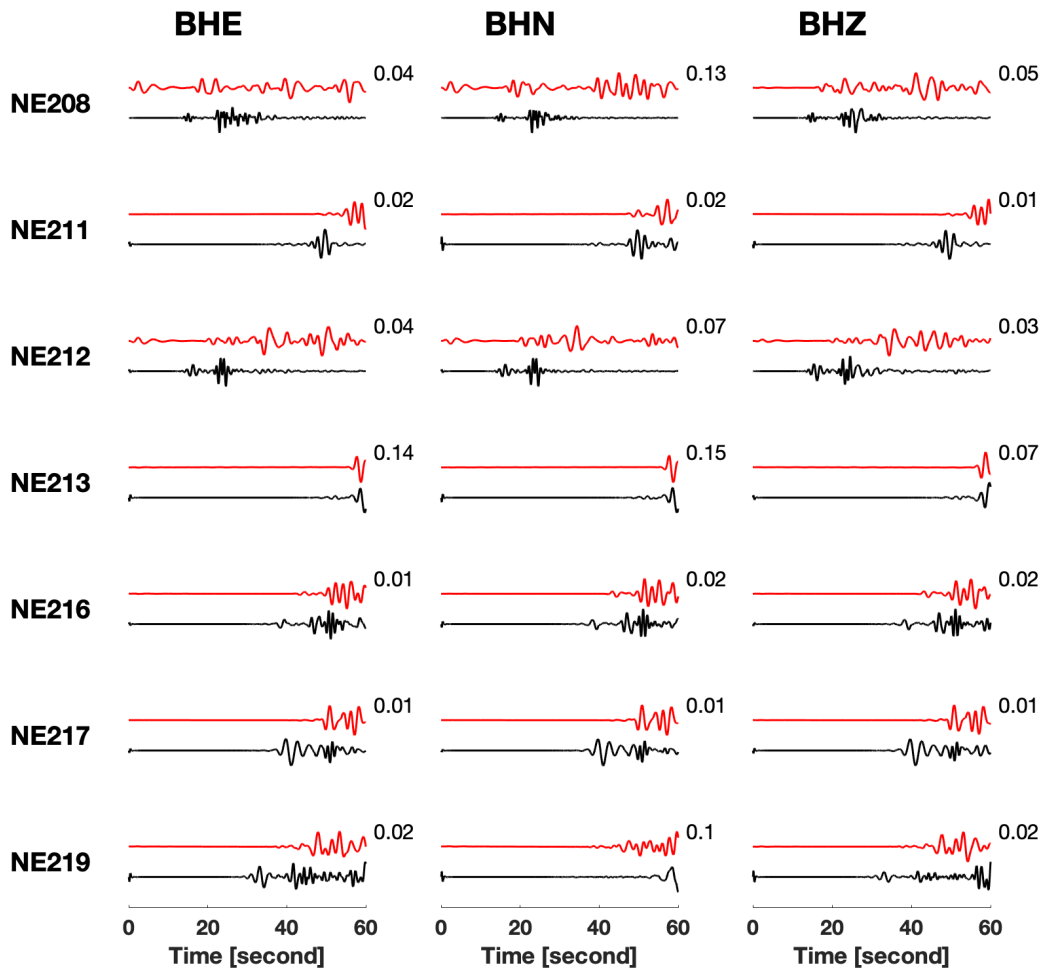


Figure 3.20: Normalized waveforms of the synthetic (black) and the observational (red) data of the 7 selected seismic stations, a 4th-order Butterworth filter [0.2, 0.6] Hz is applied to the data. The number on right upper corner is a normalization factor, which means the maximum synthetic magnitude divided by the maximum observational magnitude

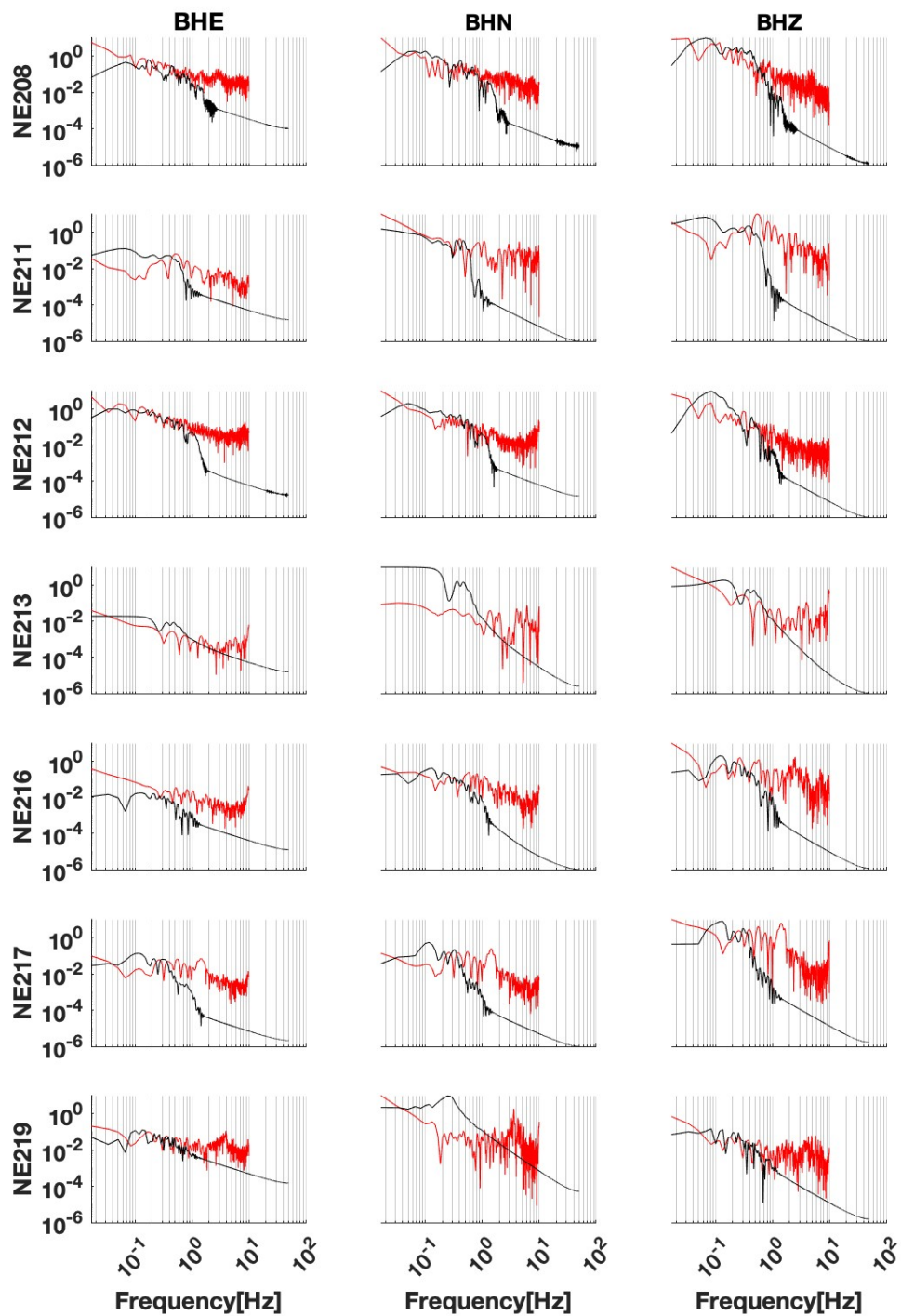


Figure 3.21: Spectrum of the synthetic (black) and the observational (red) data of the 7 selected stations

We apply a 4th-order Butterworth filter with low-cut frequency of 0.2 Hz and high-cut frequency of 0.6 Hz to both synthetic and observed seismic data. In **Figure 3.20**, we can clearly identify an earthquake signature from the synthetic data, we observe distinct P and S phase as well as the dispersion phenomenon. The starting time of the synthetic seismogram is at the earthquake time because we nucleate the rupture simultaneously. However, the comparison in **Figure 3.20** shows that the synthetic data (black) for station NE211, NE216, NE217 and NE219 arrive earlier than the observational (red), this may be due to the stations exceed the boundary of the used local 3D velocity model. Nevertheless, we observe that the polarity of the first arrival phase is comparable for almost all the stations. In **Figure 3.21**, we observe station NE208, NE212, and NE219 match the frequency content $\in [0.2 - 0.6]\text{ Hz}$.

3.7.3 Analysis Code

We acquired the observational data through IRIS DMC using python package, *Obspy*. We attached the following Python code to request, process and save the seismic data (see the Jupyter notebook, *Data_Acquisition_Botswana* in supplement).

```
from obspy.clients.fdsn import Client
from obspy import UTCDateTime
from scipy.io import savemat

t = UTCDateTime(2017, 4, 3, 17, 40, 18)

client = Client("IRIS")

NR_station_list = ["NE208", "NE211", "NE212", "NE213", "NE216", "NE217", "NE219"]

net = "NR"

for sta in NR_station_list:
    st = client.get_waveforms(net, sta, "*", "BH*", t, t+60) # Request data from the IRIS DMC

    inv = client.get_stations(network=net, station=sta, location="", channel="BH?", starttime=t, endtime=t+40,
                             level="response") # Download station response

    st1 = st.copy() # Save data to object st1 before removed instrument response
    st1.remove_response(inventory=inv) # Removed instrument response

    st2 = st1.copy() # Save data to object st2 before removed linear trend
    st2.detrend() # Removed linear trend

    st3 = st2.copy() # Save data to object st3 before filtering
    st3.filter("bandpass", freqmin=0.2, freqmax=0.6, corners=4) # Applied a Butterworth filter

    for i, tr in enumerate(st3):
        mdict = {k: str(v) for k, v in tr.stats.items()}
        mdict['data'] = tr.data
        savemat("data-" + str(sta) + "-" + str(i) + ".mat", mdict) # Save data in MATLAB format for plotting
```

Figure 3.22: Python code to request, process and save the seismic data using *Obspy*

3.7.4 Observed Seismogram

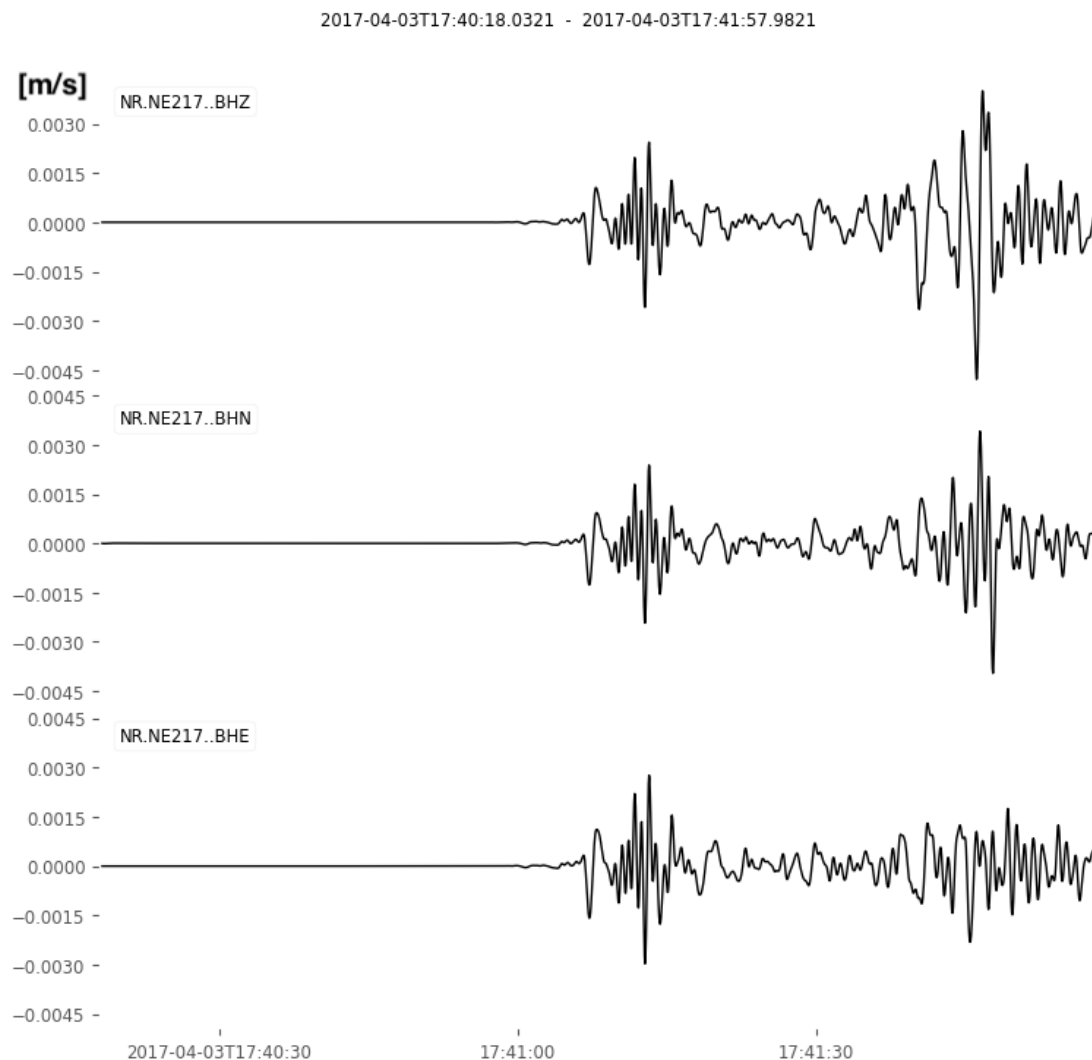


Figure 3.23: NE217, removed the instrument response, applied a 4th-order Butterworth bandpass filter with the cutoff frequencies of [0.2, 1.5] Hz

Chapter 3 Results

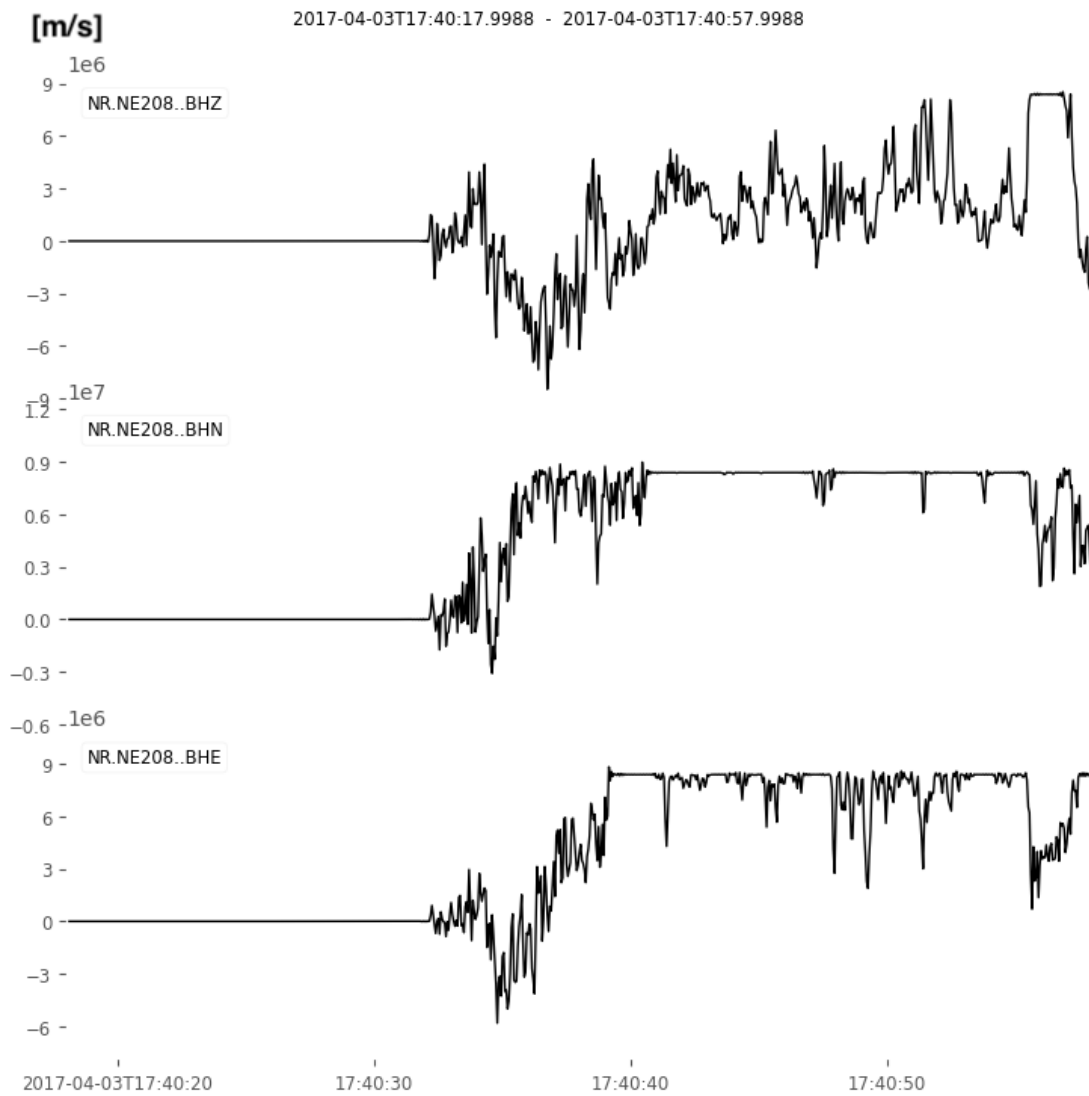


Figure 3.24: NE208, raw data

Table 3.3: Summary for All Seismic Stations inside Our Model Domain

Station	Distance <i>km</i>	Availability
LBTB	264.25	NA (Instrument response)
NE201	239.26	NA
NE208	91.16	YES (Clipped)
NE209	202.20	NA
NE211	302.42	YES (Noisy)
NE212	97.27	YES (Clipped)
NE213	384.03	YES (Noisy)
NE216	283.82	YES (Noisy)
NE217	286.41	YES (Good)
NE218	260.34	NA
NE219	237.54	YES (Clipped)
NE220	108.59	NA
MARA	317.49	NA
MRCO	355.52	NA
NHAM	332.69	NA
NYAT	386.80	NA

Figure 3.23 and **Figure 3.24** show an example of “good” and “not good” seismic recordings. The seismic waveform from station NE217 is kind of nice. After removing the instrument response and applying a 4th-order Butterworth filter with a low cut frequency of 0.2 Hz and a high cut frequency of 1.5 Hz, we can easily identify the P, S, and surface wave phases, as well as dispersion. For the other case, we can see that the seismometer NE208 is “clipped”, meaning the amplitude of the recorded waveform exceeds the upper limit of the dynamic range of the seismometer. In practice, we should not use these data to compare with our synthetics (personal communication with Fabian Lindner). However, we do not have a luxury choice, as the seismic network in Africa is very sparse. Zhang et al. (2016) [70] came up with a solution for restoration of the clipped seismograms, they found the restoration error is around 1% and 5% when clipped at 70% and 40% peak amplitude respectively for their simulated clipped-waveform data.

Table 3.3 summaries the seismic stations inside our model domain and the data availability. There are only 7 out of 16 stations that can request data from IRIS DMC at the time when the earthquake happened. However, among these 7 stations, only 1 station (NE217) recorded good quality seismic data, the others were either too noisy (NE211, NE213, and NE216) or clipped (NE208, NE212, and NE219) during the coseismic phase. The station LBTB (Network code: GT), operated by Albuquerque Seismological Laboratory (ASL), USGS, is a borehole seismometer, we can request the seismic data, but we are not able to download its instrument response. Therefore, we marked this station as not available.

Chapter 4

Discussion

Nothing in life is to be feared, it is only to be understood. Now is the time to understand more, so that we may fear less.

Marie Curie

4.1 Overview

In this chapter, we first discuss the possibility of nucleation under the lithostatic conditions. We compare two models, *Model – 5.l4* and *Model – 5.ref.hydro*, the former one nucleates under lithostatic conditions and the latter nucleates under hydrostatic conditions. Second, we discuss the observed seismogram and how could we constrain our model to improve the synthetic seismograms. Finally, we discuss the application of our DR models.

4.2 Nucleation - Lithstatic or Hydrostatic

Two models, *Model – 5.l4* and *Model – 5.ref.hydro*, from the **Table 3.1** are similar with respect to the resulting magnitude (Mw 6.35). Both of them ran on the same mesh (*Mesh4*) and nucleated at the same nucleation point (on F129). Moreover, all the input parameters are the same, except *Model – 5.l4* nucleates under lithostatic conditions ($\gamma_{nuc} = 0.95$) with a nucleation radius equal to 4 km ($r_c = 4km$) and *Model – 5.ref.hydro* nucleates under hydrostatic conditions ($\gamma_{nuc} = 0.37$) with a nucleation radius equal to 1 km ($(r_c = 1km)$). The full input parameters for both models are shown in **Table 4.1**.

Table 4.1: Full List of *SeisSol* Parameters used in Model-5_14 and Model-5_ref_hydro

<i>SeisSol</i> name	Symbol	Value	Note
-	$d_{seismogenic}$	-33000.0	User defined depth of seismogenic zone
-	d_{max}	-37000.0	User defined maximum fault depth
-	d_{min}	-5000	User defined minimum fault depth
-	ρ_{crust}	2670.0	User defined overlaying rock density
-	g	9.8	User defined gravitational constant
-	R_{ini}	0.7	User defined initial relative prestress ratio
-	R_{nuc}	4	User defined nucleation relative prestress ratio
-	γ_{ini}	0.95	User defined initial pore fluid pressure
-	γ_{nuc}	Different	User defined nucleation pore fluid pressure
-	x_c	-3446.35	User defined nucleation coordinate in x-axis
-	y_c	5.21499	User defined nucleation coordinate in y-axis
-	z_c	-29000.0	User defined nucleation coordinate in z-axis
-	r_c	Different	User defined nucleation radius
-	ρ	3330.0	User defined background rock density
-	λ	81235350000.0	User defined Lamé's first parameter
-	μ	65942325000.0	User defined Lamé's second parameter
mu_d	μ_d	0.1	Andersonian Stress input parameter
mu_s	μ_s	0.6	Andersonian Stress input parameter
SH_max	SH_{max}	132.0	Andersonian Stress input parameter
S_v	S_v	1	Andersonian Stress input parameter
cohesion	-	0.0	Andersonian Stress input parameter
s2ratio	ν	0.5	Andersonian Stress input parameter
rs_a	$a(x)$	0.01	Rate-and-State friction law input parameter
RS_b	b	0.014	Rate-and-State friction law input parameter
RS_sr0	V_0	10^{-6}	Rate-and-State friction law input parameter
RS_sl0	L	0.1	Rate-and-State friction law input parameter
RS_srW	$V_W(x)$	0.1	Rate-and-State friction law input parameter
RS_f0	f_0	0.6	Rate-and-State friction law input parameter
Mu_W	f_W	0.1	Rate-and-State friction law input parameter
RS_iniSlipRate1	V_{ini}	10^{-16}	Rate-and-State friction law input parameter
t_0	t_0	0.4	Rate-and-State friction law
CFL	-	0.5	Courant–Friedrichs–Lowy condition
EndTime	t_{total}	10.0	Simulation stop criterion

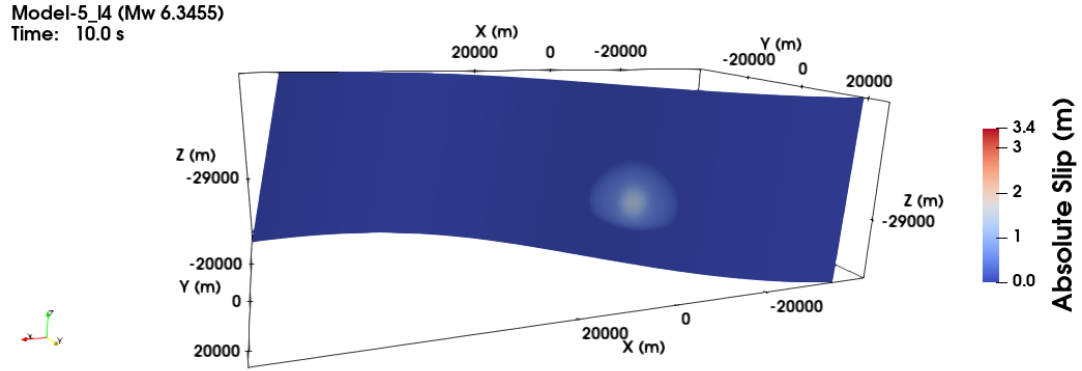


Figure 4.1: Absolute slip (ASI) of Model-5_l4 on reconstructed fault F129

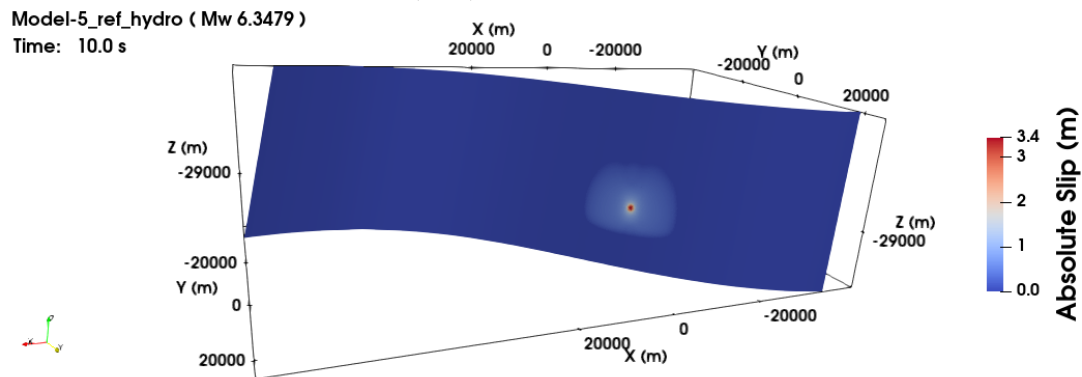


Figure 4.2: Absolute slip (ASI) of Model-5_ref_hydro on reconstructed fault F129

Figure 4.1 and **Figure 4.2** show the absolute slip (ASI) output of the two models, we observe that the size of the nucleation area is similar (average radius of 17500 m), but the maximum slip is significantly larger for the hydrostatic case (3.4 m) compare to the lithostatic case (1.3 m) at the nucleation point.

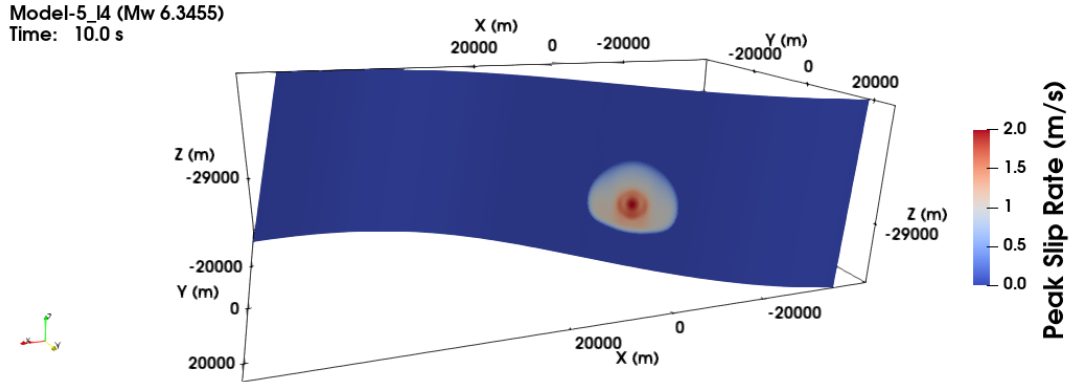


Figure 4.3: Peak slip rate (PSR) of Model-5_l4

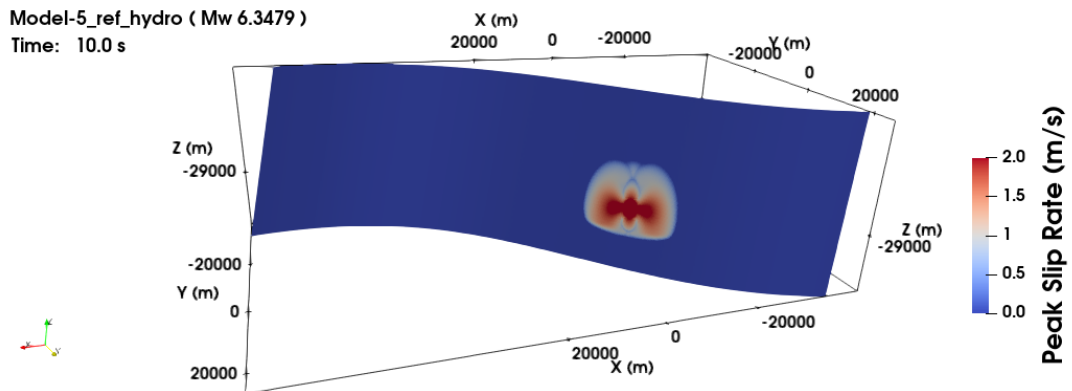


Figure 4.4: Peak slip rate (PSR) of Model-5_ref_hydro

Figure 4.3 and **Figure 4.4** show the Peak Slip Rate (PSR) output of the two models, we observe that the maximum PSR is significantly larger for the hydrostatic case (12.8 m/s) compare to the lithostatic case (2.0 m). The distribution of the PSR for the hydrostatic model looks like a “Bat”.

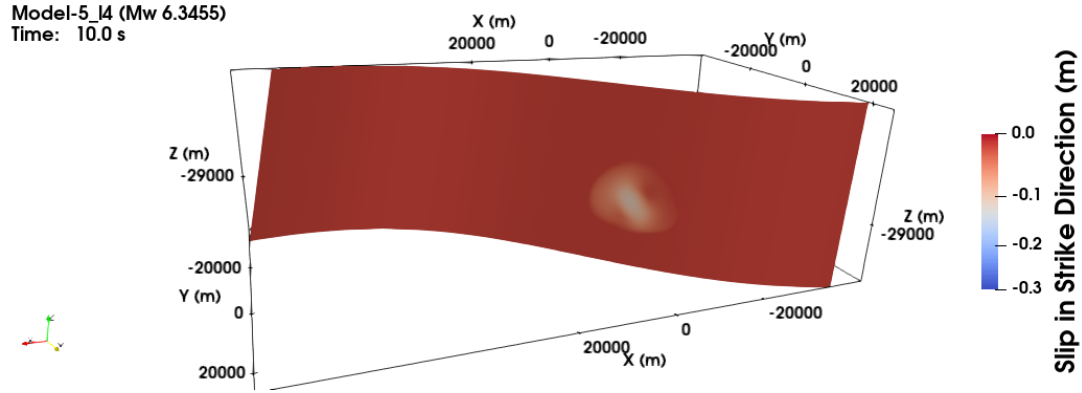


Figure 4.5: Slip in strike direction (Sls) of Model-5_I4

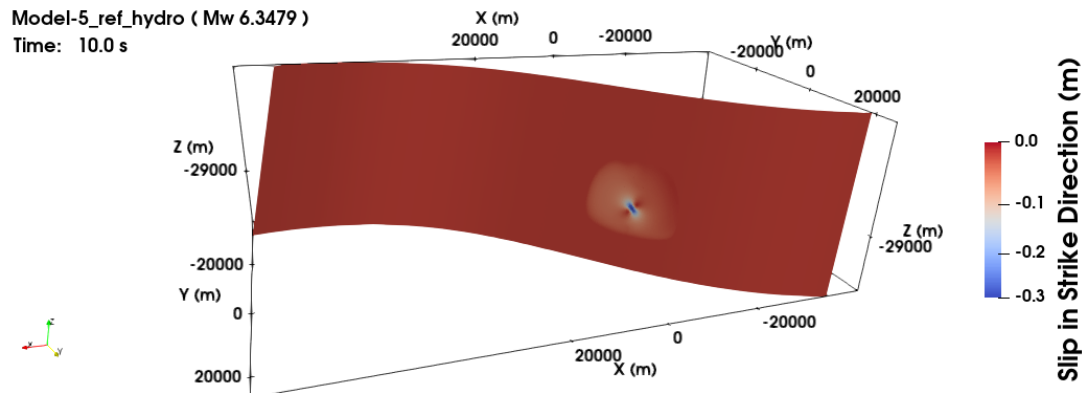


Figure 4.6: Slip in strike direction (Sls) of Model-5_ref.hydro

Figure 4.5 and **Figure 4.6** show the Slip in Strike direction (Sls) output of the two models, we observe that the Sls is higher in the hydrostatic case.

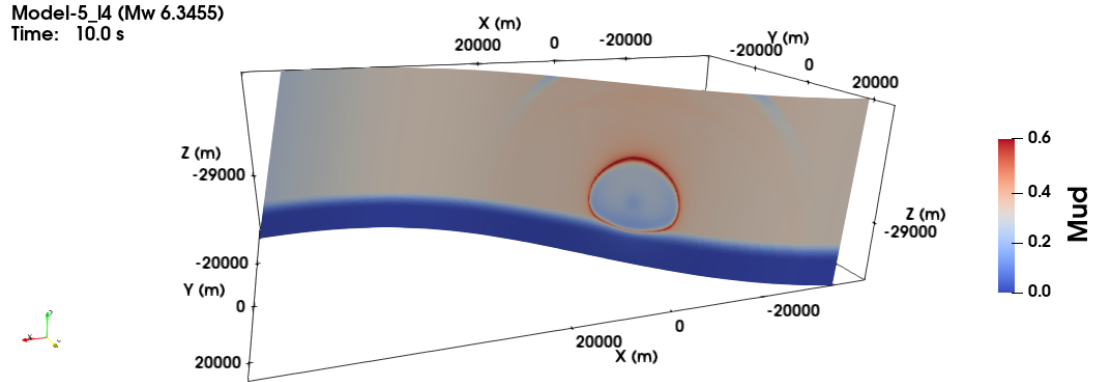


Figure 4.7: Current friction coefficient (Mud) of Model-5_l4

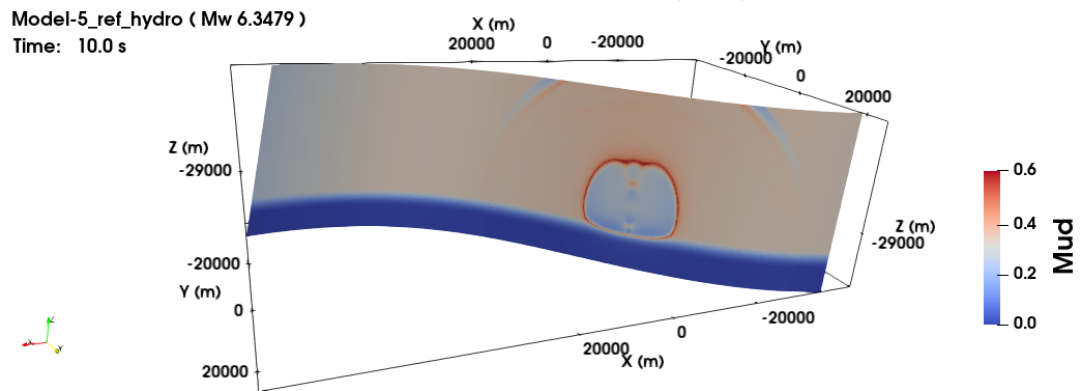


Figure 4.8: Current friction coefficient (Mud) of Model-5_ref_hydro

Figure 4.7 and **Figure 4.8** show the Current Friction Coefficient (Mud) output of the two models, we observe that the Mud value is comparable. This is expected as we use the same friction law parameters for both models.

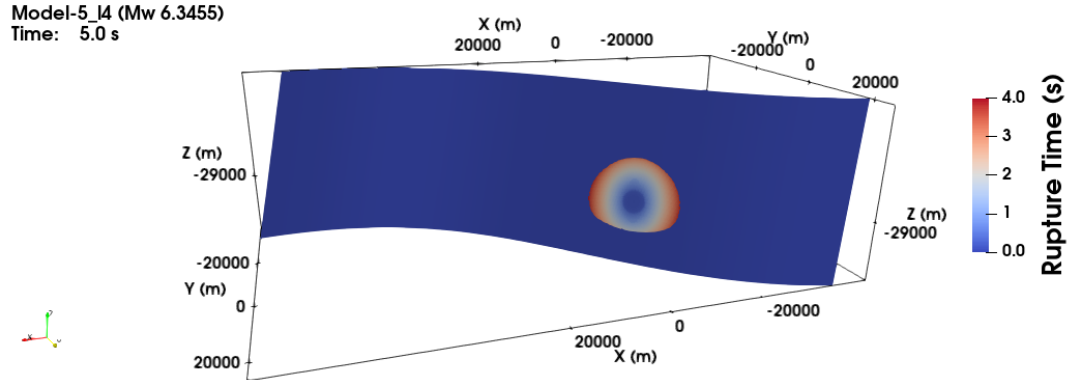


Figure 4.9: Rupture time (RT) of Model-5_I4

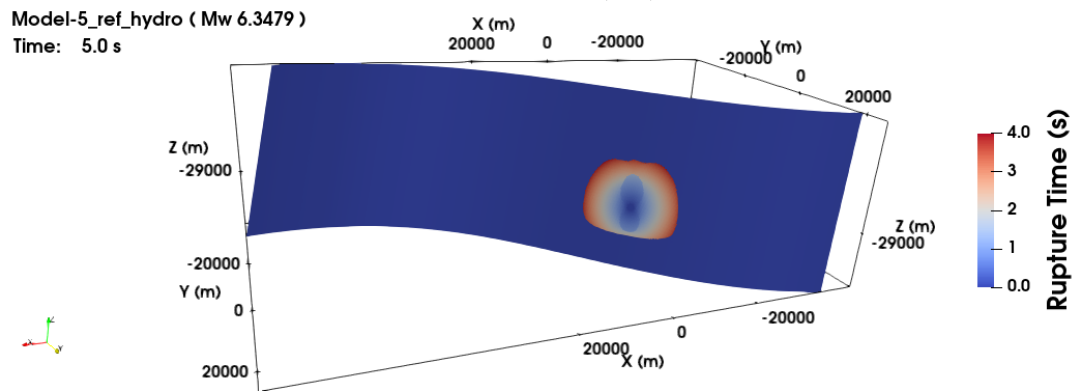


Figure 4.10: Rupture time (RT) of Model-5_ref_hydro

Figure 4.9 and **Figure 4.10** show the Rupture Time (RT) output of the two models, we observed that the RT is also comparable for the two models. We observe that the hydrostatic case has a radiative pattern extends upwards and downwards around the nucleation point.

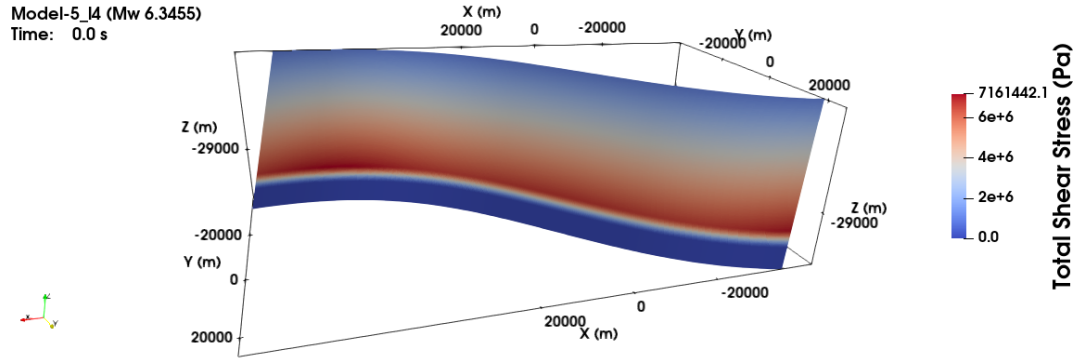


Figure 4.11: Initial total shear stress of Model-5_l4

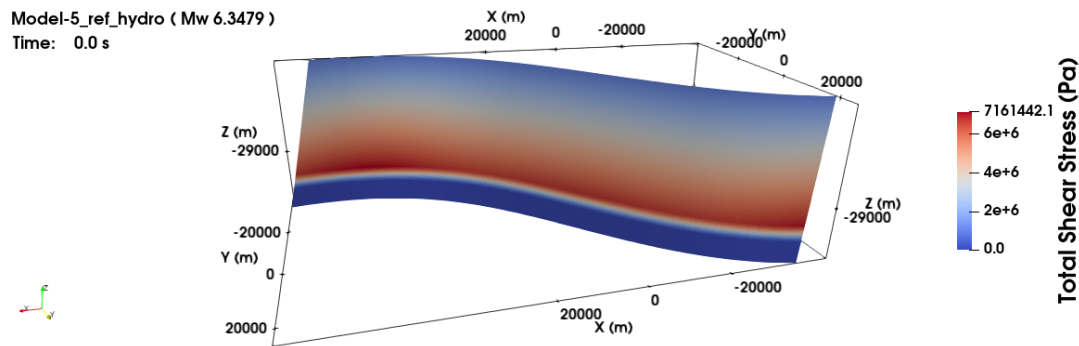


Figure 4.12: Initial total shear stress of Model-5_ref_hydro

Figure 4.11 and **Figure 4.12** show the total initial shear stress output of the two models, it is calculated from the variable $Td0$ and $Ts0$. We observe that the total initial shear stress is the same for the two models.

Chapter 4 Discussion

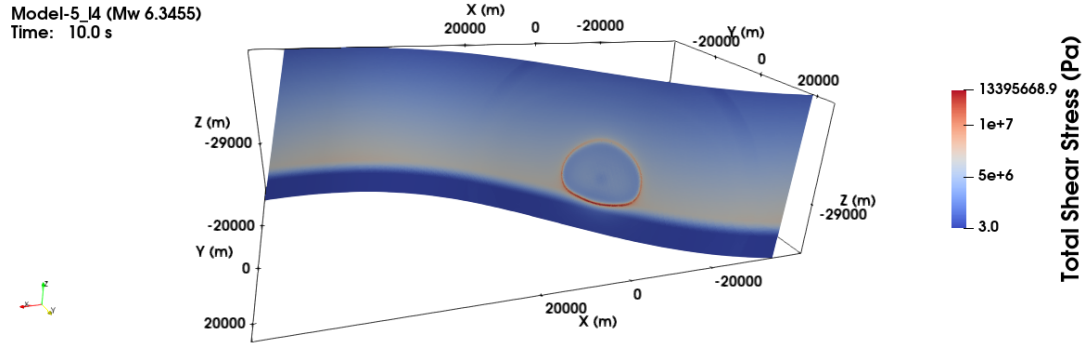


Figure 4.13: Total shear stress at 10 seconds of Model-5_I4

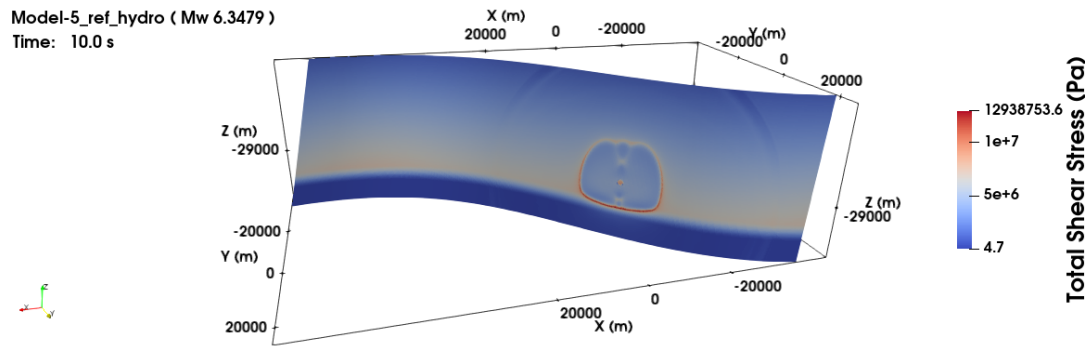


Figure 4.14: Total shear stress at 10 seconds of Model-5_ref_hydro

Figure 4.12 and **Figure 4.13** show the total shear stress (at 10s) output of the two models, it is calculated from the variable $Td0$ and $Ts0$. We observe that the total shear stress after the rupture is comparable for the two models.

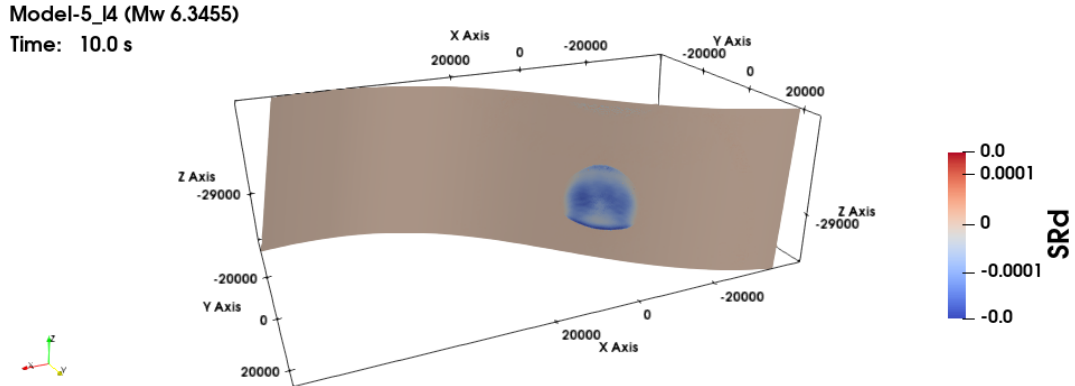


Figure 4.15: Slip Rate in dip direction (SRd) at 10 seconds of Model-5_l4

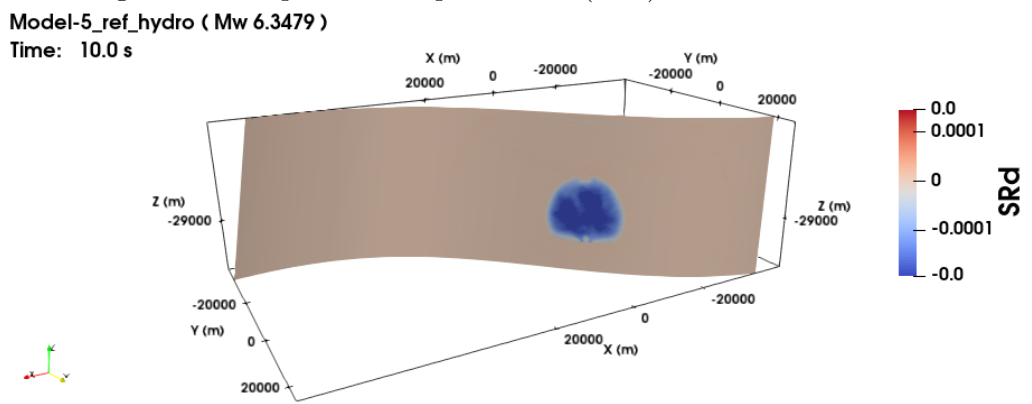


Figure 4.16: Slip Rate in dip direction (SRd) at 10 seconds of Model-5_ref_hydro

Figure 4.14 and **Figure 4.15** show the Slip Rate in dip direction (SRd) (at 10 s) output of the two models. We observe that SRd at 10 s is larger for the hydrostatic case.

Table 4.2: Comparison Summary for Model-5_l4 and Model-5_ref_hydro

SeisSol name	Physical meaning	Note
SRs	Slip rates in strike direction	Different
SRd	Slip rates in dip direction	Different
u_n	Normal velocity	Comparable
Mud	Current friction	Comparable
StV	state variable	Comparable
Ts0	shear stress in strike direction	Comparable
Td0	shear stress in dip direction	Comparable
Pn0	normal stress	Comparable
Sls	slip in strike direction	Different
Sld	slip in dip direction	Different
ASI	Absolute slip	Different
PSR	Peak slip rate	Different
RT	rupture time	Comparable

Table 4.2 is a summary for the comparison of Model-5_l4 and Model-5_ref_hydro. For the full *SeisSol* fault output, see Appendix C.2.

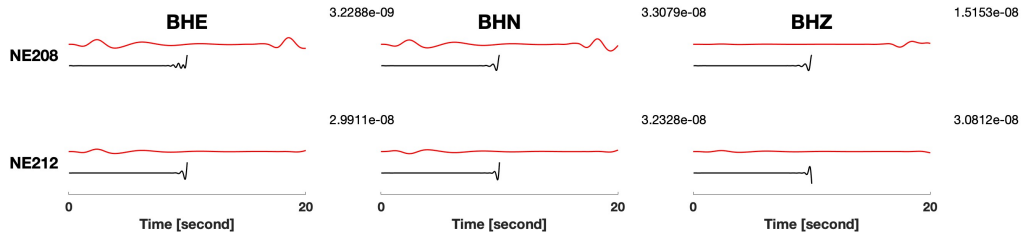


Figure 4.17: Filtered synthetic (black) and observed (red) waveforms of Station NE208 and NE212 for Model-5_l4, a 4th-order Butterworth filter [0.2, 0.6] Hz is applied to the data. The number on right upper corner is a normalization factor, same as before

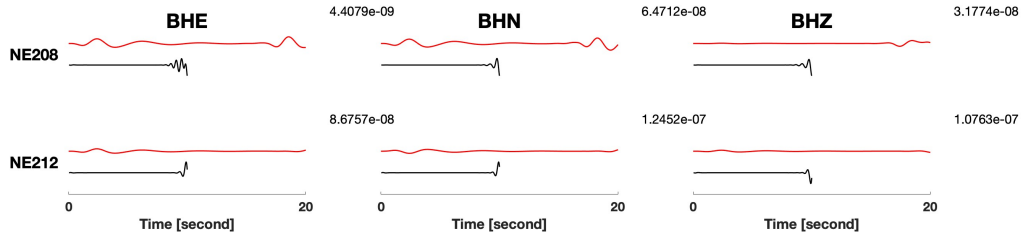


Figure 4.18: Filtered synthetic (black) and observed (red) waveforms of Station NE208 and NE212 for Model-5_ref_hydro, a 4th-order Butterworth filter [0.2, 0.6] Hz is applied to the data. The number on right upper corner is a normalization factor, same as before

Figure 4.18 shows the filtered waveforms from the two models. We applied a Butterworth 4th order filter with cutoff frequencies of [0.2, 0.6] Hz. Because we ran the two models on the smaller mesh (*Mesh4*) with short simulation time (10 s), we only obtained very limited signal from two nearby seismic stations, NE208 and NE212. Based on these few signals, we suspect the synthetic seismogram of the lithostatic and hydrostatic models are different.

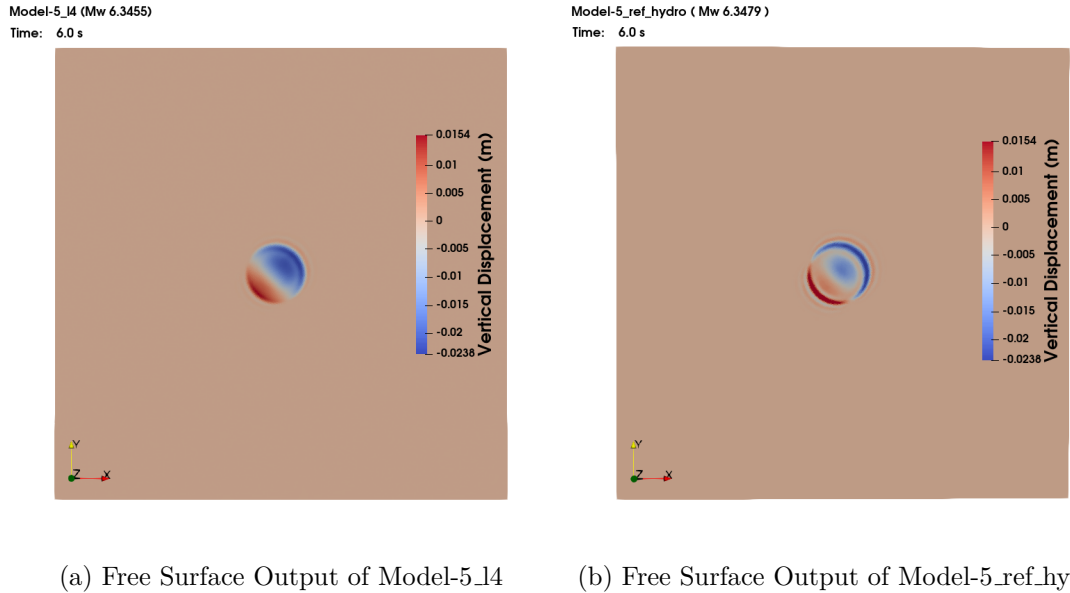


Figure 4.19: Free surface output (at 6 s) for Model-5_l4 and Model-5_ref_hydro

Figure 4.19 shows the free surface output for Model-5_l4 and Model-5_ref_hydro, plotted at 6 s. We observe that they are comparable in respect to size of magnitude of the subsidence, but the hydrostatic case seem has a more complicated pattern than the lithostatic case.

To conclude, Model-5_l4 and Model-5_ref_hydro show the rupture is mechanic viable under both lithostatic and hydrostatic conditions. We can either refute or prove the 2017 Botswana earthquake is triggered by fluid. But the elevated hot fluid from the upper mantle is a plausible explanation based on our DR models. Overall, the characteristics of both models are similar, we prefer the model nucleates under hydrostatic conditions because it has a smaller predefined nucleation patch, thus more plausible to have a runaway rupture.

4.3 Error Analysis - How can we improve the synthetic seismogram?

In general, there are two sources of errors for a physics-based model. First, the input parameter is not completely accurate, in fact, many parameters contain some kind of uncertainty, for example, the nucleation location, we have chosen a point on the fault as close to the origin as possible, but very likely it does not represent the real nucleation point. Second, the physics is not perfect, we solve the seismic wave propagation assuming a purely elastic and isotropic media, but the real earth is inelastic and anisotropic, especially for a deep event. However, even if we consider attenuation and anisotropy, the equations still can not be perfect because many processes occurred at microscopic scale which may have a profound effect on the rupture process. Such as hydrologic processes, melting and flash heating, thermal pressurization and silica gel formation (Beroza and Kanamori, 2015 [22]). Einstein once asked, “Do God throw a dice?”, the quantum theory tells us that “not only does God definitely play dice, but He sometimes confuses us by throwing them where they can’t be seen.” (Hawking, 2009 [71]).

4.3.1 3D Velocity Model

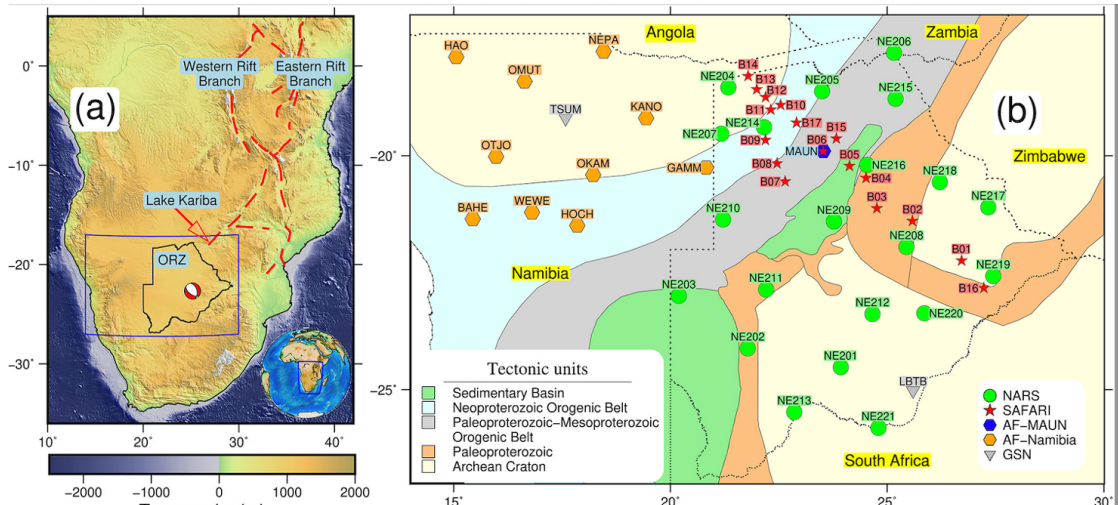


Figure 4.20: The 3D velocity model domain and seismic stations used for the inversion, figure taken from Fadel et al. (2020) [36]

The local 3D velocity model used for the material model conversion has a dimension of $220 \text{ km} \times 218 \text{ km} \times 20 \text{ km}$, which is smaller than our model domain (*Mesh700km*). Only two seismic stations, NE208 and NE212, are inside the converted material model domain. We use homogenous elastic material properties for the grid points outside the material model (see Appendix B.1.4). We think that this homogeneity is the main source

of errors for our synthetic seismograms. To solve this problem, we can use the 3D shear velocity model from Fadel et al. (2020) [36], which covers our entire model domain. **Figure 4.20** shows the domain of the 3D shear velocity model and the seismic stations used for inverting this model.

4.4 Application

The reliable in-situ stress measurements are rare in Botswana. The World Stress Map 2016 graded the stress measurements in Botswana to E-quality due to the large errors in over-coring measurements and replacement measurements have not been conducted (Materna et al. (2019) [13]). However, these measurements of stress are key to understanding the genesis of the Botswana earthquake. The static stress drop from the Botswana earthquake is only around 1 MPa , which is much smaller than the stress drop of most intraplate earthquakes (Kanamori and Anderson, 1975 [72]), a low-stress drop would indicate relative high-frequency radiation. Unfortunately, there is no near-field strong motion data to verify this theory (personal conversion with Roland Bürgmann).

Dynamic rupture models could potentially compensate for the poor measurements in the Botswana region, we can generate strong ground motion data by placing receivers close to the fault in our computational model. In Appendix C.3, we show the synthetic seismograms of all the seismic stations from the **Table 3.3**. At first, dynamic rupture simulations were performed primarily to understand the rupture itself, only recently have they been used in connection with strong ground motion simulations and to model real observations (Igel, 2017 [40]).

Our DR simulations show that we can simulate a fluid-triggered rupture scenario and obtain some critical parameters, such as the size of the fluid reservoir and the magnitude of the resulting earthquake. This leads to applications including study induced earthquakes caused by geothermal production and hydraulic fracturing.

Chapter 5

Conclusion

Modern science is not content with creating theories. It uses these theories in order to acquire new powers, and in particular to develop new technologies.

Yuval Noah Harari, The Hebrew University of Jerusalem

5.1 Overview

In this chapter, we first summarize some key findings from our preferred DR model, we conclude that the 2017 Botswana earthquake is most likely triggered by a transient stress increase on a critically loaded fault. Second, we discuss the ultimate goal of a physics-based earthquake model - to predict future earthquakes. In the end, we discuss future work.

5.2 Key Findings from our Preferred DR Model

We have built a physics-based model for the 2017 Botswana earthquake. Some features of our model: (1) state-of-the-art 3D dynamic rupture model, (1) use non-planar fault, (2) heterogeneous medium (include 3D material properties), (3) assume purely elastic medium (no plasticity), (4) use state-of-the-art Rate-and-State friction law.

Our preferred model favours the deep fluid triggering hypothesis that has been put forward by Gardonio et al. (2018) [4] because nucleation under hydrostatic conditions is more plausible to have runaway rupture (personal communication with Alice Gabriel). In chapter 3, we have compared the synthetics to the observations, we can not say that they match very well, but our preferred model is able to capture some of the important attributes of the observed data. For example, the polarity of the first arrival in synthetic seismograms is comparable to the observed data and the subsidence in free surface output agrees with the InSAR measurements. Based on our preferred model, the earthquake ruptured under hydrostatic conditions with a nucleation radius equal to 1060 meters. However, the 2017 Botswana earthquake can also occur under lithostatic conditions with a larger nucleation radius. Both ruptures are dynamically viable. Seismic moment tensor solutions and geodetic inversions for a deep event like the 2017 Botswana earthquake suffers from nodal-plane ambiguities (Materna et al. (2019) [13]

and Gardonio et al. (2018) [4]). Our preferred DR model resolved this ambiguity, we found the southwest dipping fault plane, F126, is not able to hold a rupture scenario at the target magnitude (i.e. Mw 6.46) and concluded that the rupture is most likely to occur on the northeast dipping fault plane, F129, which has a dip angle of 74° and a strike angle of 129° . The lower crust is around 35 km thick in the epicentral area (Nguuri et al., 2001 [73]; Tedla et al., 2011 [74]; Youssof et al., 2013 [75]), the depth of this event is placed at 29 km in our preferred model, thus we conclude the earthquake likely took place above the lower crust based on our preferred model. We have also made a movie of the rupture of the 2017 Botswana earthquake (see Zenodo supplement).

5.3 Holy Grail of Seismology

Earthquake prediction can be fairly called the holy grail of seismology. Based on today's technology, could we have predicted the 1755 great Lisbon earthquake or any other earthquakes? The answer is no, we can only make predictions based on what we understand, for example, we can make a prediction that for the next decades, there will be much more earthquakes will occur in California than in Germany, because California is close to the border of tectonic plate boundaries, while Germany is located on the stable continental region. However, the ability to predict a specific earthquake with accurate location, size and time has not been realized (obviously). In the seismology community, it is axiomatic that the prediction of earthquakes on short timescales is impossible. A nature paper titled, "*Japan must admit they cannot predict earthquakes*" by Geller (2017) [76] is an exemplary example.

Moorkamp et al., (2019) [1] explained the 2017 Botswana earthquake as a concentrated strain response in a reactivated preexisting zone of weakness. The concept has been applied to specific earthquakes such as the New Madrid earthquake sequence (Kenner and Segall, 2000; Pollitz et al., 2001), and has been proposed as a mechanism for the persistent weakness of craton margins during supercontinent cycles (Audet and Bürgmann, 2011 [77]; Lenardic et al., 2000 [78]).

5.4 Future Work and Outlook

Earthquake physics is highly multidisciplinary, to make better earthquake models, we need a board collaboration from seismology, engineering, geology, geodynamics, mineralogy, petrophysics and many other fields.

Materna et al. (2018) [13] have produced a kinematic model based on a geodetic and teleseismic joint inversion. Based on the kinematic model from Materna et al. (2019)

Chapter 5 Conclusion

[13]. There are two main asperities of the rupture, the deeper portion of the fault ruptured first, had a short rise time (less than 1 s), and the shallower portion of the rupture had a longer rise time (greater than 2 s). The moment rate function also shows two distinct peaks, a feature also seen in the SCARDEC solution for the event (Vallee et al., 2011 [79]). These features of the rupture may indicate that the fault contains a heterogeneous structure of asperities with locally differing stress conditions or frictional properties. We can use this kinematic model by following the approach introduced by Tinti et al. (2021) [80] to constrain the initial stress conditions in our DR model and improve our synthetic data. Furthermore, we can validate the mechanic viability of the kinematic model (see Appendix D.1).

Appendix A

A.1 Source Parameters from CMT and USGS

Region name: BOTSWANA

Date (y/m/d): 2017/4/3

Information on data used in inversion

Wave	nsta	nrec	cutoff
Body	167	412	40
Mantle	156	288	125
Surface	171	450	50

Timing and location information

	hr	min	sec	lat	lon	depth	mb	Ms
PDEW	17	40	18.60	-22.68	25.16	29.0	0.0	6.5
CMT	17	40	24.38	-22.54	25.21	30.0		
Error			0.05	0.00	0.00	0.1		
Assumed half duration:				4.3				

Mechanism information

Exponent for moment tensor:	25	units: dyne-cm				
Mrr	Mtt	Mpp	Mrt	Mrp	Mtp	
CMT	-6.290	2.600	3.700	-1.820	0.002	-4.010
Error	0.033	0.026	0.028	0.051	0.053	0.021

$M_w = 6.5$	Scalar Moment = 7.01e+25
Fault plane:	strike=332 dip=41 slip=-70
Fault plane:	strike=126 dip=51 slip=-107
Eigenvector:	eigenvalue: 7.30 plunge: 5 azimuth: 228
Eigenvector:	eigenvalue: -0.58 plunge: 13 azimuth: 137
Eigenvector:	eigenvalue: -6.72 plunge: 76 azimuth: 339
Eigenvector:	eigenvalue: -0.58 plunge: 13 azimuth: 137
Eigenvector:	eigenvalue: -6.72 plunge: 76 azimuth: 339

Figure A.1: A screenshot of CMT Web Page on the 2017 Botswana event, red circles the relevant parameters for our DR simulations

Appendix A

Contributed by USGS³ last updated 2017-06-23 07:26:28 (UTC)

- ✓ The data below are the most preferred data available
- ✓ The data below have been reviewed by a scientist

W-phase Moment Tensor (Mww)

Moment	6.188e+18 N·m
Magnitude	6.46 Mww
Depth	23.5 km
Percent DC	90%
Half Duration	4.44 s
Catalog	US
Data Source	USGS ³
Contributor	USGS ³

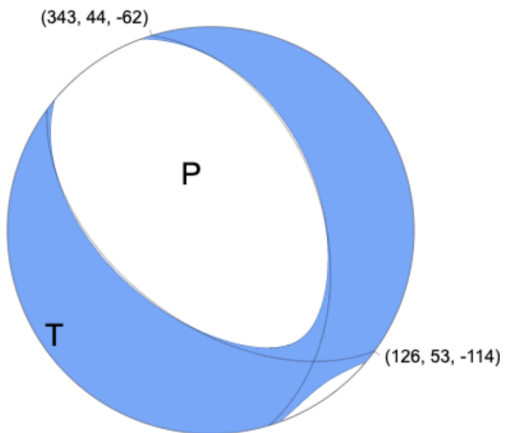


Figure A.2: A screenshot of the webpage of the USGS W-phase Moment tensor solution and focal mechanism (beach ball), red circles emphasize the relevant parameters for our DR simulations

A.2 3D Resistivity Model

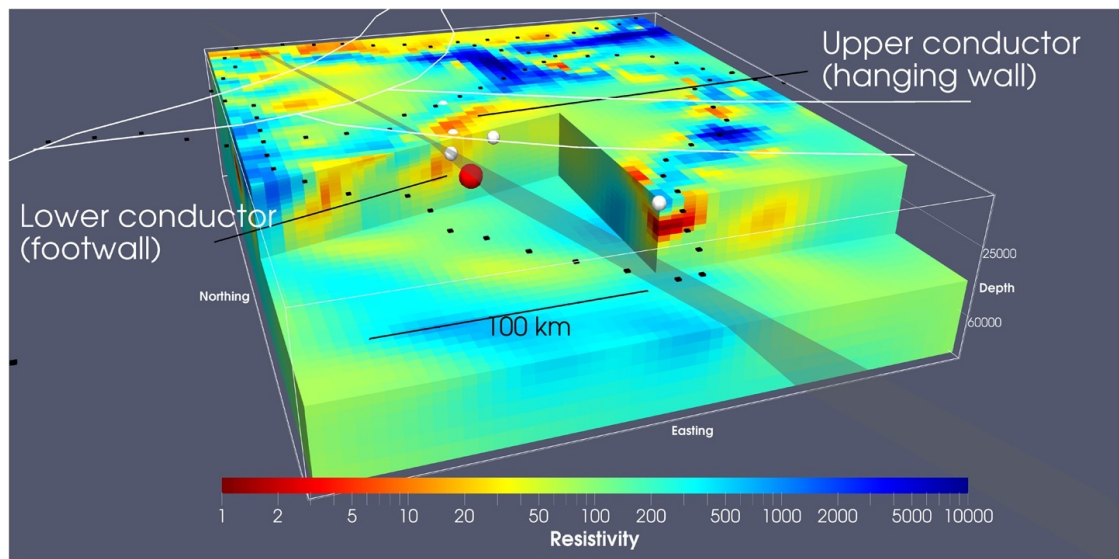


Figure A.3: 3D resistivity model, taken from Moorkmap et al., (2019) [1]

A.3 Fault Traces at 5 km Depth

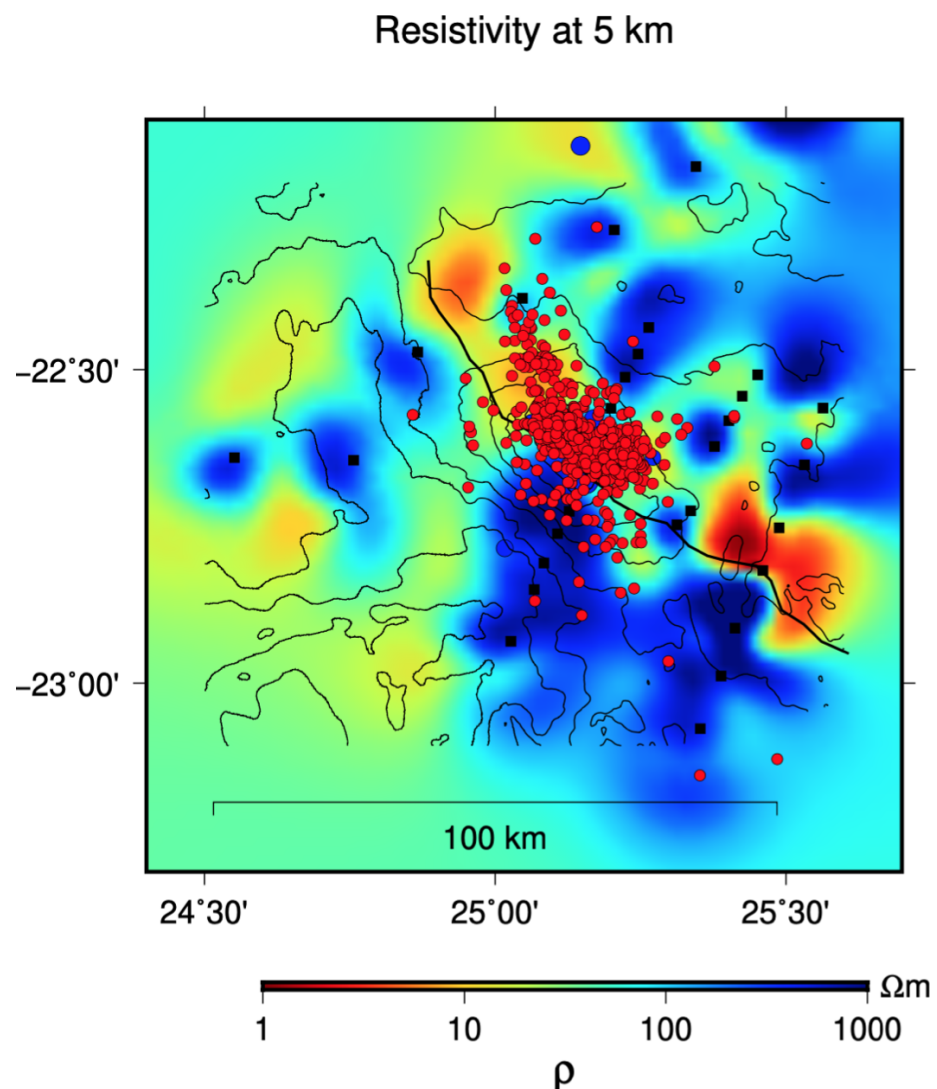


Figure A.4: Estimated fault trace with aftershock distributions, taken from Moorkmap et al., (2019) [1]

Appendix B

B.1 Configuration and Parameter Files (SeisSol)

B.1.1 Define a Fault Model - botswana_fault_700km_r6.yaml

```
!Switch
[ rs_a ]: !ConstantMap
  map:
    rs_a: 0.01
[ RS_s10 ]: !ConstantMap
  map:
    RS_s10: 0.1
[ rs_srW ]: !ConstantMap
  map:
    rs_srW: 0.1

[ s_xx , s_yy , s_zz , s_xy , s_yz , s_xz ]: !Include initial_0.95.yaml
[ nuc_xx , nuc_yy , nuc_zz , nuc_xy , nuc_yz , nuc_xz ]: !Include nucleation_0.37_1.06km.yaml
```

B.1.2 Setup Initial Stress - initial_0.95.yaml

```
!EvalModel
parameters: [Omega, eCS, b_xx, b_yy, b_zz, b_xy, b_yz, b_xz]
model: !Switch
  [Omega]: !FunctionMap
    map:
      Omega: |
        if (z>=-33000.) {
          return 1.0;
        } else {
          if (z>=-37000.) {
            a = 1.0-(z+37000.)/4000.;
            Sx = (3.0*a*a-2.0*a*a*a);
            return 1.0-Sx;
          } else {
            return 0.001;
          }
        }
      [b_xx, b_yy, b_zz, b_xy, b_yz, b_xz]: !EvalModel
      parameters: [sig_zz,S]
```

```

model: !FunctionMap
  map:
    sig_zz: |
      return 2670.0*(1.0-0.95)*9.8*min(-5000.0,z);
    S: |
      R = 0.7;
      return (1.0/R-1.0);
components: !AndersonianStress
constants:
  mu_d: 0.1
  mu_s: 0.6
  SH_max: 132.0
  cohesion: 0.0
  s2ratio: 0.5
  S_v: 1
[eCS]: !FunctionMap
  map:
    eCS: |
      return 2670.0*(1.0-0.95)*9.8*min(-5000.0,z);
components: !FunctionMap
  map:
    s_xx: return Omega*b_xx + (1.0-Omega)*eCS;
    s_yy: return Omega*b_yy + (1.0-Omega)*eCS;
    s_zz: return Omega*b_zz + (1.0-Omega)*eCS;
    s_xy: return Omega*b_xy;
    s_yz: return Omega*b_yz;
    s_xz: return Omega*b_xz;

```

B.1.3 Nucleate the Rupture - nucleation_0.37_1.06km.yaml

```

!EvalModel
parameters: [b_xx, b_yy, b_zz, b_xy, b_yz, b_xz, ShapeNucleation]
model: !Switch
  [b_xx, b_yy, b_zz, b_xy, b_yz, b_xz]: !EvalModel
    parameters: [S, sig_zz]
    model: !FunctionMap
      map:
        sig_zz: |
          return -2670.0*(1.0-0.37)*9.8*29000;
        S: |
          R = 4.0;
          return (1.0/R-1.0);
components: !AndersonianStress
constants:
  mu_d: 0.1
  mu_s: 0.6
  SH_max: 132.0
  cohesion: 0.0
  s2ratio: 0.5

```

Appendix B

```

S_v: 1
[ShapeNucleation]: !FunctionMap
  map:
    ShapeNucleation: |
      xc = -3446.35;
      yc= 5.21499;
      zc=-29000;
      r_crit = 1060.0;
      r = sqrt(pow(x-xc, 2.0) + pow(y-yc, 2.0) + pow(z-zc, 2.0));
      if (r < r_crit) {
        return exp(pow(r,2.0)/(pow(r,2.0)-pow(r_crit,2.0)));
      }
      return 0.0;
components: !FunctionMap
  map:
    nuc_xx: return ShapeNucleation*b_xx;
    nuc_yy: return ShapeNucleation*b_yy;
    nuc_zz: return ShapeNucleation*b_zz;
    nuc_xy: return ShapeNucleation*b_xy;
    nuc_yz: return ShapeNucleation*b_yz;
    nuc_xz: return ShapeNucleation*b_xz;

```

B.1.4 Include Material Properties - `botswana_material.yaml`

```

!Any
  components:
    - !ASAGI
      file: botswana_RhoMuLambda.nc
      parameters: [rho, mu, lambda]
      var: data
    - !ConstantMap
      map:
        rho: 330.
        mu: 65942325000.
        lambda: 81235350000.

```

In which `botswana_RhoMuLambda.nc`:

```

netcdf botswana_RhoMuLambda {
  types:
    compound material {
      float rho ;
      float mu ;
      float lambda ;
    };
  dimensions:
    x = 220 ;
    y = 218 ;

```

```

z = 20 ;
variables:
  float x(x) ;
  float y(y) ;
  float z(z) ;
  material data(z, y, x) ;
}

```

B.1.5 Parameter File in SeisSol - parameter_700km_r6.par

```

&equations
MaterialFileName = 'botswana_material.yaml'
Plasticity=0 ! Deactivate off-fault plasticity
/
&IniCondition
/
&Boundaries
BC_fs = 1 ! Activate free surface boundary conditions
BC_dr = 1 ! Activate dynamic rupture boundary conditions
BC_of = 1 ! Activate absorbing boundary conditions
/
&DynamicRupture
FL = 103 ! Choose RS friction Law with strong velocity weakening
ModelFileName = 'botswana_fault_700km_r6.yaml'

!Define the RS friction law parameters

RS_f0 = 0.6 ! Steady-state friction coefficient
RS_sr0 = 1d-6 ! Reference slip velocity
RS_b = 0.014 ! Evolution effect parameter
Mu_W=0.1 ! Weakening friction coefficient
RS_iniSlipRate1 = 1d-16 ! Initial Slip rate
t_0 = 0.4 ! Forced rupture decay time

GPwise=1 ! Initial condition projection on every points

! Reference point
XRef = 0.1
YRef = 0.1
ZRef = -1.0
refPointMethod = 1

RF_output_on = 0 ! Deactivate rupture front ascii output
magnitude_output_on = 1 ! Activate moment magnitude output
energy_rate_output_on = 1 ! Activate moment rate output

OutputPointType = 5 ! Type (0: no output, 3: ascii, 4: paraview, 5: 3+4)

SlipRateOutputType = 0

```

Appendix B

```
! 0: the difference between the velocity on both side of the fault (Smoothen)
! 1: the fault tractions & the failure criterion (Less smooth but usually more accurate)
/
&Elementwise
printIntervalCriterion = 2 ! 1=iteration, 2=time
printtimeinterval_sec = 0.5 ! Time interval at which output will be written

OutputMask = 1 1 1 1 1 1 1 1 1 0 1
! 1) SRs, SRd
! 2) T_s, T_d, P_n
! 3) u_n
! 4) Mud, StV
! 5) Ts0, Td0, Pn0
! 6) Sls and Sld
! 7) Vr
! 8) ASI
! 9) PSR
! 10) RT
! 11) DS
! 12) P_f, Tmp
! See Appendix C.2

refinement = 0
! 0): Each tetrahedron face has 1 triangle
! 1): Each tetrahedron face has 4 triangles (Subdivided once)
! 2): Each tetrahedron face has 16 triangles (Subdivided twice)
/
&Pickpoint
printtimeinterval = 0.5 ! Index of printed info at timesteps
OutputMask = 1 1 1 1 1 1 1 1 1 1 ! Turn on/off fault outputs
nOutpoints = 16
PPFileName = 'recevier16_35K.dat'
/
&SourceType
/
&SpongeLayer
/
&MeshNml
MeshFile = '../mesh/mesh_700km.puml.h5'
meshgenerator = 'PUML' ! Name of mesh generator
/
&Discretization
```

Appendix B

```
CFL = 0.5 ! CourantFriedrichsLewy condition (Less than 1)
FixTimeStep = 5 ! Choose maximum timestep of printed info
ClusteredLTS = 2
! 2,3,5: Local time stepping (Advised value 2)
! 1: Global time stepping (Slow)
/
&Output
OutputFile = './output_700km_r6/botswana_model_700kmr6'
Format = 6 ! 0) IDL; 1) TECPLLOT; 2) IBM DX; 4) GiD; 6) hdf5; 10) no output
iOutputMask = 0 0 0 0 0 1 1 1
printIntervalCriterion= 2
!Index of printed info criterion: 1) timesteps; 2) time; 3) timesteps+time
TimeInterval = 0.5 ! Index of printed info at time

nRecordPoints = 16 !Number of off-fault receivers
RFileName = 'recevier16_35K_seissol.dat'
pickdt = 0.01 ! Pickpoint Sampling rate
pickDtType = 1
ReceiverOutputInterval = 0.5
! (Optional) If omitted, receivers are written at the end of the simulation

!Free surface output
SurfaceOutput = 1 !Activate SurfaceOutput
SurfaceOutputInterval = 0.5 ! Index of printed info at time
/
&AbortCriteria
EndTime = 60.0 ! Define total simulation time
/
&Analysis
/
&Debugging
/
```

B.1.6 Run SeisSol with a Shell Script - seissol.sh

```
#!/bin/bash
ulimit -Ss unlimited
SeisSol_Release_drome_4_elastic parameters_700km_r6.par

nohup mpirun -n 16 ./seissol.sh & > output_700km_r6.log&
```

Appendix C

C.1 SeisSol Input Parameters for the Preferred Model

Table C.1: Full list of *SeisSol* parameters used in the preferred model

<i>SeisSol</i> name	Symbol	Value	Note
-	$d_{seismogenic}$	-33000.0	User defined depth of seismogenic zone
-	d_{max}	-37000.0	User defined maximum fault depth
-	d_{min}	-5000	User defined minimum fault depth
-	ρ_{crust}	2670.0	User defined overlaying rock density
-	g	9.8	User defined gravitational constant
-	R_{ini}	0.7	User defined initial relative prestress ratio
-	R_{nuc}	4	User defined nucleation relative prestress ratio
-	γ_{ini}	0.95	User defined initial pore fluid pressure
-	γ_{nuc}	0.37	User defined nucleation pore fluid pressure
-	x_c	-3446.35	User defined nucleation coordinate in x-axis
-	y_c	5.21499	User defined nucleation coordinate in y-axis
-	z_c	-29000.0	User defined nucleation coordinate in z-axis
-	r_c	1060.0	User defined nucleation radius
-	ρ	3330.0	User defined background rock density
-	λ	81235350000.0	User defined Lamé's first parameter
-	μ	65942325000.0	User defined Lamé's second parameter
mu_d	μ_d	0.1	Andersonian Stress input parameter
mu_s	μ_s	0.6	Andersonian Stress input parameter
SH_max	SH_{max}	132.0	Andersonian Stress input parameter
S_v	S_v	1	Andersonian Stress input parameter
cohesion	-	0.0	Andersonian Stress input parameter
s2ratio	ν	0.5	Andersonian Stress input parameter
rs_a	$a(x)$	0.01	Rate-and-State friction law input parameter
RS_b	b	0.014	Rate-and-State friction law input parameter
RS_sr0	V_0	10^{-6}	Rate-and-State friction law input parameter
RS_sl0	L	0.1	Rate-and-State friction law input parameter
RS_srW	$V_W(x)$	0.1	Rate-and-State friction law input parameter
RS_f0	f_0	0.6	Rate-and-State friction law input parameter
Mu_W	f_W	0.1	Rate-and-State friction law input parameter
RS_iniSlipRate1	V_{ini}	10^{-16}	Rate-and-State friction law input parameter
t_0	t_0	0.4	Rate-and-State friction law
CFL	-	0.5	Convergence condition
EndTime	t_{total}	40.0	Simulation stop criterion

C.2 SeisSol Full Fault Output

<i>SeisSol</i> name	Physical meaning	Note
SRs	Slip rates in strike direction	
SRd	Slip rates in dip direction	
T_s	Transient shear stress in strike direction	
T_d	Transient shear stress in dip direction	
P_n	Transient normal stress	
u_n	Normal velocity	
Mud	Current friction	
StV	state variable	In case of RS friction
Ts0	Initial shear stress in strike direction	
Td0	Initial shear stress in dip direction	
Pn0	Initial normal stress	
Sls	slip in strike direction	
Sld	slip in dip direction	
Vr	Rupture velocity	Spatial derivatives of the rupture time
ASI	Absolute slip	
PSR	Peak slip rate	
RT	rupture time	
DS	Critical distance	In case of LSW friction
P_f	Pore pressure	
Tmp	Temperature	

C.3 Raw Synthetic Seismograms for All 16 Stations

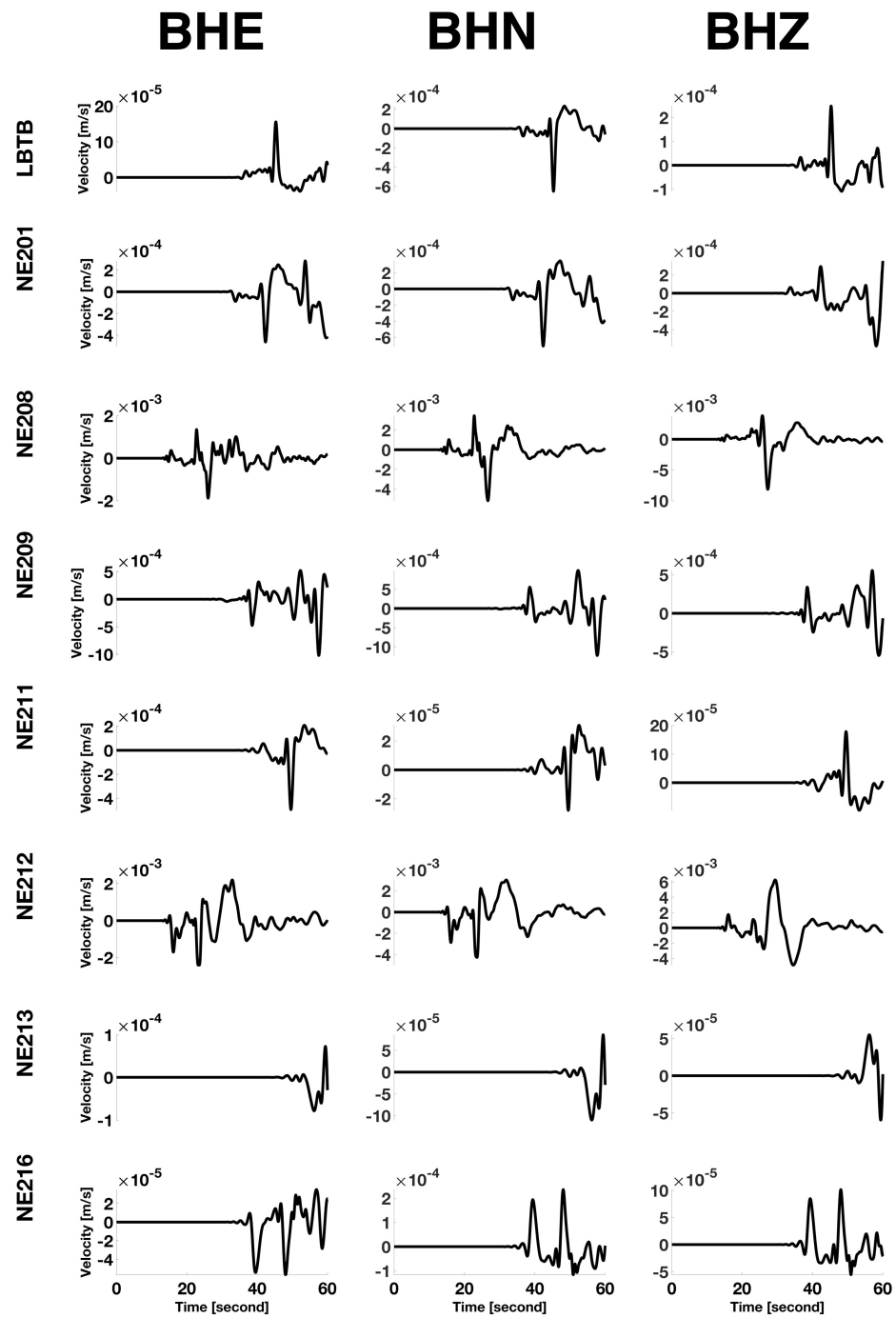


Figure C.1: Synthetic seismogram, no filter applied, total simulation time of 60 s

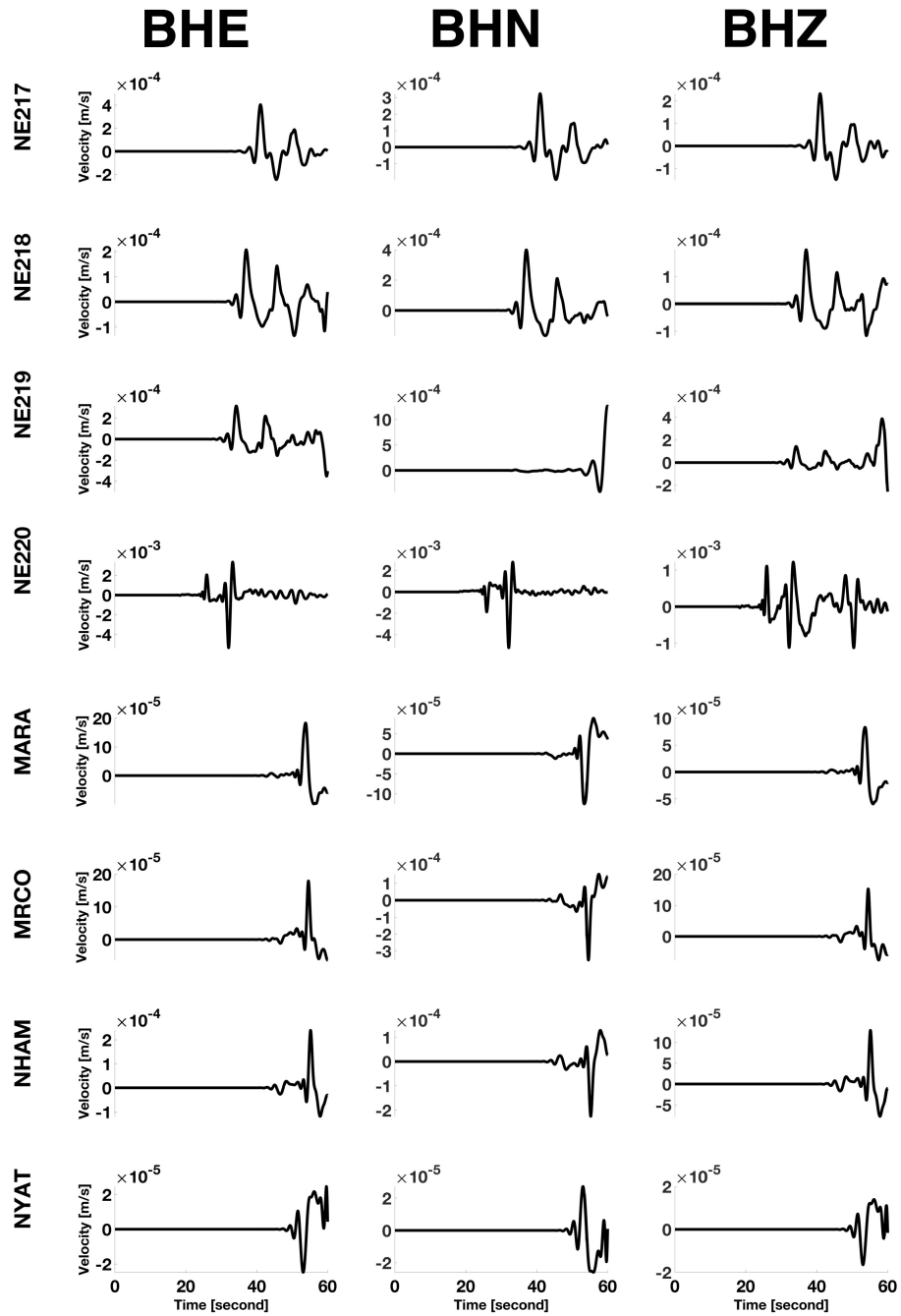


Figure C.2: Synthetic seismogram, no filter applied, total simulation time of 60 s

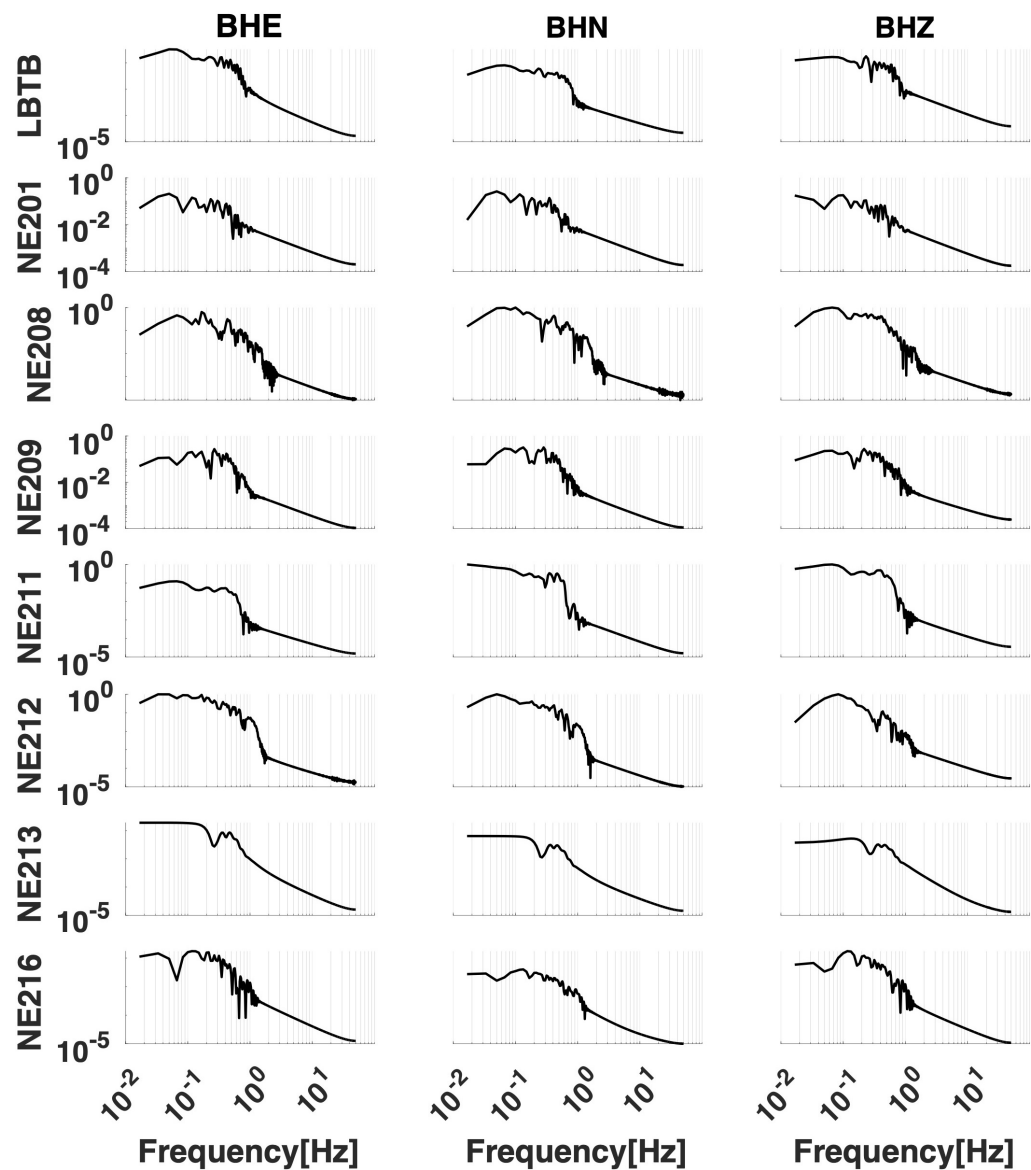


Figure C.3: Spectrum for the synthetic waveform data

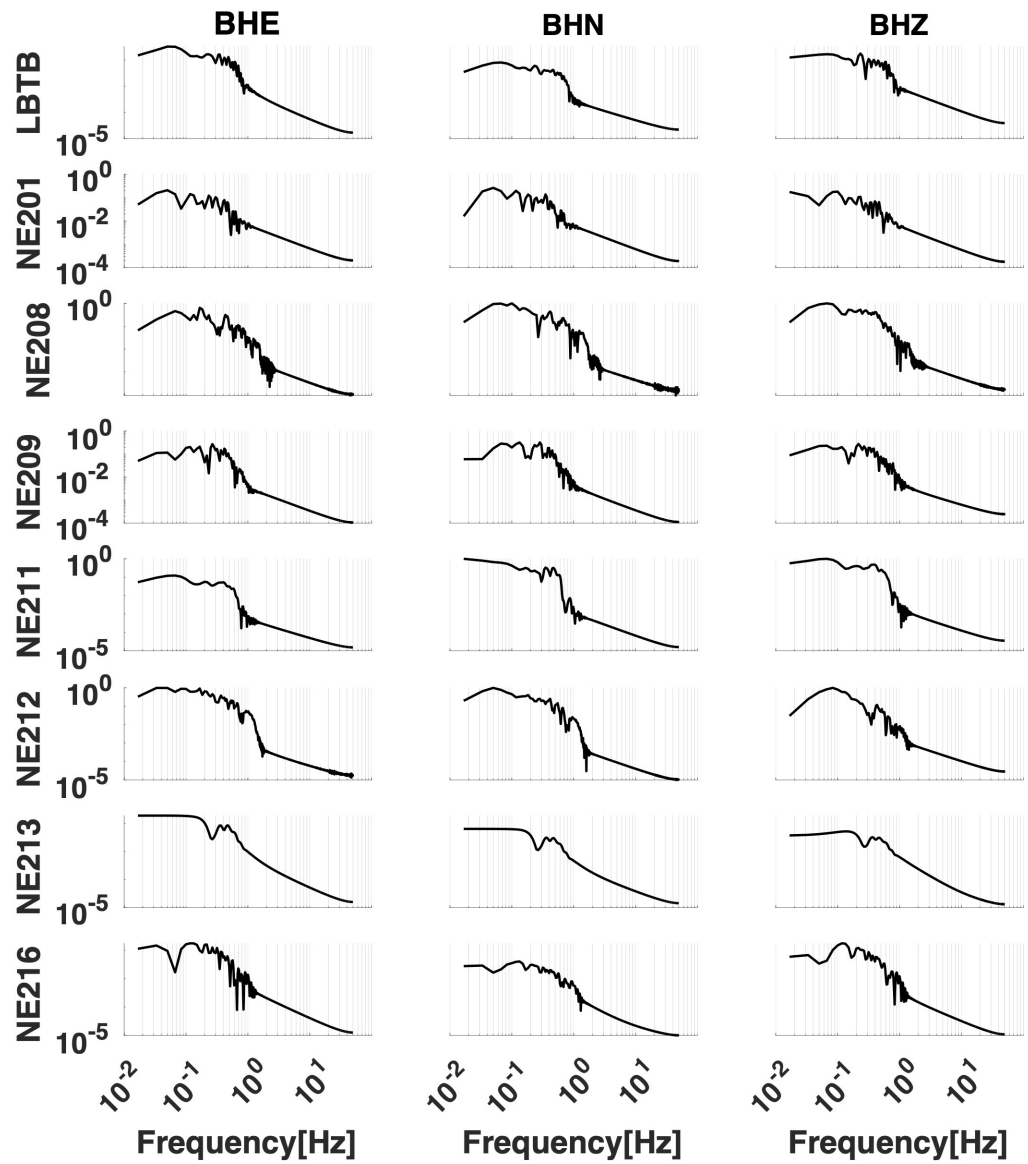


Figure C.4: Spectrum for the synthetic waveform data

Appendix D

D.1 Kinematic Model from Materna et al. (2019)

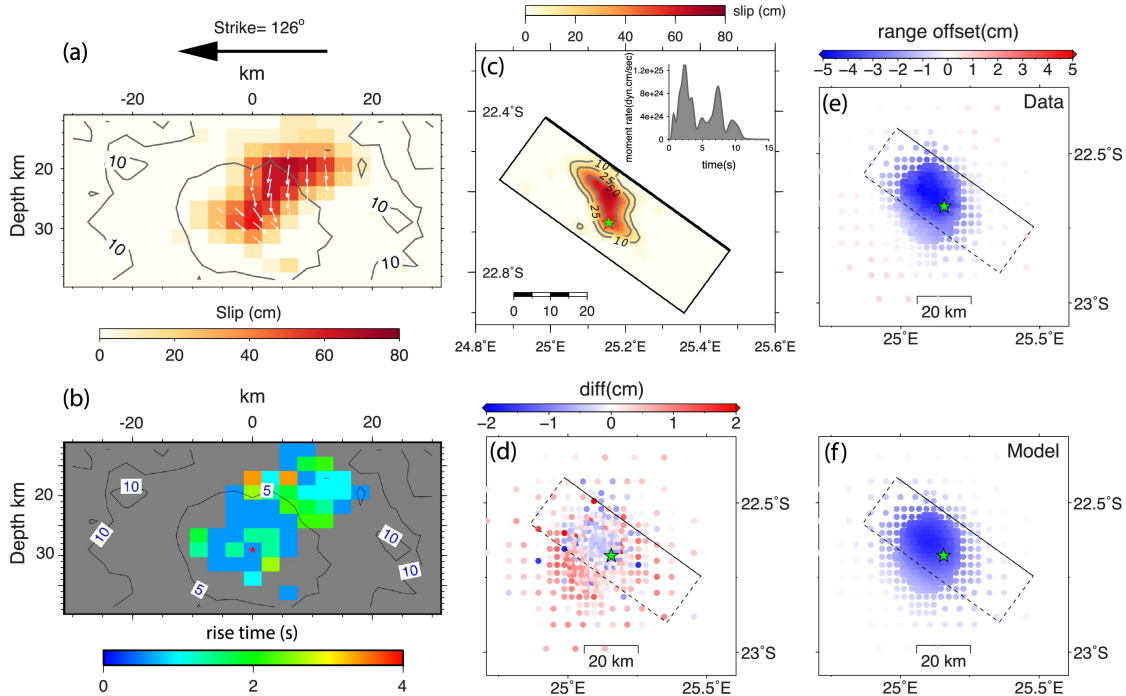


Figure D.1: Kinematic model of the 2017 Botswana earthquake, taken from Materna et al. (2019) [13]

Nomenclature

Abbreviations	Interpretation	Note
IPEs	Intraplate Earthquakes	Unified model
LSCs	Local Stress Concentrators	Unified model
SCR	Stable Continental Region	
EARS	East Africa rift system	
ORZ	Okavango Rift Zone	
MT	Magnetotellurics	
ADER-DG	Arbitrary high-order DERivative-Discontinuous Galerkin	
DR	Dynamic Rupture	
MPI	Message Passing Interface standard	
HPC	High Performance Computing	
eCS	Effective Compressive Stress	
UTC	Coordinated Universal Time	
UTM	Universal Transverse Mercator	
USGS	United States Geological Survey	
FDSN	International Federation of Digital Seismography Networks	
InSAR	Interferometric synthetic aperture radar	
GCMT	Global Centroid Moment Tensor	

Appendix D

Symbols	Physical meaning	Note
SH_{max}	Azimuth of maximum compressive horizontal stress	Static analysis
ν	Stress shape ratio	Static analysis
R	Relative prestress ratio	Static analysis
γ	Pore fluid prestress	Static analysis
μ_d	Dynamic friction coefficient	Friction law parameter
μ_s	Static friction coefficient	Friction law parameter
D_c	Critical distance	Friction law parameter
a	Direct effect parameter	Friction law parameter
b	Evolution effect parameter	Friction law parameter
V_0	Reference slip velocity	Friction law parameter
L	Characteristic slip scale	Friction law parameter
V_W	Weakening slip velocity	Friction law parameter
f_0	Steady-state friction coefficient	Friction law parameter
f_W	Weakening friction coefficient	Friction law parameter
V_{ini}	Initial sliding velocity	Friction law parameter
t_0	Forced rupture decay time	Friction law parameter

Bibliography

- [1] Max Moorkamp, Stewart Fishwick, Richard J Walker, and Alan G Jones. *Geophysical evidence for crustal and mantle weak zones controlling intra-plate seismicity—the 2017 Botswana earthquake sequence*. *Earth and Planetary Science Letters*, 506:175–183, 2019.
- [2] Thomas Obermaier. *Mechanisms of intraplate earthquakes: The 2017 Botswana event*. *BS Thesis at LMU München*, October 2020.
- [3] Sophia Gahr. *The 2017 Intraplate Earthquake in Botswana: Computational Modeling of the Rupture Dynamics*. *BS Thesis at LMU München*, May 2021.
- [4] Gardonio B., Jolivet R., Calais E., and Leclère H. *The April 2017 Mw 6.5 Botswana Earthquake: An Intraplate Event Triggered by Deep Fluids*. *Geophysical Research Letters*, 45:8886–8896, 2018. doi: 10.1029/2018GL078297.
- [5] Gregory Smits. *Conduits of power: What the origins of Japan’s earthquake catfish reveal about religious geography*. *Japan Review*, pages 41–65, 2012.
- [6] Spyros Missiakoulis. *Aristotle and earthquake data: A historical note*. *International Statistical Review*, 76(1):130–133, 2008.
- [7] Hong-Sen Yan and Kuo-Hung Hsiao. *Reconstruction design of the lost seismoscope of ancient China*. *Mechanism and Machine Theory*, 42(12):1601–1617, 2007.
- [8] Edward Paice. *Wrath of God: The great Lisbon earthquake of 1755*. Quercus Books, 2008.
- [9] James Dewey and Perry Byerly. *The early history of seismometry (to 1900)*. *Bulletin of the Seismological Society of America*, 59(1):183–227, 1969.
- [10] Arch C Johnston and Lisa R Kanter. *Earthquakes in stable continental crust*. *Scientific American*, 262(3):68–75, 1990.
- [11] Pradeep Talwani. *Intraplate earthquakes*. 2014.
- [12] Pradeep Talwani. *On the nature of intraplate earthquakes*. *Journal of Seismology*, 21(1):47–68, 2017.
- [13] Kathryn Materna, Shengji Wei, Xin Wang, Luo Heng, Teng Wang, Weiwen Chen, Rino Salman, and Roland Bürgmann. *Source characteristics of the 2017 Mw 6.4 Mojabana, Botswana earthquake, a rare lower-crustal event within an ancient zone of weakness*. *Earth and Planetary Science Letters*, 506:348–359, 2019.
- [14] Susan E Hough, John G Armbruster, Leonardo Seeber, and Jerry F Hough. *On the modified Mercalli intensities and magnitudes of the 1811–1812 New Madrid earthquakes*. *Journal of Geophysical Research: Solid Earth*, 105(B10):23839–23864, 2000.

Bibliography

- [15] Frank Krüger and Frank Scherbaum. *The 29 September 1969, Ceres, South Africa, earthquake: Full waveform moment tensor inversion for point source and kinematic source parameters.* *Bulletin of the Seismological Society of America*, 104(1):576–581, 2014.
- [16] JR Bowman. *The 1988 Tennant Creek, northern territory, earthquakes: A synthesis.* *Australian Journal of Earth Sciences*, 39(5):651–669, 1992.
- [17] Lanbo Liu and Mark D Zoback. *Lithospheric strength and intraplate seismicity in the New Madrid seismic zone.* *Tectonics*, 16(4):585–595, 1997.
- [18] Fred F Pollitz, Louise Kellogg, and Roland Burgmann. *Sinking mafic body in a reactivated lower crust: A mechanism for stress concentration at the New Madrid seismic zone.* *Bulletin of the Seismological Society of America*, 91(6):1882–1897, 2001.
- [19] Eric Calais, Thierry Camelbeeck, Seth Stein, Mian Liu, and TJ Craig. *A new paradigm for large earthquakes in stable continental plate interiors.* *Geophysical Research Letters*, 43(20):10–621, 2016.
- [20] Lynn R Sykes and Marc L Sbar. *Intraplate earthquakes, lithospheric stresses and the driving mechanism of plate tectonics.* *Nature*, 245(5424):298–302, 1973.
- [21] Lynn R Sykes. *Intraplate seismicity, reactivation of preexisting zones of weakness, alkaline magmatism, and other tectonism postdating continental fragmentation.* *Reviews of Geophysics*, 16(4):621–688, 1978.
- [22] GC Beroza and H Kanamori. *Earthquake seismology: an introduction and overview.* 2015.
- [23] Folarin Kolawole, Estella A Atekwana, Sean Malloy, D Sarah Stamps, Raphael Grandin, Mohamed G Abdelsalam, Khumo Leseane, and Elisha M Shemang. *Aeromagnetic, gravity, and Differential Interferometric Synthetic Aperture Radar analyses reveal the causative fault of the 3 April 2017 Mw 6.5 Moiyabana, Botswana, earthquake.* *Geophysical Research Letters*, 44(17):8837–8846, 2017.
- [24] Albano M., Polcari M., Bignami C., Moro M., Saroli M., and Stramondo S. *Did Anthropogenic Activities Trigger the 3 April 2017 Mw 6.5 Botswana Earthquake? .* *Remote Sensing*, 9(10), October 2017. doi: 10.3390/rs9101028.
- [25] Thifhelimbilu Mulabisana, Mustapha Meghraoui, Vunganai Midzi, Mohamed Saleh, Onkgopotse Ntibinyane, T Kwadiba, Brassnavy Manzunzu, Oarabile Seiphemo, Tebogo Pule, and Ian Saunders. *Seismotectonic analysis of the 2017 Moiyabana earthquake (MW 6.5; Botswana), insights from field investigations, aftershock and InSAR studies.* *Journal of African Earth Sciences*, 182:104297, 2021.
- [26] Oliver Heidbach, Mojtaba Rajabi, Karsten Reiter, Moritz Ziegler, Wsm Team, et al. *World stress map database release 2016.* *GFZ Data Services*, 10, 2016.
- [27] M Pagani, J Garcia-Pelaez, R Gee, K Johnson, V Poggi, R Styron, G Weatherill, M Simionato, D Viganò, L Danciu, et al. *Global Earthquake Model (GEM) seismic hazard map (version 2018.1–December 2018).* *GEM Foundation: Pavia, Italy*, 2018.
- [28] Baraka D Kinabo, Estella A Atekwana, John Patrick Hogan, Motsoptse P Modisi, Daniel D Wheaton, and AB Kampunzu. *Early structural development of the Okavango rift zone, NW Botswana.* *Journal of African Earth Sciences*, 48(2-3):125–136, 2007.

Bibliography

- [29] D Sarah Stamps, Eric Calais, Elifuraha Saria, Chris Hartnady, Jean-Mathieu Nocquet, Cynthia J Ebinger, and Rui M Fernandes. *A kinematic model for the East African Rift*. *Geophysical Research Letters*, 35(5), 2008.
- [30] Oliver Heidbach, Mark Tingay, Andreas Barth, John Reinecker, Daniel Kurfeß, and Birgit Müller. *Global crustal stress pattern based on the World Stress Map database release 2008*. *Tectonophysics*, 482(1-4):3–15, 2010.
- [31] Youqiang Yu, Kelly H Liu, Zhouchuan Huang, Dapeng Zhao, Cory A Reed, Moikwathai Moidaki, Jianshe Lei, and Stephen S Gao. *Mantle structure beneath the incipient Okavango rift zone in southern Africa*. *Geosphere*, 13(1):102–111, 2017.
- [32] CV Reeves. *Rifting in the Kalahari?* *Nature*, 237(5350):95–96, 1972.
- [33] NM Beeler, TE Tullis, and DL Goldsby. *Constitutive relationships and physical basis of fault strength due to flash heating*. *Journal of Geophysical Research: Solid Earth*, 113(B1), 2008.
- [34] Maarten J De Wit, Cornel EJ de Ronde, Marian Tredoux, Chris Roering, Rodger J Hart, Richard A Armstrong, Rod WE Green, Ellie Peberdy, and Roger A Hart. *Formation of an Archaean continent*. *Nature*, 357(6379):553–562, 1992.
- [35] RBM Mapeo, RA Armstrong, and AB Kampunzu. *SHRIMP U-Pb zircon geochronology of gneisses from the Gweta borehole, northeast Botswana: implications for the Palaeoproterozoic Magondi Belt in southern Africa*. *Geological Magazine*, 138(3):299–308, 2001.
- [36] Islam Fadel, Hanneke Paulsen, Mark van der Meijde, Motsamai Kwadiba, Onkgopotse Ntibinyane, Andrew Nyblade, and Raymond Durheim. *Crustal and upper mantle shear wave velocity structure of Botswana: The 3 April 2017 central Botswana earthquake linked to the East African Rift System*. *Geophysical research letters*, 47(4):e2019GL085598, 2020.
- [37] Chikondi Chisenga, Mark Van der Meijde, Jianguo Yan, Islam Fadel, Estella A Atekwana, Rebekka Steffen, and Calistus Ramotoroko. *Gravity derived crustal thickness model of Botswana: Its implication for the Mw 6.5 April 3, 2017, Botswana earthquake*. *Tectonophysics*, 787:228479, 2020.
- [38] Marlon Ramos, Prithvi Thakur, Yihe Huang, Ruth Harris, and Kenneth Ryan. *Working with Dynamic Earthquake Rupture Models: A Practical Guide*. 03 2022. doi: 10.31223/X5KD16.
- [39] Martin Käser and Michael Dumbser. *An arbitrary high-order discontinuous Galerkin method for elastic waves on unstructured meshes—I. The two-dimensional isotropic case with external source terms*. *Geophysical Journal International*, 166(2):855–877, 2006.
- [40] Heiner Igel. *Computational seismology: a practical introduction*. Oxford University Press, 2017.
- [41] Heiner Igel and Michael Weber. *SH-wave propagation in the whole mantle using high-order finite differences*. *Geophysical research letters*, 22(6):731–734, 1995.
- [42] Heiner Igel and Michael Weber. *P-SV wave propagation in the Earth’s mantle using finite differences: Application to heterogeneous lowermost mantle structure*. *Geophysical Research Letters*, 23(5):415–418, 1996.

Bibliography

- [43] Eric M Dunham, David Belanger, Lin Cong, and Jeremy E Kozdon. *Earthquake ruptures with strongly rate-weakening friction and off-fault plasticity, part 2: Nonplanar faults*. *Bulletin of the Seismological Society of America*, 101(5):2308–2322, 2011.
- [44] Zheqiang Shi and Steven M Day. *Rupture dynamics and ground motion from 3-D rough-fault simulations*. *Journal of Geophysical Research: Solid Earth*, 118(3):1122–1141, 2013.
- [45] Carsten Uphoff and Michael Bader. *Generating high performance matrix kernels for earthquake simulations with viscoelastic attenuation*. In *2016 International Conference on High Performance Computing and Simulation (HPCS)*, pages 908–916. IEEE, 2016.
- [46] Stephanie Wollherr, Alice-Agnes Gabriel, and Carsten Uphoff. *Off-fault plasticity in three-dimensional dynamic rupture simulations using a modal Discontinuous Galerkin method on unstructured meshes: implementation, verification and application*. *Geophysical Journal International*, 214(3):1556–1584, 2018.
- [47] Stephanie Wollherr, Alice-Agnes Gabriel, and P Martin Mai. *Landers 1992 “reloaded”: Integrative dynamic earthquake rupture modeling*. *Journal of Geophysical Research: Solid Earth*, 124(7):6666–6702, 2019.
- [48] Thomas Ulrich, Alice-Agnes Gabriel, Jean-Paul Ampuero, and Wenbin Xu. *Dynamic viability of the 2016 Mw 7.8 Kaikōura earthquake cascade on weak crustal faults*. *Nature communications*, 10(1):1–16, 2019.
- [49] Thomas Ulrich, Stefan Vater, Elizabeth H Madden, Jörn Behrens, Ylona van Dinther, Iris Van Zelst, Eric J Fielding, Cunren Liang, and Alice-Agnes Gabriel. *Coupled, physics-based modeling reveals earthquake displacements are critical to the 2018 Palu, Sulawesi tsunami*. *Pure and Applied Geophysics*, 176(10):4069–4109, 2019.
- [50] Michael Dumbser, Martin Käser, and Eleuterio F Toro. *An arbitrary high-order Discontinuous Galerkin method for elastic waves on unstructured meshes-V. Local time stepping and p-adaptivity*. *Geophysical Journal International*, 171(2):695–717, 2007.
- [51] Alexander Breuer, Alexander Heinecke, Sebastian Rettenberger, Michael Bader, Alice-Agnes Gabriel, and Christian Pelties. *Sustained petascale performance of seismic simulations with SeisSol on SuperMUC*.
- [52] Ruth A Harris, Michael Barall, Brad Aagaard, Shuo Ma, Daniel Roten, Kim Olsen, Benchun Duan, Dunyu Liu, Bin Luo, Kangchen Bai, et al. *A suite of exercises for verifying dynamic earthquake rupture codes*. *Seismological Research Letters*, 89(3):1146–1162, 2018.
- [53] Brittany A Erickson, Junle Jiang, Michael Barall, Nadia Lapusta, Eric M Dunham, Ruth Harris, Lauren S Abrahams, Kali L Allison, Jean-Paul Ampuero, Sylvain Barbot, et al. *The community code verification exercise for simulating sequences of earthquakes and aseismic slip (SEAS)*. *Seismological Research Letters*, 91(2A):874–890, 2020.
- [54] Seth Stein and Michael Wysession. *An introduction to seismology, earthquakes, and earth structure*. John Wiley & Sons, 2009.
- [55] Marlon D Ramos, Prithvi Thakur, Yihe Huang, Ruth A Harris, and Kenny J Ryan. *Working with Dynamic Earthquake Rupture Models: A Practical Guide*. *Seismological Research Letters*, 2022.

Bibliography

- [56] Alice-Agnes Gabriel, J-P Ampuero, Luis A Dalguer, and Paul Martin Mai. *The transition of dynamic rupture styles in elastic media under velocity-weakening friction*. *Journal of Geophysical Research: Solid Earth*, 117(B9), 2012.
- [57] Thomas H Heaton. *Evidence for and implications of self-healing pulses of slip in earthquake rupture*. *Physics of the Earth and Planetary Interiors*, 64(1):1–20, 1990.
- [58] Alain Cochard and Raúl Madariaga. *Dynamic faulting under rate-dependent friction*. *pure and applied geophysics*, 142(3):419–445, 1994.
- [59] J-P Ampuero and Y Ben-Zion. *Cracks, pulses and macroscopic asymmetry of dynamic rupture on a bimaterial interface with velocity-weakening friction*. *Geophysical Journal International*, 173(2):674–692, 2008.
- [60] Kadek Hendrawan Palgunadi, Alice-Agnes Gabriel, Thomas Ulrich, José Ángel López-Comino, and Paul Martin Mai. *Dynamic Fault Interaction during a Fluid-Injection-Induced Earthquake: The 2017 Mw 5.5 Pohang Event*. *Bulletin of the Seismological Society of America*, 110(5):2328–2349, 2020.
- [61] Jeremy E Kozdon and Eric M Dunham. *Rupture to the Trench: Dynamic Rupture Simulations of the 11 March 2011 Tohoku Earthquake Rupture to the Trench: Dynamic Rupture Simulations of the 11 March 2011 Tohoku Earthquake*. *Bulletin of the Seismological Society of America*, 103(2B):1275–1289, 2013.
- [62] James Byerlee. *Friction of rocks*. In *Rock friction and earthquake prediction*, pages 615–626. Springer, 1978.
- [63] Elizabeth H Madden, Thomas Ulrich, and Alice-Agnes Gabriel. *The State of Pore Fluid Pressure and 3-D Megathrust Earthquake Dynamics*. *Journal of Geophysical Research: Solid Earth*, 127(4):e2021JB023382, 2022.
- [64] Hiroo Kanamori. *The nature of seismicity patterns before large earthquakes*. 1981.
- [65] Susan LM Miller and Robert R Stewart. *The relationship between elastic-wave velocities and density in sedimentary rocks: A proposal*. *Crewes Res. Rep.*, pages 260–273, 1991.
- [66] Islam Fadel, Mark van der Meijde, and Hanneke Paulssen. *Crustal structure and dynamics of Botswana*. *Journal of Geophysical Research: Solid Earth*, 123(12):10–659, 2018.
- [67] Christophe Geuzaine and Jean-François Remacle. *Gmsh: A 3-D finite element mesh generator with built-in pre-and post-processing facilities*. *International journal for numerical methods in engineering*, 79(11):1309–1331, 2009.
- [68] Dimitri Komatitsch and Jeroen Tromp. *A perfectly matched layer absorbing boundary condition for the second-order seismic wave equation*. *Geophysical Journal International*, 154(1):146–153, 2003.
- [69] Alice-Agnes Gabriel, J-P Ampuero, LA Dalguer, and Paul Martin Mai. *Source properties of dynamic rupture pulses with off-fault plasticity*. *Journal of Geophysical Research: Solid Earth*, 118(8):4117–4126, 2013.
- [70] Jinhai Zhang, Jinlai Hao, Xu Zhao, Shuqin Wang, Lianfeng Zhao, Weimin Wang, and Zhenxing Yao. *Restoration of clipped seismic waveforms using projection onto convex sets method*. *Scientific reports*, 6(1):1–10, 2016.

Bibliography

- [71] Stephen Hawking. *A brief history of time: from big bang to black holes*. Random House, 2009.
- [72] Hiroo Kanamori and Don L Anderson. *Theoretical basis of some empirical relations in seismology*. *Bulletin of the seismological society of America*, 65(5):1073–1095, 1975.
- [73] TK Nguuri, J Gore, DE James, SJ Webb, C Wright, TG Zengeni, O Gwava, JA Snode, and Kaapvaal Seismic Group. *Crustal structure beneath southern Africa and its implications for the formation and evolution of the Kaapvaal and Zimbabwe cratons*. *Geophysical Research Letters*, 28(13):2501–2504, 2001.
- [74] Getachew E Tedla, M Van Der Meijde, AA Nyblade, and FD Van der Meer. *A crustal thickness map of Africa derived from a global gravity field model using Euler deconvolution*. *Geophysical Journal International*, 187(1):1–9, 2011.
- [75] Moho Youssof, H Thybo, IM Artemieva, and A Levander. *Moho depth and crustal composition in Southern Africa*. *Tectonophysics*, 609:267–287, 2013.
- [76] Robert J Geller. *Seismology: Japan must admit it can't predict quakes*. *Nature*, 545(7654):289–289, 2017.
- [77] Pascal Audet and Roland Bürgmann. *Dominant role of tectonic inheritance in supercontinent cycles*. *Nature geoscience*, 4(3):184–187, 2011.
- [78] Adrian Lenardic, L Moresi, and H Mühlhaus. *The role of mobile belts for the longevity of deep cratonic lithosphere: the crumple zone model*. *Geophysical Research Letters*, 27(8):1235–1238, 2000.
- [79] Martin Vallée, Jean Charléty, Ana MG Ferreira, Bertrand Delouis, and Julien Vergoz. *SCARDEC: a new technique for the rapid determination of seismic moment magnitude, focal mechanism and source time functions for large earthquakes using body-wave deconvolution*. *Geophysical Journal International*, 184(1):338–358, 2011.
- [80] Elisa Tinti, Emanuele Casarotti, Thomas Ulrich, Taufiq Taufiqurrahman, Duo Li, and Alice-Agnes Gabriel. *Constraining families of dynamic models using geological, geodetic and strong ground motion data: The Mw 6.5, October 30th, 2016, Norcia earthquake, Italy*. *Earth and Planetary Science Letters*, 576:117237, 2021.

List of Figures

1.1	Tectonic setting of southern Africa, taken from in Materna et al. (2019) [13].	6
1.2	(a) Schematic geologic map of Archean terranes in Botswana, (b) Aeromagnetic data over Botswana showing the placement of Karoo dykes, taken from Materna et al., (2019) [13].	7
2.1	A 3D mesh of our proposed model plotted together with the locations of 16 seismic stations (yellow sphere) from the NR (FDSN code) network and two proposed faults, F129 dips to northeast (blue plane) and F126 dips to southwest (red plane)	13
2.2	A 3D reconstruction of our proposed fault planes plotted together with the locations of the measured aftershocks (green dots) and the hypocenter (red sphere).	14
2.3	Slip-weakening friction law with $D_c = 2.7\text{ m}$, $\mu_s = 0.6$ and $\mu_d = 0.1$	15
2.4	Velocity-weakening friction law, taken from Ramos et al., 2022 [55], Velocity weakening friction law	16
3.1	Mesh4 visualization in Paraview, only contain fault F129, consists of 1,291,885 tetrahedron elements, red sphere represents hypocenter	24
3.2	Mesh3 visualization in Paraview, contain both fault F126 and F129, consists of 676,984 tetrahedron elements, red sphere represents hypocenter	25
3.3	Dynamic rupture fault output of Model-3.ref, we show the absolute slip on the reconstructed second fault plane, F126	26
3.4	A zoomed view of Figure 3.3 in the nucleation area, a green ruler measures the indicated line distance of the ruptured zone is about 1042 m	27
3.5	Dynamic rupture fault output of the Model-5.14, we show the absolute slip on the reconstructed first fault plane, F129	28
3.6	Dynamic rupture fault output of the Model-5.ref.hydro, we show the absolute slip on the reconstructed first fault plane, F129	29
3.7	Mesh700km visualization in Paraview, consists of 2,124,064 unstructured tetrahedron grids, red sphere represents hypocenter	30
3.8	Dynamic rupture fault output of the Model-700km.r6, we show the absolute slip on the reconstructed fault plane	31
3.12	Absolute slip of Model-700km.r6 from 0 to 5.5 seconds on reconstructed fault planes	33
3.16	Absolute slip rate of Model-700km.r6 from 0 to 5.5 seconds on reconstructed fault planes	34
3.17	Vertical displacement plotted from free surface output of our preferred model, Model-700km.r6	35
3.18	Vertical displacement comparison of the InSAR measurements and the free surface output (at 10 s) plotted from our preferred dynamic rupture model, <i>Model – 700km.r6</i> . Figure 3.18 (b) taken from Materna et al. (2019) [13]	36
3.19	Location of the corresponding seismic stations projected on <i>Mesh700km</i> , yellow sphere represents the seismic station used in this study	37

List of Figures

3.20	Normalized waveforms of the synthetic (black) and the observational (red) data of the 7 selected seismic stations, a 4th-order Butterworth filter [0.2, 0.6] Hz is applied to the data. The number on right upper corner is a normalization factor, which means the maximum synthetic magnitude divided by the maximum observational magnitude	39
3.21	Spectrum of the synthetic (black) and the observational (red) data of the 7 selected stations	40
3.22	Python code to request, process and save the seismic data using <i>Obspy</i>	41
3.23	NE217, removed the instrument response, applied a 4th-order Butterworth band-pass filter with the cutoff frequencies of [0.2, 1.5] Hz	42
3.24	NE208, raw data	43
4.1	Absolute slip (ASI) of Model-5_14 on reconstructed fault F129	47
4.2	Absolute slip (ASI) of Model-5_ref_hydro on reconstructed fault F129	47
4.3	Peak slip rate (PSR) of Model-5_14	48
4.4	Peak slip rate (PSR) of Model-5_ref_hydro	48
4.5	Slip in strike direction (Sls) of Model-5_14	49
4.6	Slip in strike direction (Sls) of Model-5_ref_hydro	49
4.7	Current friction coefficient (Mud) of Model-5_14	50
4.8	Current friction coefficient (Mud) of Model-5_ref_hydro	50
4.9	Rupture time (RT) of Model-5_14	51
4.10	Rupture time (RT) of Model-5_ref_hydro	51
4.11	Initial total shear stress of Model-5_14	52
4.12	Initial total shear stress of Model-5_ref_hydro	52
4.13	Total shear stress at 10 seconds of Model-5_14	53
4.14	Total shear stress at 10 seconds of Model-5_ref_hydro	53
4.15	Slip Rate in dip direction (SRd) at 10 seconds of Model-5_14	54
4.16	Slip Rate in dip direction (SRd) at 10 seconds of Model-5_ref_hydro	54
4.17	Filtered synthetic (black) and observed (red) waveforms of Station NE208 and NE212 for Model-5_14, a 4th-order Butterworth filter [0.2, 0.6] Hz is applied to the data. The number on right upper corner is a normalization factor, same as before	55
4.18	Filtered synthetic (black) and observed (red) waveforms of Station NE208 and NE212 for Model-5_ref_hydro, a 4th-order Butterworth filter [0.2, 0.6] Hz is applied to the data. The number on right upper corner is a normalization factor, same as before	55
4.19	Free surface output (at 6 s) for Model-5_14 and Model-5_ref_hydro	56
4.20	The 3D velocity model domain and seismic stations used for the inversion, figure taken from Fadel et al. (2020) [36]	57
A.1	A screenshot of CMT Web Page on the 2017 Botswana event, red circles the relevant parameters for our DR simulations	63
A.2	A screenshot of the webpage of the USGS W-phase Moment tensor solution and focal mechanism (beach ball), red circles emphasis the relevant parameters for our DR simulations	64
A.3	3D resistivity model, taken from Moorkmap et al., (2019) [1]	65
A.4	Estimated fault trace with aftershock distributions, taken from Moorkmap et al., (2019) [1]	66
C.1	Synthetic seismogram, no filter applied, total simulation time of 60 s	75
C.2	Synthetic seismogram, no filter applied, total simulation time of 60 s	76

List of Figures

C.3	Spectrum for the synthetic waveform data	77
C.4	Spectrum for the synthetic waveform data	78
D.1	Kinematic model of the 2017 Botswana earthquake, taken from Materna et al. (2019) [13]	79

List of Tables

1.1	proposed fault geometry by various research group	5
2.1	Parameters of fault geometry	12
2.2	<i>SeisSol</i> Friction Parameters for Rate-and-Sate Friction Law (FL=103)	17
2.3	<i>AndersonianStress</i> Input Parameters	19
3.1	SeisSol Simulation Results	23
3.2	Seismic stations	37
3.3	Summary for All Seismic Stations inside Our Model Domain	44
4.1	Full List of <i>SeisSol</i> Parameters used in Model-5_14 and Model-5_ref_hydro	46
4.2	Comparison Summary for Model-5_14 and Model-5_ref_hydro	55
C.1	Full list of <i>SeisSol</i> parameters used in the preferred model	73

Declaration of Competing Interest

The author declare that this study is completely objective, and he has no known competing financial interests or personal relations that could have appeared to influence the work reported in this thesis.

Data and Resources

All simulations in this thesis were performed using the open-source software package SeisSol (<https://doi.org/10.5281/zenodo.4899349>), freely available at <https://github.com/SeisSol/SeisSol>. In this thesis, we use a spatiotemporal discretization of polynomial degree 4 (Order of 5) for all DR simulations.

All simulation input files for our preferred model, high resolution plots and the aforementioned video are accessible at the Zenodo data repository: <https://doi.org/10.5281/zenodo.7011137>

All observational seismic waveforms used in this thesis were from the NARS-Botswana network (NARS, 2019 <https://doi.org/10.7914/SN/NR>) and were downloaded through the Incorporated Research Institutions for Seismology Data Manage Center (IRIS DMC). The NARS-Botswana network is operated by the Utrecht University, Netherlands.

Non-planar fault planes in this thesis were generated by using standard SeisSol Meshing python scripts, which are accessible at Github repository (<https://github.com/SeisSol/Meshing>). We use open-source meshing software, *Gmsh*, to create the Box domain. We discretize the unstructured tetrahedral mesh using commercial software, SimModeler (Simmetrix Inc., NY). We visualize our SeisSol simulation results in Paraview (5.10.1).

We use open-source python package Obspy (<https://github.com/obspy/obspy>) and MATLAB (R2022a, 64-bits maci64 with TUM student license) to analyze the seismic data. All analysis code (Matlab and Python) and data for this thesis are archived at Github repository (<https://github.com/HongyiSu/masterthesis>).

All the simulations reported in this thesis were running on department cluster (*heisenbug*, 256 AMD CPUs, 512 GB RAM), which was invested by my supervisors. All simulation results and input files are archived at [/import/freenas-m-05-seissol/Su/masterarbeit](http://import/freenas-m-05-seissol/Su/masterarbeit).

Acknowledgements

First and foremost, I am deeply indebted to my supervisors, Prof. Alice-Ange Gabriel and Dr. Max Moorkamp. Alice is very knowledgeable about earthquake physics and dynamic rupture simulation, she always knew which paper is the right one to answer my questions, and I have understood a lot by reading these papers. Max is an expert on MT inversion, he gave me the location of estimated fault traces in pairs of latitude and longitude coordinates and the 3D material model in netCDF format. Max always willing to help and gives constructive feedbacks. I also would like to acknowledge two former bachelor students, Thomas Obermaier and Sophia Gahr, who did their bachelor's thesis with Alice and Max on this topic. I am very happy and grateful to be admitted into this joint master's program between the two elite German universities, where I met so many brilliant researchers. I would like to give thanks to all of my lecturers from LMU Munich and TUM, they are: Prof. Heiner Igel, Dr. Marcus Mohr, Prof. Hans-Peter Bunge, Prof. Alice-Ange Gabriel, Dr. Max Moorkamp, Dr. Sara Carena, Dr. Florian Lhuillier, Prof. Roland Pail (TUM), Dr. Bernhard Schuberth, Dr. Joachim Wassmann, Dr. Christoph Kiemle (TUM) and Dr. Marcello Passaro (TUM). I would like to express my gratitude once again to Prof. Igel and Dr. Mohr who give me the most lectures. I used a lot of material from Heiner's textbook, *Computational Seismology: A Practical Introduction*, in this thesis. A special thanks go to the LMU International Office for providing me a Study Scholarship (funded by the Government of Free State of Bavaria) for my thesis work. I would like to thank Dr. Mark Hutchison for his review of my application proposal. Next, I would like to thank Dr. Thomas Ulrich for many useful python scripts and for showing me how to constrain initial stress conditions in dynamic rupture models with a kinematic model, Dr. Fabian Lindner for reviewing my Jupyter notebook for data acquisition using Obspy and for discussing on observational data quality in Botswana area, Dr. Casper Pranger for teaching me friction behaviour in microscale, Dr. Shihao Yuan for discussing waveform-based seismic inversion (FWI) compare to physics-based forward model approach, Mr. Fabian Kutschera for helping me to be familiar with Paraview. A big thanks go to Prof. Roland Bürgmann (UC Berkley) and Dr. Kathryn Materna (USGS) for sharing their InSAR data and discussing genesis of intraplate earthquakes, Asst. Prof. Shengji Wei (NTU) for sharing his kinematic model with us. I also would like to thank my classmates and peers, Fabian Kutschera, Saskia Steibel and Julie Svendsmark for walking me through the Covid pandemic and studying together. Finally, I would like to express my highest gratitude possible to my beloved parents, Jingdong Su and Xuemei Yang, and my grandparents, Denggui Su and Mingyue Wei, for supporting my decision to study aboard even that means they might not see me for several years, we have indeed not seen each other since the corona pandemic in 2019. I hope I can visit them soon.

Also thanks to all those who have helped me in this study that I have forgotten to acknowledge.

Statement of Authorship

With this statement, I certify that this master thesis has been composed by myself. Unless otherwise acknowledged in the text, it describes my own work. All references have been quoted and all sources of information have been specifically acknowledged. This thesis has not been accepted in any previous application for a degree.

Selbständigkeitserklärung

Hiermit versichere ich, diese Masterarbeit selbständig und lediglich unter Benutzung der angegebenen Quellen und Hilfsmittel verfasst zu haben. Ich erkläre weiterhin, dass die vorliegende Arbeit noch nicht im Rahmen eines anderen Prüfungsverfahrens eingereicht wurde.